Department of Radio Science and Engineering

Geometry-based radio channel modeling: Propagation analysis and concept development

Juho Poutanen

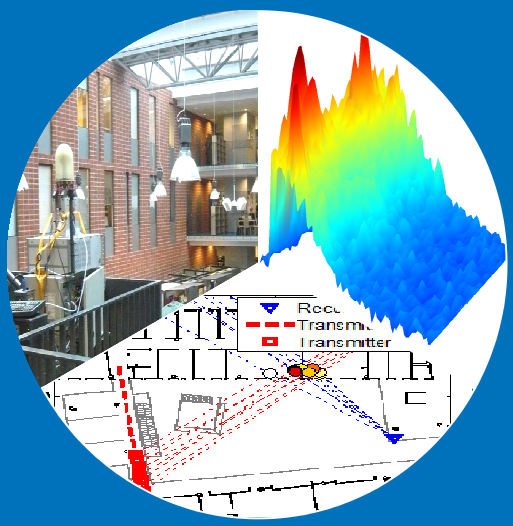

Aalto University

DOCTORAL DISSERTATIONS

Aalto University publication series
DOCTORAL DISSERTATIONS 36/2011

Geometry-based radio channel modeling: Propagation analysis and concept development

Juho Poutanen

Doctoral dissertation for the degree of Doctor of Science in Technology to be presented with due permission of the School of Electrical Engineering for public examination and debate in Auditorium S1 at the Aalto University School of Electrical Engineering (Espoo, Finland) on the 13th of May 2011 at 12 noon.

Aalto University
School of Electrical Engineering
Department of Radio Science and Engineering

Supervisor
Prof. Pertti Vainikainen

Instructor
Dr. Katsuyuki Haneda

Preliminary examiners
Prof. Mir Ghoraishi, Tokio Institute of Technology, Japan
Dr. Tricia Willink, Communication Research Centre, Canada

Opponents
Dr. Jonas Medbo, Ericsson Research, Sweden
Prof. Martine Lienard, University of Lille, France

Aalto University publication series
DOCTORAL DISSERTATIONS 36/2011

ISBN 978-952-60-4106-3 (pdf)
ISBN 978-952-60-4105-6 (printed)
ISSN-L 1799-4934
ISSN 1799-4942 (pdf)
ISSN 1799-4934 (printed)

Aalto Print
Helsinki 2011

The dissertation can be read at http://lib.tkk.fi/Diss/

Aalto University

Abstract

Aalto University, P.O. Box 11000, FI-00076 Aalto www.aalto.fi

Author
Juho Poutanen

Name of the doctoral dissertation
Geometry-based radio channel modeling: Propagation analysis and concept development

Publisher School of Electrical Engineering

Unit Department of Radio Science and Engineering

Series Aalto University publication series DOCTORAL DISSERTATIONS 36/2011

Field of research Radio Engineering

Manuscript submitted 19 November 2010 **Manuscript revised** 10 March 2011

Date of the defence 13 May 2011 **Language** English

☒ **Monograph** ☐ **Article dissertation (summary + original articles)**

In order to fully exploit the potential that the multiple-input multiple-output (MIMO) technology can provide for the novel radio communication applications, knowledge of the radio channel is necessary. For instance, signal processing algorithms or network coverage planning are tasks that are vitally dependent on the characteristics of the radio channel in which the system is desired to operate. However, since it is both time-consuming and expensive to measure all the envisioned usage scenarios, accurate and easy-to-use channel models are essential in many stages of the system development.

This thesis aims at improving the quality of the geometry-based stochastic MIMO channel models (GSCMs). First, an overview of the existing MIMO channel models is given including a detailed description of the principles of the models using the geometry-based approach. In addition, the shortages of the current GSCMs are discussed in order to motivate the work of the thesis on their part.

The main achievements of this thesis are the following. First of all, as compulsory background work, a measurement-based ray tracer (MBRT) was developed in order to facilitate detailed analysis of the radio channel measurements. With the help of the MBRT, channel model parameters for GSCMs were extracted from measurement data gathered in various indoor environments. In addition, the characteristics of the so called dense multipath components (DMC) were comprehensively studied, and as a result, a method to include the DMC to the GSCMs was developed. Finally, issues related to multi-link MIMO channel modeling were addressed. First and foremost, the propagation phenomena that are important in multi-link scenarios were studied. Based on the analyses, an approach to extend current GSCMs to fully support simulations of multi-link scenarios was invented.

Many of the outcomes of this thesis have been directly applied in the COST 2100 MIMO channel model.

Keywords Radio wave propagation, geometry-based radio channel modeling, dense multipath components, multi-link MIMO channel modeling

ISBN (printed) 978-952-60-4105-6 **ISBN (pdf)** 978-952-60-4106-3

ISSN-L 1799-4934 **ISSN (printed)** 1799-4934 **ISSN (pdf)** 1799-4942

Location of publisher Espoo **Location of printing** Helsinki **Year** 2011

Pages 159 **The dissertation can be read at** http://lib.tkk.fi/Diss/

Tekijä
Juho Poutanen

Väitöskirjan nimi
Geometriaan perustuva radiokanavamallinnus: Radioaaltojen etenemisen analysointi ja konseptien kehittäminen

Julkaisija Sähkötekniikan korkeakoulu

Yksikkö Radiotieteen ja -tekniikan laitos

Sarja Aalto University publication series DOCTORAL DISSERTATIONS 36/2011

Tutkimusala Radiotekniikka

Käsikirjoituksen pvm 19.11.2010 **Korjatun käsikirjoituksen pvm** 10.03.2011

Väitöspäivä 13.05.2011 **Kieli** Englanti

☒ **Monografia** ☐ **Yhdistelmäväitöskirja (yhteenveto-osa + erillisartikkelit)**

Tiivistelmä

Jotta moniantenni- eli MIMO-tegnologian mahdollistama potentiaali pystyttäisiin kokonaisuudessaan hyödyntämään uusissa radiotietoliikennesovelluksissa, radiokanavan ominaisuudet tulee tietää tarkasti. Esimerkkejä suunnittelutehtävistä, joissa radiokanavan vaikutukset tulee huomioida, ovat signaalinkäsittelyalgoritmien suunnittelu ja solurakenteisen radioverkon kattavuussuunnittelu. Koska radiokanavamittaukset ovat kalliita ja aikaa vieviä, käytännössä on kuitenkin mahdotonta mitata radiokanavan ominaisuudet kaikissa mahdollisissa järjestelmän käyttöympäristöissä. Sen vuoksi järjestelmien suunnittelussa tarkoilla ja helppokäyttöisillä radiokanavamalleilla on keskeinen rooli.

Tämän väitöskirjan tavoitteena on parantaa geometriaan perustuvien MIMO-kanavamallien laatua. Aluksi työssä tehdään katsaus eri kanavamallinnusmenetelmiin ja erityisesti geometristen mallien periaatteet esitellään yksityiskohtaisesti. Lisäksi käsitellään olemassa olevien kanavamallien puutteita.

Väitöskirjan seuraavassa osassa kehitetään työkalu radioaaltojen etenemismekanismien tunnistamiseen mittaustuloksista. Tämä niin kutsuttu mittaustuloksiin perustuva säteenseuraaja (MBRT) mahdollistaa geometristen mallien parametrisoinnin sekä uusien mallinnuskonseptien suunnittelun geometristen mallien laadun parantamiseksi. Työn keskeisimmät saavutukset voidaan jakaa kolmeen pääosaan: 1) Olemassa olevien yhden linkin geometristen mallien parametrisointi sisätiloissa, 2) niin sanottujen tiheiden monitiekomponenttien (DMC) ominaisuuksien tutkiminen ja mallintaminen, ja 3) monen linkin geometrisen kanavamallin luominen.

Monia tässä väitöskirjassa saavutettuja tuloksia on suoraan hyödynnetty myös COST 2100 MIMO kanavamallin kehityksessä.

Avainsanat Radioaaltojen eteneminen, geometriaan perustuva radiokanavan mallinnus, tiheät monitiekomponentit, monen linkin MIMO radiokanavan mallinnus

ISBN (painettu) 978-952-60-4105-6 **ISBN (pdf)** 978-952-60-4106-3

ISSN-L 1799-4934 **ISSN (painettu)** 1799-4934 **ISSN (pdf)** 1799-4942

Julkaisupaikka Espoo **Painopaikka** Helsinki **Vuosi** 2011

Sivumäärä 159 **Luettavissa verkossa osoitteessa** http://lib.tkk.fi/Diss/

Preface

The work for this Doctoral thesis has been done at the Department of Radio Science and Engineering in Aalto University School of Science and Technology. The work is also a part of the Nordite WILATI+ project, which is a joint project between Aalto University in Finland, Lund University in Sweden, and Norwegian University of Science and Technology in Norway. Some parts of the thesis have been done in close cooperation with the COST 2100 action.

I would like to thank Professor Pertti Vainikainen for giving me the opportunity to work in his group among this truly interesting and challenging subject. The instructor of the work, Dr. Katsuyuki Haneda, deserves my deepest gratitude for the infinite number of hours he has spent helping and guiding me during my post-graduate studies. I thank Professor Fredrik Tufvesson for many fruitful discussions and for helping me in writing publications; and, most importantly, for hosting me during my several visits in his department in Lund University.

I humbly thank Dr. Veli-Matti Kolmonen who is always able to help me whatever the problem I have; and Dr. Jussi Salmi for letting me use the codes he has developed for the data analysis. Without the contribution of these two guys, I would never have finished this thesis. In addition, all the people working in the WILATI+ project deserve acknowledgment for creating an excellent working atmosphere during the whole project. I would also like to express my gratitude to Professor Claude Oestges, Dr. Nicolai Czink, and Mr. Lingfeng Liu for inspiring cooperation within the COST 2100 action.

Finally, I thank my family for both mental and financial support during my studies. I also thank my girlfriend Laura and my other friends for helping me to maintain a good balance in my life.

Helsinki, November 18, 2010

Juho Poutanen

Contents

List of Abbreviations

Aalto	Aalto University School of Science and Technology
AS	Angular spread
3GPP	3rd generation partnership project
BS	Base station
CC	Common cluster
CDF	Cumulative distribution function
CMC	Correlation matrix collinearity
COST	Cooperation europeenne dans le domaine de la recherché scientique et technique
CPR	Co-polarization ratio
CS	Computer science
DMC	Dense multipath components
DoA	Direction of arrival
DoD	Direction of departure
DS	Delay spread
EKF	Extended Kalman filter
ESPRIT	Estimation of signal parameters via rotational invariance technique
FDTD	Finite difference time domain
GPS	Global positioning system
GSCM	Geometry-based stochastic channel model
GSM	Groupe spécial mobile, or Global system for mobile communications
i.i.d.	Independent and identically distributed
INR	Interference-to-noise ratio
ISIS	Initialization and search improved SAGE algorithm
ITS	Intelligent transportation system

LOS	Line-of-sight
LTE	Long term evolution
LU	Lund University
MBC	Multiple bounce cluster
MBRT	Measurement-based ray tracer
MIMO	Multiple-input-multiple-output
MOM	Method of moments
MPC	Multipath component
MS	Mobile station
MUSIC	Multiple signal classification
NLOS	Non-line-of-sight
OD	Offset distance
OLOS	Obstructed line-of-sight
PADP	Power-angular-delay profile
PAP	Power-angular profile
PDF	Probability density function
RIMAX	Parameter estimation algorithm
RS	Radio science
RT	Ray tracing
RX	Receiver
SAGE	Space-alternating generalized expectation-maximization
SBC	Single bounce cluster
SC	Specular components
SCM	Spatial channel model
SL	Shadowing level
SNR	Signal-to-noise ratio

SRC	Sum rate capacity
TX	Transmitter
UCC	Uncommon cluster
UCL	Universite Catholique de Louvain
ULA	Uniform linear array
UWB	Ultra wide-band
VR	Visibility region
WBAN	Wireless body area network
WILATI	Wireless LANs with high throughput in interference-limited environments
WIMAX	Worldwide interoperability for microwave access
WINNER	Wireless world initiative new radio
WLAN	Wireless local area network
WMAN	Wireless metropolitan area network
XPR	Cross-polarization ratio

List of symbols

$*$	Convolution operation
$(\cdot)^{\mathrm{T}}$	Matrix transpose operation
$(\cdot)^{\mathrm{H}}$	Complex transpose
$\det(\cdot)$	Determinant
$\mathrm{tr}\{\cdot\}$	Trace operation
$\lvert\cdot\rvert$	Absolute value
$\lVert\cdot\rVert_{\mathrm{F}}$	Frobenius norm
$E\{\cdot\}$	Expected value
α	Signal amplitude
$\boldsymbol{a}$	Array response vector
c	Speed of light
C	Channel capacity
d	Propagation path distance
η	INR
ϕ	Direction of departure
f	Frequency
ψ	Direction of arrival
G	Antenna pattern
$\mathbf{H}$	Radio channel matrix
h	Channel impulse response
$\mathbf{I}$	Identity matrix
j	Imaginary number
k	Wave number

K_{c}	Cluster K-factor
K_{sel}	Cluster selection factor
K_{LOS}	LOS power factor
k_{τ}	Cluster decay factor
λ	Wavelength
L	Power scaling factor
μ	Mean value
n	Noise
N	Number of clusters
ξ	Random phase
p_{common}	Probability of common clusters
P	Power
Ψ	Normalized DoD
$\Psi_{\mathrm{c,MS/BS}}$	Scatterer angle
ρ	SNR
$\mathbf{r}$	Antenna position vector
$\mathbf{R}$	Correlation matrix
σ	Standard deviation
S_{common}	Significance of common clusters
t	Time
τ	Delay
$\mathbf{u}$	Unit vector
x	Transmitted signal
y	Received signal

Part I – Introduction

1 Context and contributions of research

1.1 Trends in wireless communications

The information revolution in the 1980s and 1990s launched a dramatic change in billions of people's lives and in global economics [18]. Millions of routine tasks that previously required human labor became automated and all types of electronic devices became a part of every-day life. Along with the information revolution, also communications – both wired and wireless – encountered evolution no one would have imagined. First and foremost, two innovations around the early 1990s, i.e. the internet and the GSM, changed the direction of people's lives. From those days, an unforeseen growth has reached around two billion internet users [19], and more than four billion GSM users [20].

Roughly within the past ten years, a clear trend in wireless communications has been to combine the easy access to an enormous amount of data provided by the internet with the mobility of a mobile phone. Numerous new technologies, e.g. GSM EDGE [20], 3G LTE [21], WLAN [22], and WIMAX [23], have emerged with the same aspiring vision: high data rate wireless internet access everywhere and for everyone. Businessmen are online and working efficiently and people are consuming diverse multimedia services regardless of place and time. Something about the tremendous success of this vision tells the endless debates around coffee tables about whether Nokia or Apple makes the best smartphones; or the biggest headlines in the tabloids being the speculations about Nokia's new CEO.

In addition to the never-ending desire to increase data rates and flexibility of the personal communication devices for more efficient working and versatile entertainment, another trend in wireless communications has been that we are seeing radio waves to be utilized in more and more imaginative applications. Take for instance the so called intelligent transportation systems (ITSs) where vehicles exchange information with other vehicles or communicate with the infrastructure to e.g. avoid accidents or to control congestion [24], [25]; the wireless body area networks (WBANs) where sensors are put on the surface of and/or inside human body for the purpose of remote healthcare [26], [27]; or alternative localization and navigation applications to GPS [28] by utilizing WLAN, GSM, or even broadcast TV network infrastructures [29] – [32]. And the story is only at its beginning.

The explosion of wireless communications that we have witnessed during the recent decades has required both creative thinking and, first and foremost, invention of huge amount of new enabling technologies. New higher frequency bands have been taken into use e.g. from the millimeter wave region, and the so called ultrawideband (UWB)

systems have been widely developed [33], [34]. On top of these, multi-antenna and cooperative communication systems have been considered as promising solutions to rise to the challenges of flexible and high data rate wireless systems [35], [36].

1.2 Scope and contributions of the thesis

The development of a new wireless system requires broad knowledge starting from the characteristics of the physical radio wave propagation, going through hardware construction and signal processing algorithm development to the design of high-layer protocols. The scope of this thesis is restricted to the lowest level of the development chain, i.e. to the characterization and modeling of radio channels, mainly for the purposes of multiple-input-multiple output (MIMO) communication system development. Even though research in the field of MIMO systems has been remarkably intensive during the past years, the potential of the MIMO systems is yet to be fully exploited in practical applications, for which at least a part of the reason is the lack of thorough understanding of the characteristics of the radio channel.

In this thesis, tools and methods have been developed for more detailed analysis of the radio propagation phenomena based on measurement data, and the obtained knowledge has been utilized in the development of geometry-based stochastic MIMO channel models (GSCMs). Among a large variety of different types of MIMO channel models, the geometry-based approach was chosen due to many features that make it attractive for the simulations of MIMO systems, such as the inherent capability to mimic the spatial and temporal characteristics of radio channels in a straightforward manner. Even though GSCMs have been widely studied already prior to this thesis, and the existing GSCMs are very sophisticated, they still include numerous severe deficiencies that have motivated the work of this thesis.

In particular, the contributions of this thesis can be divided into four main parts:

- *Methods and tools for radio wave propagation analysis.* The first main contribution of this thesis is the development of tools and methods for detailed propagation analysis based on measurement data. To this end, the so-called measurement-based ray tracer (MBRT) was developed. The MBRT is a Matlab-based computer program whose core idea is to combine measurement results with digital map of the measurement environment. With the MBRT, the paths along which the signals propagated in measurements can be identified. The obtained knowledge is essential when developing the channel models in the later parts of the thesis.

- *Channel model parameterization and validation.* The second main contribution of the thesis has been to investigate the characteristics of radio channels based on measurements, and to extract parameter values for cluster-based channel models, including a full parameterization of the COST 2100 MIMO channel model [16] in indoor scenarios. In addition, the COST 2100 channel model has been validated against measurement data. Previously, part of the parameters of the COST 2100 channel model has either been totally lacking or not extracted based on measurement data. The validation of the COST 2100 channel model done in this work is the first of its kind.

- *Characterization and modeling of dense multipath components.* Another shortage of the previous GSCMs has been the omission of the so called dense multipath components (DMC) from the models. The DMC represent the part of the radio channel that cannot be characterized by a superposition of distinct plane waves, and is known to contribute significantly to the real-world radio channels. In this thesis, the characteristics of the DMC have been thoroughly analyzed based on measurement data, and an approach to include the DMC to the GSCMs has been proposed.

- *Multi-link MIMO channel modeling.* In principle, the structure of a general GSCM supports simulations of multi-link scenarios, i.e. scenarios with multiple base stations (BSs) and/or mobile stations (MSs) just by dropping multiple BSs or MSs to the simulation environment. However, in the previous implementations of the GSCMs, there has not been any way to control the important characteristics of the radio wave propagation in multi-link scenarios, especially the correlation between different links. In this work, extensive multi-link measurements have been analyzed, and a concept to extend the GSCMs to fully support simulations of multi-link scenarios has been developed.

The results of this thesis can be utilized in developing new radio channel models, and as an example, many novel features of the COST 2100 channel model, such as the multi-link extension and the approach to model the DMC, have been directly exploited based on the modeling concepts originally invented in this thesis. The analyses of this thesis are in many respects based on dual-link MIMO channel sounding measurements done at the frequency of 5.3 GHz in indoor scenarios. However, the developed methods and modeling concepts can be applied to any other environment or frequency range, as well.

1.3 Organization of the thesis

This thesis has been mainly written based on publications [1] – [17], which all have been previously authored or co-authored by this author. In particular, all the research results presented in this thesis have been previously reported in those publications.

The content of this thesis is organized in four parts as follows. Part I introduces the context of the research field of this thesis, and provides an overview of MIMO systems and principles of MIMO channel modeling. In Part II, the tasks needed in the development of GSCMs, and how these tasks have been performed in this thesis, are explained. In addition, a case study on the evolution of number of clusters, as well as the parameterization and validation of the COST 2100 channel model are presented in Part II. The research results presented in Part II are based on publications [1] – [5]. In Part III, the characteristics of the DMC have been investigated based on extensive set of measurement data, and, based on the findings, an approach to include the DMC into the GSCMs has been presented. Part III is based on publications [6] – [9]. Part IV is dedicated for multi-link MIMO channel modeling, including analyses of the propagation phenomena that are important in the simulations of multi-link scenarios, and the introduction of a concept with which a generic GSCM can be extended to fully support the simulations of multi-link scenarios. Part IV is based on publications [10] – [17].

1.4 Contribution of the Author

The overall research framework of this thesis was defined in cooperation between this author, Dr. Katsuyuki Haneda, and Prof. Pertti Vainikainen. Prof. Vainikainen was the supervisor, and Dr. Haneda the instructor of the thesis. The used radio channel measurement system was developed within the WILATI project Dr. Veli-Matti Kolmonen being the main responsible person, and the measurement campaigns were carried out by the WILATI project members, including this author. Dr. Jussi Salmi provided the data processing codes for the EKF parameter estimation algorithm. Both the measurement data and EKF parameter estimation algorithm have been used throughout the thesis as basis for the analyses.

In Part II, the MBRT was designed and implemented by this author. Furthermore, all propagation analyses and the COST 2100 channel model parameter extraction were performed by this author. The validation of the COST 2100 channel model was done in cooperation between this author, Dr. Haneda, and Mr. Lingfeng Liu: This author processed the measurement data that were used in the validation and provided the model

parameters, Mr. Liu provided the implementation code of the COST 2100 channel model, and Dr. Haneda was responsible for defining the validation procedure and conducting the actual simulations.

In Part III, this author performed all the measurement data analyses regarding the propagation characteristics of the DMC. This author was also the main initiator of the idea of how to include the DMC to geometry-based channel models, and this idea was further refined in discussions between this author, Prof. Fredrik Tufvesson, and Dr. Haneda.

In Part IV, all the measurement data analyses were performed by this author. The concept of common clusters was developed in cooperation between this author and Dr. Haneda. The method to investigate common clusters based on measurement data was defined by this author. The multi-link GSCM based on common clusters was implemented in cooperation between this author and Mr. Alvaro Palacios. The description of how to apply the concept of common clusters in the COST 2100 channel model was defined by this author, Dr. Haneda, Mr. Liu, Prof. Claude Oestges, and Prof. Tufvesson.

2 Basics of MIMO systems and MIMO channel modeling

A MIMO system is a wireless communication system that is equipped with multiple antennas at both ends of the link. Compared to conventional single-antenna systems, MIMO systems enable many significant advantages in terms of e.g. link reliability and data transfer rate. The most fundamental difference between the operation of a single-antenna system and a MIMO system is grounded on the way they treat multipath propagation. In the conventional single-antenna systems, fading caused by multipath propagation was considered as a disturbing element for the communication link and its effect was tried to be removed. In MIMO systems, the dispersive radio channel is, on the contrary, used to enhance the overall system performance, e.g. by utilizing independent signal paths to create parallel data streams and thus to increase the capacity. MIMO technology has also been recently adopted by several standards, namely by the 3GPP long term evolution (LTE) [21], the new WLAN standard IEEE 802.11n [22], and the mobile internet WIMAX [23].

A schematic illustration of the operation of a generic MIMO system is shown in Figure 2.1. The transmit signal is fed as a digital bit stream to the TX, where the stream is pre-processed before feeding it to the antenna ports. At the RX, the received signal needs to be post-processed in order to decode the original signal that was transmitted. The performance of a MIMO system depends on the quality of the signal processing algorithms at the TX and RX. However, the signal processing algorithms are not developed only based on the envisioned performance target (i.e. link reliability, capacity enhancement, etc), but also the characteristics of the radio channel in which the system needs to operate play an essential role. In fact, the thousands of research articles published roughly within the previous twenty years in the area of MIMO can be categorized into 1) MIMO signal processing papers and 2) MIMO channel modeling papers.

2.1 Forms and benefits of MIMO

MIMO systems offer many attractive advantages compared to the conventional single-antenna communication systems in terms of e.g. data transfer rate and link reliability without additional bandwidth or transmit power. There are two forms of MIMO, i.e. co-located MIMO and distributed MIMO, which are explained in the following.

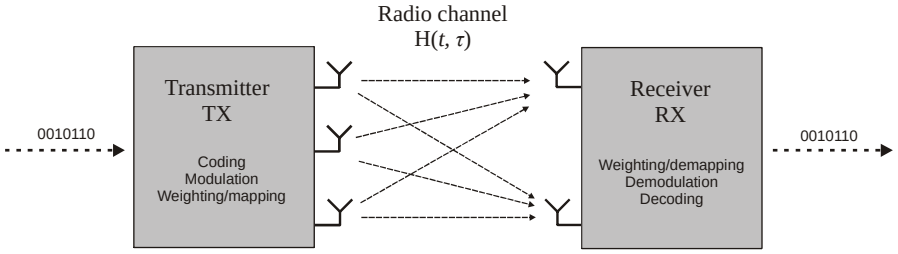

Figure 2.1. Illustration of a MIMO system.

2.1.1 Co-located MIMO

Co-located MIMO stands for a "traditional" MIMO system where the communication link is established between two devices that are each equipped with multiple antennas. The techniques through which MIMO systems exploit all its benefits can be roughly categorized into three main parts: 1) diversity techniques, 2) spatial multiplexing, and 3) beamforming. All of these functions aim to improve the performance of the communication in slightly different ways, and it is generally not possible to achieve all of them simultaneously.

Diversity

The fluctuation of the signal level due to multipath fading and shadowing can be significantly reduced by multi-antenna technology by using *diversity* techniques. Using multiple antennas at the reception only (i.e. single-input-multiple-output, SIMO), the probability that the signal is in a deep fade can be decreased by combining the signals received by different antennas, and hence improve the average signal-to-noise ratio (SNR); this method is often referred to as *receive diversity*. In cases where multiple antennas are used only at the transmitter (MISO), *transmit diversity* is applicable. If the channel is unknown to the transmitter, transmit diversity can be obtained by using space-time codes to design the transmitted signal. On the other hand, if channel information is available at the transmitter, the signal can be transmitted from each transmit antenna after being weighted appropriately, so that the different replicas of the signal arrive in phase at the receiver and add coherently. This technique is also known as *maximum ratio combining*. More comprehensive discussion on MIMO diversity techniques can be found e.g. in [37].

Spatial multiplexing

Probably the most attractive advantage of MIMO systems is the potential to hugely increase the channel capacity. By utilizing parallel data streams between the multiple transmit and receive antenna pairs, the amount of data transferred through the same radio channel and *within the same time, bandwidth, and transmit power* can be multiplied. Traditionally, enhancements in data transfer rate were obtained either by expanding the communication bandwidth or by using higher level constellations which, in turn, required higher SNR (i.e. more transmit power). In an ideal case, a system equipped with N antennas at the receiver and M antenna at the transmitter can multiply the channel capacity by the factor of $\min(N, M)$ compared to a conventional single antenna system [39], [35]. The technique to utilize parallel data streams to enhance the channel capacity is often called *spatial multiplexing*.

Beamforming

The beam of an antenna array can be directed to a desired direction by adjusting the phases of the signals fed to the different antenna elements [38]. This feature enables numerous fascinating usage applications. For example, interference caused by other users can be reduced, and the gain of the desired communication enhanced, if users can be separated in the spatial domain by directing the BS antenna towards the desired user [40], [41]. Figure 2.2 shows an example of this kind of interference reduction. In this case, the BS equipped with an antenna array directs its radiation to communicate with MS 1 and to reduce the interference caused by the interfering mobile, i.e. MS 2. As a result, the SNR in the BS – MS 1 increases, and interference caused by MS 2 decreases.

The principle of beamforming functions also the other way around, meaning that it is possible for a device equipped with multiple antennas to estimate the directions of the incoming signals. The direction finding capability can be used e.g. in localization applications as an alternative to the global positioning system (GPS), or in radar applications [42], [43].

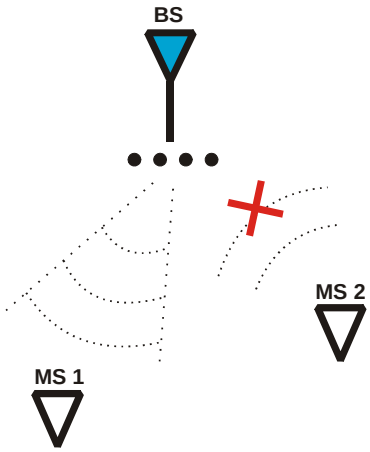

Figure 2.2. Principle of interference reduction. BS directs its antenna beam to improve communication with MS1. Simultaneously, interference caused by the un-wanted mobile MS2 is reduced.

2.1.2 Distributed MIMO

Distributed MIMO stands for a communication technique, in which several mobiles share their antennas in order to create a virtual MIMO system, and, by working together, can reap some of the benefits of co-located MIMO systems [36]. For instance, in a relay scheme shown in Figure 2.3, the source node may communicate with the destination via a relay node, if the direct link between the source and destination is of bad quality. Given that the source-destination and the source-relay-destination links are independently fading, this type of relaying scheme introduces spatial diversity. Several challenges are faced in the development of the cooperative or multi-user MIMO techniques. On one hand, communication-theoretical issues are related to problems such as which nodes should work together and how, in order to e.g. maximize network throughput or minimize overall power consumption. On the other hand, the radio channel characteristics in multi-user environments should be well investigated, since for instance the correlation between different links has a significant impact on the performance of a distributed MIMO system.

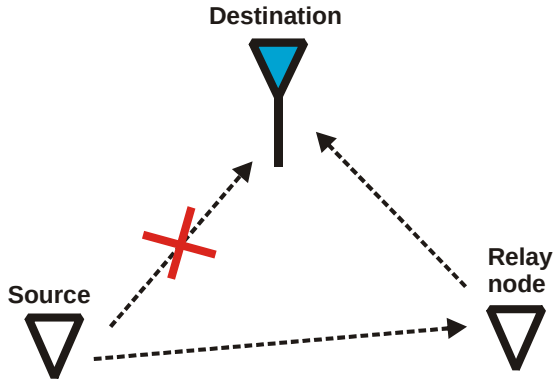

Figure 2.3. Illustration of a relay channel. The source may communicate with the destination through a relay node if the direct link between the source and the destination is in a deep fade.

2.2 MIMO radio channel modeling

How to exploit the benefits offered by the MIMO technology in the best possible way? This is a question that has tried to be answered by signal processing algorithms in thousands of recently published research articles. One of the barriers that people who are trying to answer the question face, is, that the performance of any MIMO system is always fundamentally dependent on the characteristics of the radio channel (depicted by $\mathbf{H}(t,\tau)$ in Figure 2.1) in which the system operates. And the radio channel is not always friendly. For instance, the early performance analyses of the MIMO technologies promised enormous capacity gains compared to the conventional single-antenna systems [35], [39]. In the initial studies, however, a crucial assumption of independent and identically distributed (i.i.d.) fading was commonly made concerning the characteristics of the radio channel, meaning that all channels between the different TX and RX antenna pairs were regarded as uncorrelated and Gaussian distributed. The physical interpretation of the i.i.d. assumption is that the radio channel would consist of a very large number of distinguishable signal paths that could be utilized in the transmission of a large number of parallel data streams. Later on it was realized that realistic radio channels rarely exhibit the i.i.d. fading characteristics, but often only a limited number of independent signal paths are available, which results in strong spatial correlation. Unfortunately, it soon became evident that when MIMO systems are assessed in their realistic operation environments, their performance stays far behind the theoretical promises [45] – [48].

This fact underlined the need of physically meaningful methods to mimic the wireless channel and the underlying radio wave propagation mechanisms, so that it would be

possible for the researchers and engineers to develop the MIMO systems from the beginning under more realistic usage conditions. Nowadays – more than twenty years after the invention of the MIMO technology – a large variety of different types of channel models have been established for characterizing the wireless medium for MIMO communication systems [50], [51].

2.2.1 MIMO radio channel

The radio channel typically consists of several multipath components (MPCs) departing from the TX and arriving at the RX at different time instants due to reflections and diffractions from scattering objects in the surrounding environment. Mathematically, the relationship between the transmitted signal x and the received signal y can be expressed as a function of time t and delay τ as

$$y(t) = h(t,\tau) * x(t) + n(t) \tag{2.1}$$

where $h(t,\tau)$ is the channel impulse response, $n(t)$represents additive noise, and $*$ denotes the convolution operation.

In a MIMO system, the radio channel is often presented as matrix $\mathbf{H}(t,\tau)$ which is comprised of the time-variant impulse responses $h_{ij}(t,\tau)$ between the *j*-th transmit antenna and the *i*-th receive antenna as

$$\mathbf{H}(t,\tau) = \begin{bmatrix} h_{11}(t,\tau) & h_{12}(t,\tau) & \cdots & h_{1m}(t,\tau) \\ h_{21}(t,\tau) & h_{22}(t,\tau) & \cdots & h_{2m}(t,\tau) \\ \vdots & \vdots & \ddots & \vdots \\ h_{n1}(t,\tau) & h_{n2}(t,\tau) & \cdots & h_{nm}(t,\tau) \end{bmatrix}. \tag{2.2}$$

For flat fading channels, (2.1) can be expressed in a matrix form as

$$\mathbf{y}(t) = \mathbf{H}(t)\mathbf{x}(\mathrm{t}) + \mathbf{n}(t), \tag{2.3}$$

where $\mathbf{x}(t)$ and $\mathbf{n}(t)$ are the signal and noise vectors.

On the other hand, the temporal and angular dispersion of a radio channel can be described by a double-directional impulse response [49] as

$$\hat{h}(\mathbf{r}_{\mathrm{TX}}, \mathbf{r}_{\mathrm{RX}}, t, \tau, \phi, \psi) = \sum_{p=1}^{P} \hat{h}_{\mathrm{p}}\,(\mathbf{r}_{\mathrm{TX}}, \mathbf{r}_{\mathrm{RX}}, t, \tau, \phi, \psi), \tag{2.4}$$

where t, τ, ϕ, and ψ denote the time, excess delay, and the directions of departure (DoD) and –arrival (DoA). Furthermore, P is the total number of MPCs, and $\mathbf{r}_{\mathrm{TX}}$ and $\mathbf{r}_{\mathrm{RX}}$ are the antenna position vectors at the TX and RX.

The ultimate goal in MIMO channel modeling is to artificially create the MIMO channel matrix $\mathbf{H}(t,\tau)$ so that its properties are similar to those of the realistic radio channels, including the dispersion of the radio channel in angular and temporal domains. However, if we take a closer look at Equation (2.2), we notice that the characteristics of the channel in angular domain are not explicitly described by the MIMO channel matrix, since its elements $h_{ij}(t,\tau)$ are functions of time and delay only. On the other hand, Equation (2.4) directly shows the channel response as a function of time, delay, angles of departure, and angles of arrival. Hence, there is an essential difference in what these two representations of the MIMO radio channel actually tell us.

In fact, Equations (2.2) and (2.4) represent the two main categories in MIMO channel modeling. The first category is *analytical modeling*, where the channel matrix $\mathbf{H}(t,\tau)$ in Equation (2.2) is directly created mathematically without full and detailed consideration of underlying physical propagation phenomena. The second category in MIMO channel modeling is *physical modeling*, where the double-directional impulse response in Equation (2.4) is obtained by calculating the t, τ, ϕ, and ψ of each MPC for a given simulation environment on the basis of physical wave propagation.

As stated above, the goal in MIMO channel simulations is to finally obtain an artificially created channel matrix, and hence, it is important to understand the relationship between the MIMO channel matrix $\mathbf{H}(t,\tau)$, which includes the antenna array properties, and the double directional impulse response $h(\mathbf{r}_{\mathrm{TX}},\mathbf{r}_{\mathrm{RX}},t,\tau,\phi,\psi)$, which, on the other hand, is expressed by the propagation parameters. The following is the equation that relates these two representations:

$$h_{ij}(t,\tau) = \int_{\tau'}\int_{\phi}\int_{\psi} h_p\left(\mathbf{r}_{\mathrm{TX}}^{j},\mathbf{r}_{\mathrm{RX}}^{i},t,\tau',\phi,\psi\right) \times G_{\mathrm{TX}}^{j}(\phi)G_{\mathrm{RX}}^{i}(\psi)f(\tau-\tau')d\tau' d\phi d\psi, \tag{2.5}$$

where $\mathbf{r}_{\mathrm{TX}}^{j}$ and $\mathbf{r}_{\mathrm{RX}}^{i}$ are the coordinates of the j-th transmit and i-th receive antenna, and $G_{\mathrm{TX}}^{j}(\phi)$ and $G_{\mathrm{RX}}^{i}(\psi)$ are the j-th transmit and i-th receive antenna patterns, and $f(\tau)$ is the overall impulse response of the TX and RX antennas and frequency filters. A significant difference between analytical and physical models is that, the output of the analytical model, i.e. $\mathbf{H}(t,\tau)$, includes antenna properties and pulse shaping, whereas physical models based on Equation (2.4) are independent of antennas describing only the

propagation channel itself. This means that when using physical models, the channel matrix can be created for an arbitrary antenna configuration. Next, an overview of the previously developed analytical and physical MIMO channel models is given.

2.2.2 Analytical models

Analytical channel models characterize the impulse response or the transfer function of the radio channel analytically, i.e. mathematically without explicitly considering the underlying wave propagation mechanisms. The fundamental idea in analytical channel models is to determine the impulse response between all TX/RX antenna pairs individually, which are then merged to form the MIMO channel matrix. Analytical models can be further categorized into propagation-motivated models and correlation-based models. Propagation-motivated models generate channel matrices via propagation parameters (such as directions and delays of signals), whereas the correlation-based models characterize the MIMO channel matrix statistically in terms of the correlations between the matrix entries. Examples of propagation-motivated models are the finite scatterer model [65], the maximum entropy model [66], and the virtual channel representation [67], and of correlation-based models are the Kronecker model [68], [69], [70], [71] and the Weichselberger model [72].

2.2.3 Physical models

Physical channel models characterize the environment and construct the double-directional radio channel [49] between the TX and RX on the basis of electromagnetic wave propagation. The propagation parameters of the radio waves, i.e. DoD, DoA, and delay, are determined for each MPC based on the geometry of the simulation environment. Physical channel models can be further split into deterministic, geometry-based stochastic and non-geometric stochastic models.

In deterministic methods, such as ray tracing (RT) [52], [53], [54], finite difference time domain (FDTD) [55], or the method of moments (MOM) [56], the propagation parameters are characterized in a purely deterministic manner for a pre-determined environment. All the mentioned deterministic modeling approaches require as detailed as possible description of the environment, including accurate description of the geometry, material parameters, weather conditions, people, etc, which may be difficult to obtain in practice. This, together with the fact that deterministic methods are computationally heavy means that they may not always be a suitable alternative despite their creditable modeling exactness.

With GSCMs, the radio propagation is modeled with specific TX, RX, and scatterer geometries, which are drawn in a stochastic manner. Whereas in deterministic models the radio channel is simulated for a specific site, GSCMs construct the propagation channel by placing scatterers to the simulation coordinates randomly based on stochastic parameters that are typical for the environment scenario that is to be modeled. Examples of GSCMs are the COST 259 [57], [58], COST273 [59], [60], COST2100 [16] and WINNER [61] channel models. Non-geometric channel models, e.g. the Saleh-Valenzuela model [62] and the Zwick model [63], describe the propagation parameters themselves in a completely stochastic manner without calculating them based on the geometry of the environment. Table 2.1 shows the classification of the different channel models.

Table 2.1. Classification of MIMO channel models.

Physical models	**Analytical models**
i) Deterministic - Ray tracing - FDTD - MOM	i) Correlation-based: - i.i.d model - Kronecker model - Weichselberger model
ii) Geometry-based stochastic - COST 259/273/2100 - WINNER - 3GPP SCM	ii) Propagation motivated: - Finite scatterer model - Maximum entropy model - Virtual channel representation
iii) Non-geometrical stochastic - Saleh-Valenzuela model - Zwick model	

2.3 Geometry-based channel modeling

Since this thesis contributes to the development of GSCMs, the modeling philosophy behind them is explained in detail in this chapter. The properties of the state-of-the-art GSCMs are discussed by presenting the structure of the COST 2100 channel model in detail. The COST 2100 is currently the most sophisticated GSCM, and one of the essential aspects in this thesis has been to contribute to the development of that model.

"COST" is an abbreviation for *European cooperation in the field of scientific and technical research* [73] and its purpose is to gather researchers around Europe to collaborate among scientific topics. Several COST actions have been dedicated to wireless communications during the recent decades, and a number of channel models have been developed within the previous COST actions, i.e. COST 207 [74], COST 231

[75], COST 259 [57], [58], and COST 273 [60] channel models. The COST 207 and COST 231 channel models have been widely used in the development of the GSM systems, whereas the COST 259 was the first geometry-based MIMO channel model developed by the COST, and was continued by the COST 273. After the COST 273 action, the COST 2100 action continued the development of the GSCMs.

2.3.1 Basic structure

The radio channel typically consists of several distinct MPCs departing from the TX and arriving at the RX with specific directions and delays due to reflections and diffraction from scattering objects in the surrounding environment. The MPCs often tend to appear as clusters, i.e. groups of closely located MPCs that have propagated along a similar path. In the GSCMs the underlying idea is to theoretically create the radio channel in delay and directional domains by placing clusters in the simulation environment to emulate the physical scattering objects of real environments. The characteristics of the clusters are modeled based on channel measurements, and naturally, the accuracy of a cluster-based channel model always is indispensably dependent on the quality of the cluster parameters.

The basic structure of a simple GSCM is shown in Figure 2.4, where the radio channel between the mobile station (MS) and the base station (BS) consists of one single bounce cluster and a pair of double bounce clusters. Around the MS there is a local cluster which is needed in order to model the MPCs that have a random angular distribution and thus cannot be included in other clusters. The black dots inside each cluster depict the scattering points associated with individual MPCs within the clusters. Usually, the clusters are placed in the simulation coordinates in a stochastic (random) fashion, and the propagation path parameters are calculated based on the created geometry for each MPC.

One of the biggest advantages of the GSCMs is that a large number of different scenarios can be modeled by using the same modeling framework just by modifying the model input parameters. Examples of the different scenarios are rural macrocell, urban microcell, and indoor office scenarios. The parameters of the model are roughly categorized into stochastic (cluster) parameters and external parameters that describe the environment. The stochastic cluster parameters are determined based on channel measurement data, and they describe e.g. the number of clusters and how the clusters are distributed in the simulation environment, as well as how the MPCs are placed within each cluster. The external parameters describe the environmental characteristics e.g. the network cell sizes or antenna heights, or other system related parameters such as the used frequency band. The parameterization of the GSCMs is addressed more in detail later in this thesis, and hence is not considered any further here.

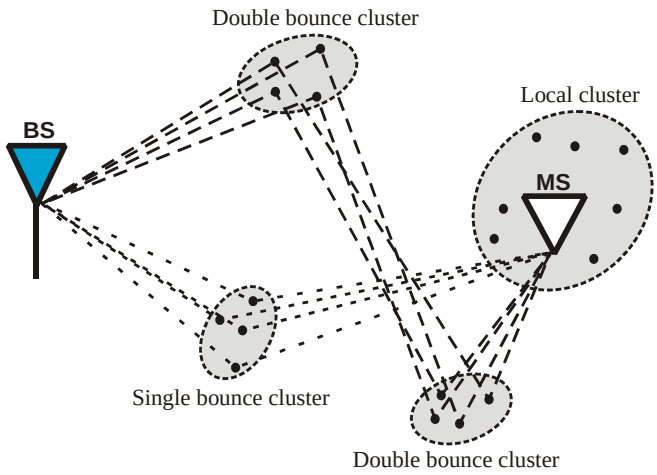

Figure 2.4. Cluster-based channel model. Clusters emulate the physical scatterers of real environments in order to create a multipath propagation channel between the mobile (MS) and base stations (BS).

Modeling the time-varying behavior of the channel

In GSCMs, clusters are generated randomly for a given BS position, and after the clusters have been placed in the simulation environment, the MS can be dropped in any location in the network. The time evolution of channel parameters is implicitly simulated in a realistic manner simply by moving the MS along a continuous route, since the cluster positions are fixed during a simulation run.

In realistic environments the power carried by each scatterer fluctuates, and besides, old scatterers may disappear and new scatterers appear as the location of the MS changes. In the COST 2100 channel model, this dynamic behavior of the radio channel is modeled by the following means. First of all, cluster power undergoes fast fading (or small scale fading) due to fading caused by different MPCs within each cluster, and on top of that, cluster power is assigned a random fading component to account for the shadow fading that also exists in real radio channels. The appearance and disappearance of clusters is controlled by the concept of visibility regions (VRs). In the VR concept, each cluster is assigned a VR, and the cluster is activated only when the MS enters the corresponding VR. The VR concept is illustrated in Figure 2.5: even though there are altogether four clusters in the simulation environment, the MS is inside only one VR and thus only the corresponding cluster is active at this time. The total number of clusters and VRs in the environment is determined so that on average the MS is inside a pre-determined number of VRs, and as a result, sees a pre-determined number of clusters.

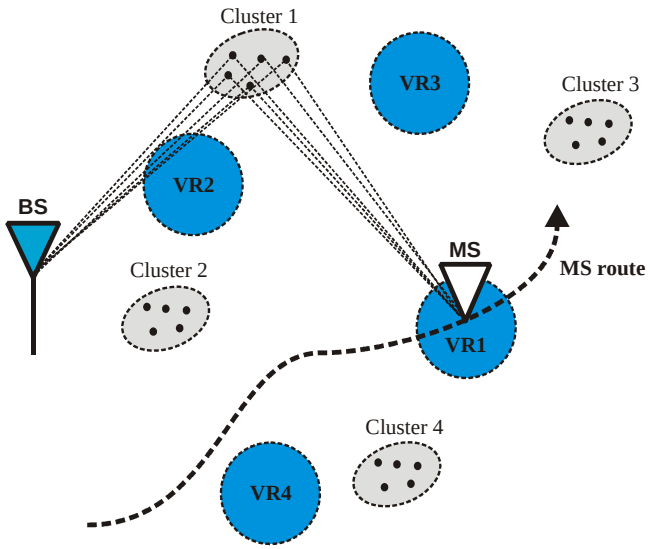

Figure 2.5. Modeling the dynamic behavior of the channel in the COST 273 channel model. A cluster is active only when the MS is located inside the corresponding visibility region (VR).

Cluster parameters

The cluster parameters needed by the GSCMs can be divided into three classes: 1) inter-cluster parameters, 2) intra-cluster parameters, and 3) cluster location parameters. The inter-cluster parameters describe the global cluster settings, e.g. the total number of clusters and their relationships with each other. The intra-cluster parameters, on the other hand, are necessary in order to describe how the MPCs are arranged within each cluster thus specifying the internal structure of the clusters. Cluster location parameters define how the clusters are located in the simulation coordinates. The cluster parameters and the methods of how to extract them from measurement data will be described more in detail in Part II.

2.3.2 New features of the COST 2100 channel model

Despite the significant advances that have been made in the field of MIMO propagation channel modeling, there are still a number of effects known to exist in real environments but have not been dealt with properly in the previous geometry-based channel models, such as the COST 273 or the WINNER channel models. This section highlights the most important features that are further considered in the later parts of this thesis, and that are also included in the COST 2100 channel model.

Incomplete parameterization

As mentioned earlier in this chapter, the cluster-based structure of the GSCMs enables a large variety of different kinds of environments to be simulated just by changing the parameter values input to the model. The downside of the approach is that to parameterize all the envisioned model scenarios based on valid channel measurements is a huge task. For instance in the COST 273 channel model, many parameters are either totally missing or the quality of the parameters is questionable due to a limited amount of sound channel measurement data. In Part II of this thesis, an appreciable effort has been made to complete the parameterization of the COST 273 channel model in indoor environments.

Dense multipath components (DMC)

Current GSCMs model the radio channel by using a superposition of a finite number of distinct MPCs, often referred to as specular components (SC). This is a natural approach, since also the model parameters have been determined based on measured propagation path parameter estimates that mainly comprise the SC. However, lately it has been noticed that only a part of the power in the radio channel can be characterized by the SC and that also the residual part, i.e. the DMC has a significant impact. In Part III, the characteristics of the DMC are studied comprehensively based on indoor channel measurements. Based on the analyses, a method to include the DMC to the GSCMs is also presented in Part III.

Multi-link MIMO channel modeling

In principle, the structure of the existing single-link geometry-based MIMO channel models, such as COST 273 and WINNER, supports simulating multi-link radio environments by dropping more than one MSs or BSs in the simulation environment. However, investigations of the VRs for the different clusters and users are lacking and it is not yet known if the radio channels simulated by such models are realistic enough. As a pioneer work in multi-link geometry-based channel modeling, Part IV will provide the foundation for the extension of current geometry-based MIMO models to multi-link scenarios. The new COST 2100 multi-link MIMO channel model [16] is based on the principles developed in this thesis. Naturally, the principles developed in this thesis can be applied to extend any other GSCM to support multi-link scenarios, as well.

Channel model implementation and validation

One of the most critical parts in establishing a channel model is to validate the quality of the model. A usual way to perform the validation is to compare the output of the channel simulation with the measurement based on which the model was parameterized. For the WINNER channel model, validation works have been reported in [77] and [78], but for the COST 273 and COST 2100 channel models, the validation presented based on publication [5] in Part II is the first of its kind.

Summary of Part I

Two main trends have been emerging in wireless communication during the recent years. On one hand, new smartphones represent the trend to combine high data rate internet access and mobile phone in order to enable flexible multimedia services and efficient working regardless of space and time. On the other hand, wireless communications have spread to a wide range of new application areas, such as intelligent transportation systems and remote healthcare. The development of new wireless systems has required invention of many enabling technologies, for instance MIMO, UWB, and mm-wave systems.

The focus in this thesis is on the development of radio channel models for MIMO systems. The MIMO technology has been widely studied due to its numerous significant advantages compared to traditional communication systems in terms of higher data rates and better reliability. However, the performance of a MIMO system is only as good as the radio channel in which it operates allows. Therefore, knowing the characteristics of the radio channel plays an essential role in all levels of the development of novel MIMO communication systems.

An overview of the existing MIMO channel models was given in Chapter 2. The structure of the geometry-based stochastic channel models was explained in detail by following the concepts of the COST 2100 channel model. Even though the existing geometry-based channel models are extremely sophisticated, they still have numerous severe shortages, for which the later parts of this thesis try to find solutions.

Part II – Development of single-link GSCMs

3 Establishing a geometry-based channel model

Establishing a GSCM requires four essential parts: 1) channel measurements, 2) propagation path parameter estimation, 3) propagation analysis, and 4) model development, see Figure 3.1. In this chapter, each part will be briefly explained. However, the focus in this thesis is on parts 3) and 4), whereas tools and methods to accomplish the tasks in parts 1) and 2) already have been successfully developed within the frameworks of the Dissertations of Dr. Veli-Matti Kolmonen [79] and Dr. Jussi Salmi [80].

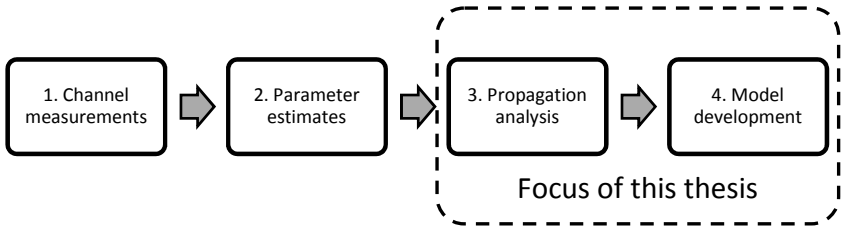

Figure 3.1. Four steps in geometry-based MIMO channel modeling

3.1 Channel measurements

The first task in the channel model development chain is to do channel measurements. The role of channel measurements can be understood to be two-fold; first of all, in order get insight about the physical phenomena for which the modeling framework is intended to be constructed, experimental observations are a prerequisite. On the other hand, once a model framework has been established, measurements are needed for the parameterization and validation of the model.

Since the trend in novel radio systems has recently been to efficiently utilize detailed information about the channel, the requirements for the measurement systems have increased accordingly. The measurement system has to be capable of measuring the dispersion of the channel in polarization, angular and delay domains in dynamic environments. In order to resolve signal directions with a high resolution, the channel sounder needs to be equipped with large enough antenna arrays (or highly directional antennas) at both ends of the link, whereas the resolution in the delay domain is

dependent on the bandwidth of the measurement system. Furthermore, if dynamic channels need to be measured, switching between the TX-RX antenna pairs, i.e. the channel sampling rate, needs to be fast to ensure that the channel characteristic do not change during a sample the channel is being measured. The measurement properties and the limiting factors are summarized in Table 3.1.

Table 3.1. Properties of the channel measurements and the limiting factors.

Performance measure	**Limiting factor**
Angular resolution	Size of the antenna arrays
Delay resolution	Bandwidth
Maximum Doppler frequency	Channel sampling rate

The results of this thesis are based on measurements that have been conducted by using a unique dual-link channel sounding system consisting of two sounders [81]: one of the sounders has been developed in Aalto University School of Science and Technology (Aalto) [82] and the other, a commercial RUSK channel sounder from Lund University (LU), has been manufactured by Medav [83]. The dual-link sounder was tailored for the purposes of simultaneous dual-link channel measurements and it consists of one TX (from LU) and two RXs (from Aalto and LU). It mimics a situation where the two RXs are intended to represent BSs of adjacent network cells and the TX acts as the MS, as shown in Figure 3.2 (a). This way it is possible to measure characteristics which are required in the development of multi-link channel models. The system is capable of measuring simultaneously two wideband dual-polarized links, having the MIMO matrix sizes of 30 × 30 and 30 × 32. The used antenna arrays and switches are shown in Figure 3.2 (b). The specifications of the dual-link sounder are listed in Table 3.2. To take into account the deficiencies of the measurement system, several calibration measurements were performed, namely back-to-back calibration, power level calibration in an anechoic chamber, and a detailed radiation pattern measurement for all antenna elements. A thorough description of the conducted calibration measurements can be found in [81].

An excellent reference for more detailed description of the used measurement system, and channel measurement techniques in general, can be found in the Dissertation of D.Sc. Veli-Matti Kolmonen [79].

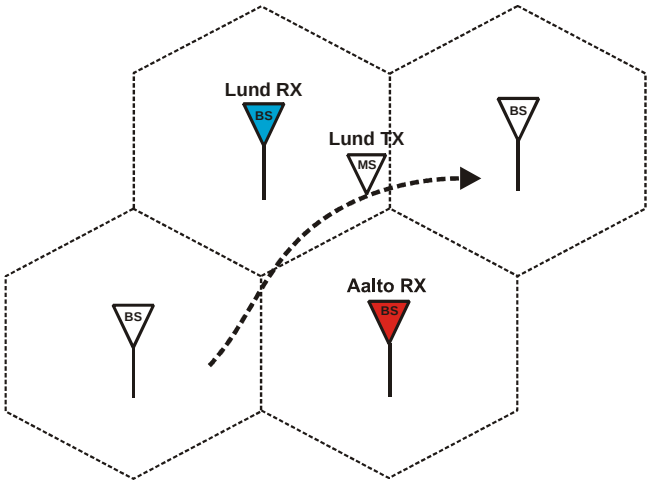

(a)

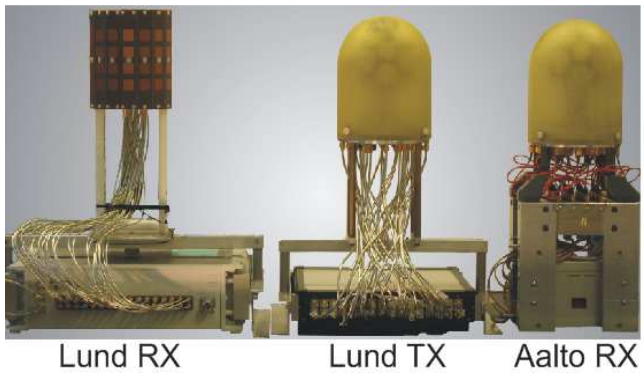

(b)

Figure 3.2. Dual-link channel sounder used in the measurements of this work. (a) Lund RX and Aalto RX represent BSs of adjacent cells and Lund TX acts as the MS. (b) Used antenna arrays and switches.

Table 3.2. The specifications of the dual-link sounder used in this thesis.

	LU sounder	**Aalto sounder**
Carrier frequency	5150 – 5750 MHz	5300 MHz
Bandwidth	10 – 240 MHz	120 MHz
TX-signal length	1.6 – 25.6 µs	N/A
Sampling rate at TX	320 MHz	N/A
Sampling rate at RX	640 MHz	120 MHz
RX-element switching interval	3.2 / 6.4 µs	3.2 / 6.4 µs
Time between MIMO snapshots	39.322 / 72.090 ms	39.322 / 72.090 ms
MIMO snapshot measurement time	3.277 / 6.554 ms	3.277 / 6.554 ms

3.1.1 Summary of analyzed measurements

The measurements that have been used as the basis for the radio channel analyses in this thesis were conducted in two different buildings. The first measurement venue was the Computer Science (CS) building located in the Otaniemi campus area of Aalto University School of Science and Technology, in Espoo, Finland. The floorplan of the CS building is shown in Figure 3.3 (a), and two photos of the environment are shown in Figure 3.3 (b) and (c); the red dashed lines in Figure 3.3 (a) depict the routes of the TX, the black triangles show the locations of the RXs, and the different walls are marked with letters A – D. The CS building has three floor levels, and there is a large open hall in the middle that occupies the whole height of the building. Small offices surround the open space, and as can be seen in Figure 3.3 (b) and (c), there are many windows on the walls. Several TX/RX combinations were measured; a summary can be found in Table 2.1.

The second measurement venue was an office corridor in the Department of Radio Science and Engineering (RS), also located in the Otaniemi campus area; the floorplan of the venue is shown in Figure 3.4 (a). Again, the red dashed lines depict the TX route, the black triangles the locations of the RXs, and the different walls are marked with letters A – D. In the measurements performed in this environment, the TX was moved along a corridor towards a T-junction, and the two RXs were located in corridors opposite two each other. Figure 3.4 (b) shows the location of RX2, and Figure 3.4 (c) the TX in the starting point of its route. As can be seen, walls A, C, and D are solid brick, whereas wall B is partly window close to the starting point of the TX route and brick in the end of the route.

All the measurements were performed by moving the TX trolley at a constant speed, an average distance between two snapshots being approximately 2.7 cm. During the measurements, there was no other activity (such as people moving around) in the surrounding environment. It is worth noticing, that not all the measurements have been used in all the analyses in this thesis, but the most representative scenarios have been selected for the analysis of each phenomenon. On the other hand, the measurement scenarios analyzed in this thesis are only a part of a huge archive of measurement data collected within the WILATI-project which have been, and will be, used in the research done by other people as well.

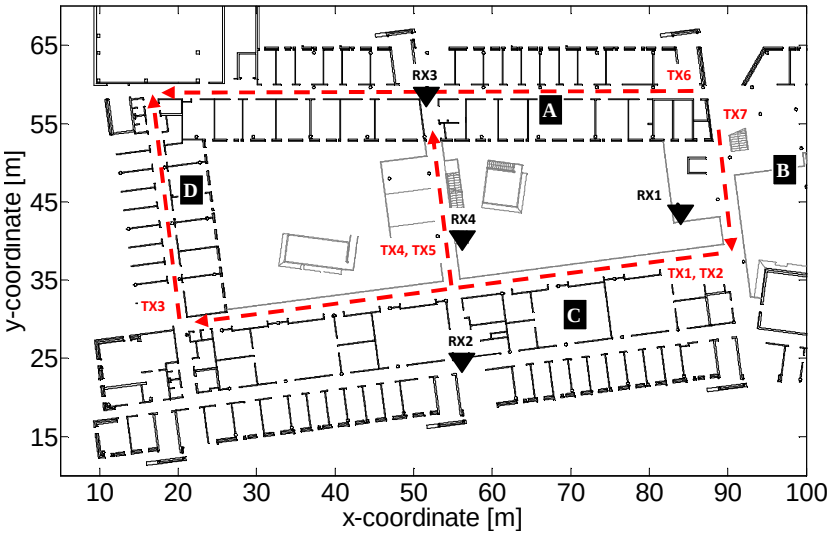

(a)

(b) (c)

Figure 3.3. (a) The floorplan of the Computer Science building. Red dashed lines show the TX routes and black triangles the locations of the RXs. (b) A photo of the environment taken from the bridge connecting the two sides of the building on the second floor. The Aalto RX is also seen on the left side of the photo in location RX4. (c) A view of the environment seen from the balcony of the third floor above RX1.

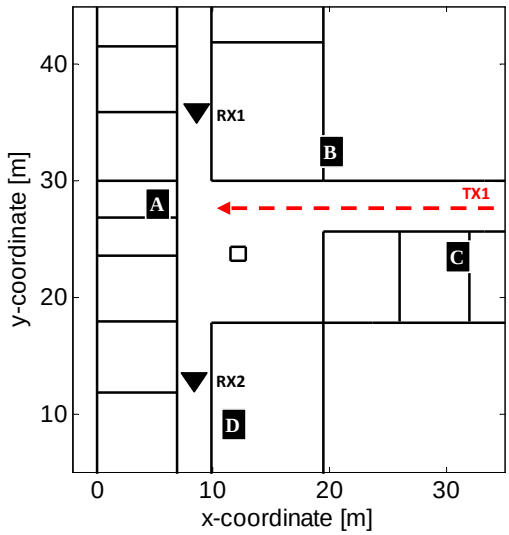

(a)

(b)

(c)

Figure 3.4. (a) Floorplan of the office corridor in Department of Radio Science and Engineering. Red dashed lines show the TX routes and black triangles the locations of the RXs. (b) View behind LU RX in location RX2. (c) TX in its starting position in the beginning of the corridor between walls B and C. Note that wall B is partly window in the beginning the TX route.

Table 3.3. Summary of measurements analyzed in this thesis

Building	Scenario	Floor level (TX/RX)	Snapshots	Conditions
Computer Science	TX1/RX1	2/2	3100	LOS
Computer Science	TX4/RX1	2/2	900	LOS
Computer Science	TX5/RX1	3/2	900	LOS
Computer Science	TX4/RX3	2/2	1600	LOS
Computer Science	TX2/RX2	3/2	2400	NLOS
Computer Science	TX2/RX3	3/2	2400	NLOS
Computer Science	TX3/RX1	2/2	1200	NLOS
Computer Science	TX3/RX3	2/2	1100	NLOS
Computer Science	TX3/RX4	2/3	1100	NLOS
Computer Science	TX6/RX1	2/2	2500	NLOS
Computer Science	TX7/RX1	2/2	1800	LOS
Radio Science	TX1/RX1	3/3	300	NLOS
Radio Science	TX1/RX2	3/3	300	NLOS

3.2 Propagation path parameter estimation

The data obtained from channel measurements are not directly in a feasible format for detailed propagation analysis or channel model development. The parameters of the double-directional radio channel need to be estimated with a specific channel parameter estimation algorithm, which, in essence, enables removing the effect of the antennas of the sounders from the data so that the radio channel itself can be studied in detail. The propagation path parameters of interest include DoD and DoA on azimuth and elevation planes, delay, and polarimetric path weight, which are estimated for each MPC (see Eq. (2.4)).

Several algorithms have been proposed for the estimation of channel model parameters from measurement data, including e.g. the ESPRIT [84], SAGE [85], RIMAX [86], and EKF [80], [87]. The different parameter estimation algorithms use somewhat different approaches for characterizing the radio channel, however, in all the algorithms, the essential idea is to approximate the double-directional radio channel by a superposition of distinct plane waves. The work done within this thesis is based on the EKF parameter estimation and –tracking algorithm, which uses two components to describe the radio channel **H**: 1) the superposition of the highly concentrated specular-like propagation paths, i.e. the SC, and 2) the distributed random scattering, i.e. the DMC as

$$\mathbf{H} = \mathbf{H}_{\mathrm{SC}} + \mathbf{H}_{\mathrm{DMC}}. \tag{3.1}$$

In the EKF algorithm, the SC are described by the DoD, DoA, delay, and polarimetric path weights. In addition, the algorithm tracks the path parameters over time meaning that each specular path has a lifetime over a number of consecutive measurement locations. This means that the state dimension is not fixed and hence the number of tracked paths changes as new paths may appear or old paths disappear as a function of time due to changes in propagation environment. More detailed description about the tracking of the paths, and how old paths are dropped and new paths added to the state can be found in [87]. The DMC explain the parts of the channel that cannot be estimated as SC due to limited antenna array aperture size, sounding signal bandwidth, and the complexity of the underlying physical processes of the channel. The DMC can be understood to consist of a very large amount of specular-like paths that are individually weak but may together represent a significant part of power carried by the radio channel. Traditional channel models have been based only on the SC. However, in Part III of this thesis the characteristics of the DMC are studied, and a method to include also the DMC to the GSCMs is presented.

The problem of propagation parameter estimation based on channel measurement data has been comprehensively discussed e.g. in the Dissertation of Dr. Jussi Salmi [80]. A thorough description of the EKF algorithm can also be found there.

3.3 Propagation analysis

Once the propagation parameters have been estimated, detailed propagation analysis is possible. The analyses may include e.g. investigation of some specific phenomenon, such as fading caused by some specific objects, or getting insight of the entire radio channel, such as power composition of different propagation mechanisms. However, whatever the goal in the propagation analysis might be, a basic task to begin with is to identify the different propagation mechanisms, and to relate these mechanisms with physical objects in the environment. This section is dedicated to first discussing the basic idea of how the measurement results can be related with the measurement environment, and then to introducing a tool which was developed to execute this task automatically.

3.3.1 Relating measurement results with the environment

For the construction of the GSCMs it is essential to have knowledge about the physical propagation mechanisms in the radio channel. Basically, each distinguishable propagation

path in the measured radio channel can be considered to be equivalent to an individual cluster in the GSCM. Each MPC obtained from the measurement data by a parameter estimation algorithm includes the DoD, DoA, and delay. Together with the map of the environment, the parameters can be used to identify the propagation paths and the scattering objects associated with each MPC.

Figure 3.5 shows an example of relating the parameter estimates with the physical environment. A joint DoD/DoA profile with the identified clusters is shown in Figure 3.5 (a), and the rays corresponding to each MPC are plotted in the physical environment in Figure 3.5 (b). In this imaginary example, the identified clusters included two single bounce clusters and one double bounce cluster originating via reflections from the surfaces of buildings 1 and 2. Also the LOS component existed.

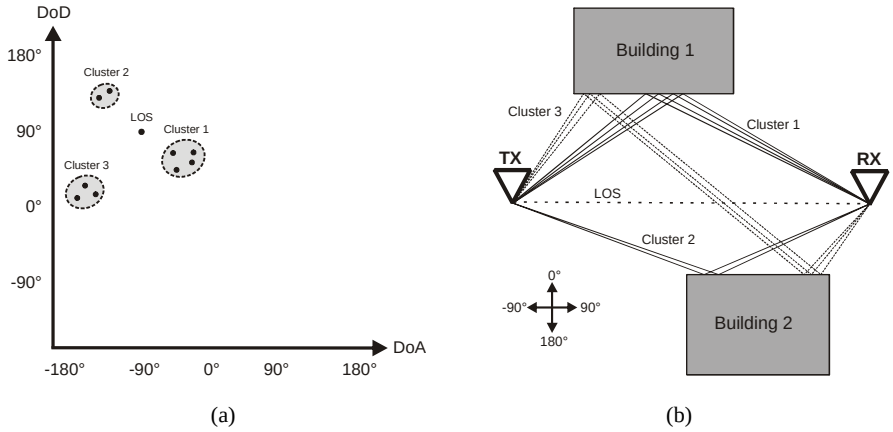

Figure 3.5. Example of relating the measured parameter estimates with the physical environment. (a) Joint DoD/DoA profile with identified clusters. (b) Rays corresponding to each MPC plotted in the physical environment.

3.3.2 The measurement-based ray tracer

Previously, the propagation paths of the clusters have been mainly determined manually, e.g. [88]. However, in complex environments, where the number of MPCs is large, manual inspection of the propagation paths becomes cumbersome. To overcome this problem, a measurement-based ray tracer (MBRT) was developed in [1] for automatic combining of the measured parameter estimates and physical objects in the measurement environment. The MBRT is a Matlab-based software that visualizes rays in measurement environments on both sides of the link according to the parameter estimates extracted from channel measurement, thus providing a physical interpretation of the measurement

results. All the input parameters and the visualization are based on the parameter estimates extracted from channel measurements; the ray launching algorithm itself is a very simple method including only specular reflections and ray-optical wave propagation.

The MBRT requires two inputs: measured propagation parameter estimates and a map of the measurement environment. The rays are launched from either or both ends of the link to the direction defined by the measured DoD and DoA, whereas the length of the propagation path d is determined by the measured delay time τ simply by $d = \tau c$, where c is the speed of light. The information about the measurement environment can be obtained for instance from a detailed AutoCAD [89] drawing of the measurement venue. Manual creation of simplified maps of the measurement environment is a straightforward and, in many cases, a sufficient alternative, in case detailed CAD data are not available.

An example of identification of the scattering points and signal paths in the cases of single- and double bounce paths is shown in Figure 3.6. The thick dashed red lines show the route along which the TX was moving, and the red squares and blue triangles indicate the TX and RX locations (scenario TX4/RX1 in Section 3.1.1). The dashed red and blue lines visualize the rays launched from the TX and RX on top of the CAD map of the measurement venue according to the directions specified by the EKF parameter estimates. The color of the scattering points indicates the path gain in dB for each reflected ray. The identification of the scattering points is accomplished by launching rays from both link ends according to the directional parameter estimates and by calculating the intersection point of these rays at each TX location, i.e. snapshot. The intersection point of the rays is considered as the scattering point. In case only the first or last interaction point seen from the TX or RX sides is needed, a straightforward alternative is to calculate only the intersection points on the object the rays hit first (or last). However, if the scattering point identification is done in this way, no knowledge about the intermediate propagation between the first and last interaction points is obtained.

The implementation of the MBRT is 2.5-dimensional, meaning that the azimuth and elevation dimensions are treated separately as two 2-D cases. This approach was considered sufficient since in indoor scenarios, which are the main focus in this thesis, most of the important phenomena occur on the azimuth plane, and usually in the elevation dimension the most probable propagation phenomenon is a single reflection from either ground or ceiling, for which the 2.5-D is in most cases sufficient. Furthermore, obtaining full 3-D CAD data is in practice far more complicated than the 2-D maps.

To summarize, the MBRT is a robust tool for identifying the propagation mechanisms from radio channel measurements thus providing an in depth physical interpretation for the measurement results. The MBRT forms an essential basis for the whole thesis.

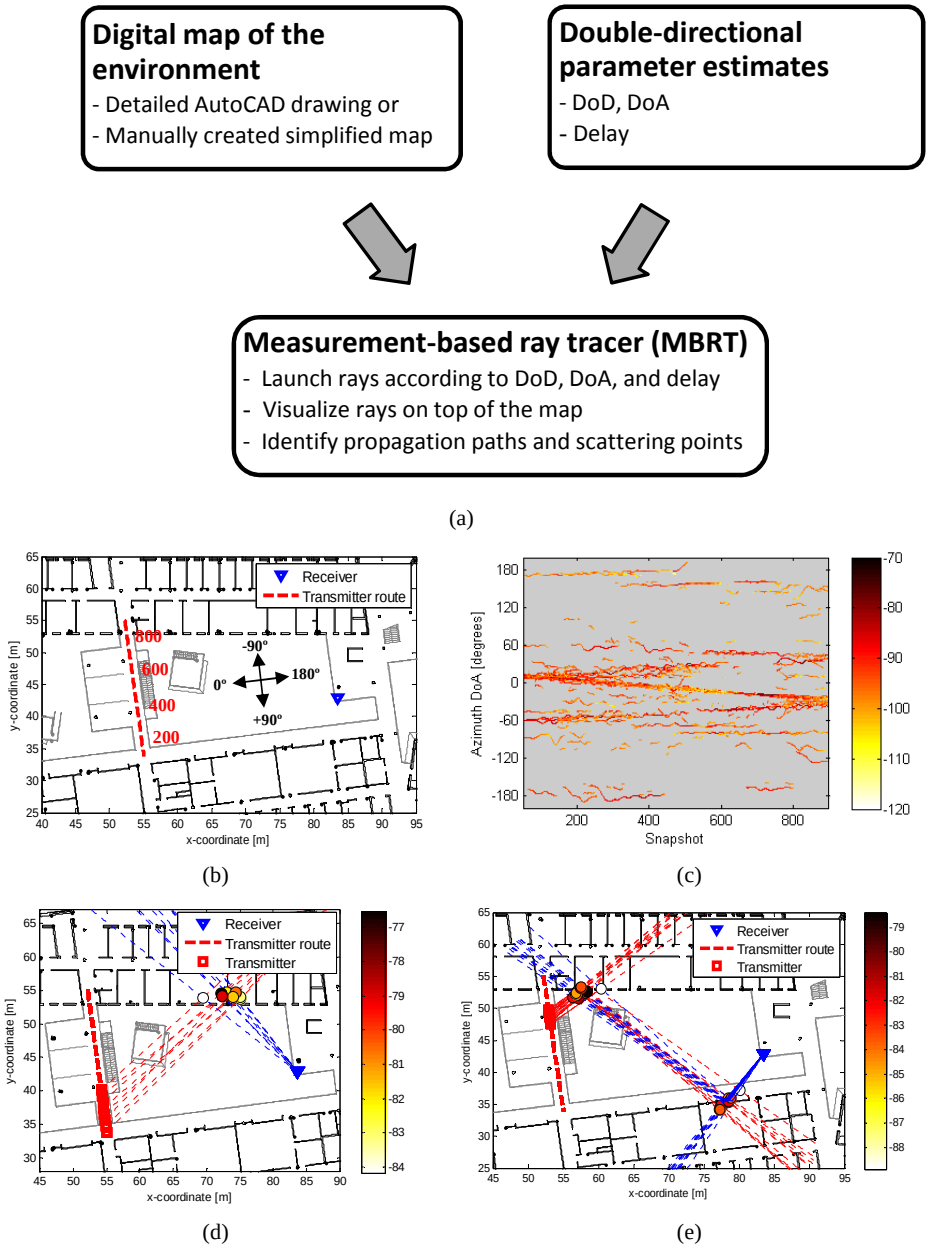

Figure 3.6. Identification of propagation mechanisms by using the measurement-based ray tracer (MBRT). (a) Block diagram. (b) CAD map of the measurement venue. (c) EKF parameter estimates of the azimuth DoA. (d) Example of scattering point- and propagation path identification in the case of a single bounce path and (e) a double bounce path.

3.4 Model development

3.4.1 New modeling concepts

Detailed propagation analysis provides us with an insight of the entire radio channel, which is essential when building up channel modeling concepts. For instance, the whole idea of the cluster-based GSCMs has originated from observations that the energy that is transferred by the radio channel is concentrated around certain directions due to reflections and scattering from objects in the environment. In this thesis, the MBRT has had an essential role in developing novel "add-on" concepts on top of the conventional GSCMs. Especially, methods for including the DMC to the GSCMs in Part III (publications [6] – [9]) and for the multi-link extension of the GSCMs in Part IV (publications [10] – [12], [17]) have been developed with the help of MBRT.

3.4.2 Multipath clustering

As mentioned above, in GSCMs the radio channel is described solely by the clusters that are placed in the simulation environment, meaning that the quality of the GSCMs is essentially dependent on the quality of the cluster parameters. In order to extract parameters for the clusters, the MPCs obtained by measured parameter estimates have to be grouped to form clusters. Traditionally, clustering has been done only based on the parameters of the estimated MPCs without an effort to relate them with physical objects, e.g. [90], [91]. In this thesis, the MBRT has been used for clustering by grouping the MPCs that propagated along similar paths, i.e. through similar scattering processes. In other words, each distinct propagation mechanism that is identified in the measurement data has been regarded as a cluster. Figure 3.7 shows an example of the power carried by each propagation mechanism[1], or cluster, in the scenario presented in Figure 3.6 (b). After grouping the MPCs to form clusters, it is possible to extract the parameters that are needed in generating clusters in GSCM. In the example presented in Figure 3.7, the radio channel consisted of the LOS component, single-, double-, and triple bounce clusters from different walls (marked with "A" – "D"), and of the ground reflection.

[1] In this case, 100 % corresponds to the total power of the SC, i.e. the DMC have not been considered.

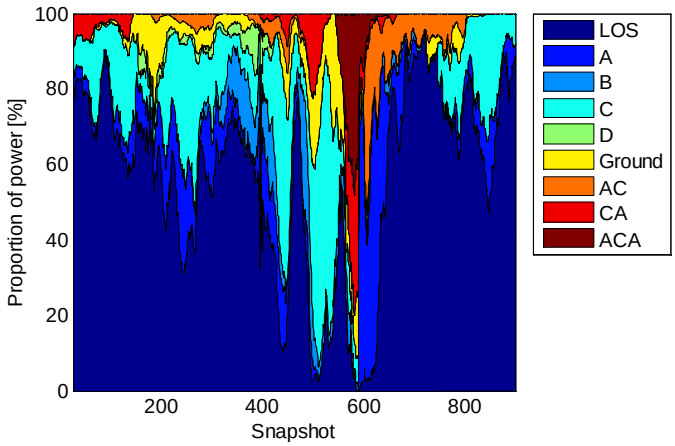

Figure 3.7. Evolution of the power composition for each cluster in measurement scenario presented in Figure 3.6 (b).

There are several advantages in clustering the MPCs based on the actual physical propagation paths when compared to clustering methods that are based only on statistical processing of the MPCs in parameter spaces without relating them with the physical environment:

- Since the GSCMs are also based on clusters which emulate physical scatterers, the measurement data processing in this thesis is done in the similar way as the channel model is constructed.
- The clustering method itself does not produce bias to the cluster parameters, such as intra-cluster spreads, since every MPC within a cluster really is originating from the same physical object(s).
- Clusters can be explicitly categorized into single- and multiple bounce clusters, which is advantageous when different parameters are used for different cluster types.
- Understanding of the physical propagation phenomena increases, which is useful as such e.g. for physically motivated computational field prediction methods, such as ray launching or ray tracing.

The MBRT has been used in several publications for the identification of propagation mechanisms and for the extraction of cluster parameters dedicated to the GSCMs, i.e. [2] – [7], [10] – [12], [17].

3.5 Propagation analysis case: Evolution of number of clusters

When analyzing the characteristics of radio channels, one of the most essential tasks is to resolve different propagation mechanisms and the corresponding scattering objects. This provides important knowledge of the entire radio channel, and enables for instance resolving the total number of clusters. In fact, the number of clusters is a very important feature in geometry-based channel models, because it consequentially affects many other channel characteristics, such as delay and angular spreads or channel capacity; in principle, overestimating the number of clusters would possibly end up overestimating e.g. angular and delay spreads or channel capacity. The number of clusters has been previously studied based on measurements in various publications. For instance Czink *et al.* studied the average number of clusters in indoor office environments in [92] and [76], and Hentilä *et al.* reported the lifetimes of individual clusters in indoor-to-outdoor and outdoor-to-indoor environments in [94].

In this section, the number of clusters and the evolution of number of clusters are studied in indoor environments. This section is based on publication [3].

3.5.1 Measurement scenarios

The measurements were carried out in the Computer Science (CS) building in Aalto University School of Science and Technology. Figure 3.8 shows the measured TX routes and RX positions. Altogether nine TX/RX combinations were measured, including four scenarios with LOS and five scenarios with NLOS conditions. Measurements TX1/RX1 and TX5/RX1 represent scenarios with LOS where both the TX and RX were located in the hall. In measurement TX4/RX1, the stairs obstructed the LOS component in the middle of the route, but otherwise there were LOS conditions. The measurement TX4/RX3 always had a LOS through an open door between the hall and the corridor. Measurements TX2/RX2, TX2/RX3, TX3/RX1, and TX3/RX4 were classified into NLOS conditions; one end of the link was always located in a corridor and the other in the hall. In measurement TX3/RX3, both sides of the link were located in a corridor. In the remaining parts of this paper, the LOS and NLOS measurement are treated separately. The properties of each measurement are summarized in Table 3.4.

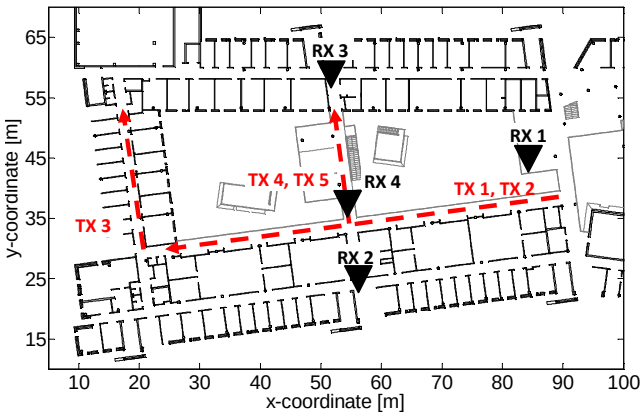

Figure 3.8. Floor plan of the measurment venue with the TX routes (dashed red lines) and the RX positions (black triangles).

Table 3.4. Summary of measurement scenarios

Scenario	Floor level (TX/RX)	Snapshots	Conditions
TX1/RX1	2/2	3100	LOS
TX4/RX1	2/2	900	LOS
TX5/RX1	3/2	900	LOS
TX4/RX3	2/2	1600	LOS
TX2/RX2	3/2	2400	NLOS
TX2/RX3	3/2	2400	NLOS
TX3/RX1	2/2	1200	NLOS
TX3/RX3	2/2	1100	NLOS
TX3/RX4	2/3	1100	NLOS

3.5.2 Number of clusters in LOS and NLOS scenarios

Clusters were extracted by first applying the EKF parameter estimation algorithm to the measurement data, and then by identifying the propagation mechanisms (i.e. clusters) with the MBRT, as described earlier in Section 3.3. Figure 3.9 (a) shows an example of the variation of the number of active clusters over the location of the TX for measurements TX4/RX1 (LOS) and TX3/RX3 (NLOS) for 800-snapshot periods. The number of active clusters is typically between 4 and 7 in the LOS measurement, and around 2 and 3 in the NLOS measurement. Another clear difference between these two cases is that the number of active clusters changes more rapidly in the NLOS than in the LOS scenario. The normalized histograms of the number of clusters in all LOS and

NLOS measurements are shown in Figure 3.9 (b) and (c). The probabilities were obtained by dividing the number of snapshots at which a certain number of active clusters was observed by the total number of snapshots (6500 and 8200 in LOS and NLOS scenarios, respectively). The mean value and the standard deviation of the number of active clusters are 3.7 and 1.4 in LOS, and 2.2 and 0.9 in NLOS scenarios. As was the case in measurements TX4/RX1 and TX3/RX3 shown in Figure 3.9 (a), the number of active clusters is also generally lower in NLOS than in LOS scenarios. This observation is in good accordance with the intuition; signals may arrive from all directions in LOS scenarios where both antennas are located in an open space, whereas that is not necessarily the case in NLOS scenarios because only a limited number of signal directions are possible due to blocking objects.

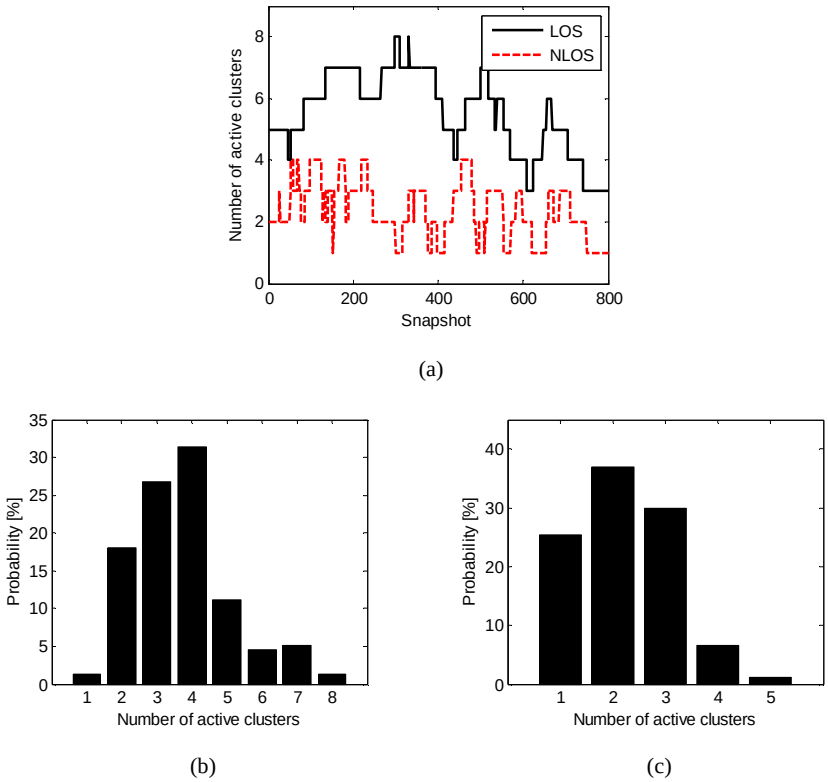

Figure 3.9. (a) Number of active clusters as a function of the TX location extracted from measurement TX4/RX1 (LOS) and TX3/RX3 (NLOS). (b) Probability density functions of the number of active clusters in LOS and (c) NLOS scenarios. The PDFs include data from all the measurements listed in Table 3.3.

3.5.3 Evolution of number of clusters as a Markov process

In addition to the instantaneous number of active clusters, it is important have knowledge about the rate of change in the number of clusters, as the location of the MS changes. In this case, to study the evolution of number of clusters is possible, since the analyses of the number of clusters were based on dynamic measurements carried out along continuous routes. Next, the evolution of number of clusters is analyzed by presenting the phenomenon as a Markov process, where different states represent the number of active clusters, and the transition probabilities between the states denote the probability that the number of clusters stays the same or changes [95]. The analysis of the evolution of number of clusters based on a Markov-process serves two different purposes: first of all, it is a convenient way of quantifying the rate of change in the number of clusters which indicates how rapidly the channel changes as a function of time in different environments. On the other hand, by using proper values for the transition probabilities between different states (i.e. number of clusters), it is possible to construct a realistic model for describing how the number of clusters changes[2], as was done in [3].

The Markov process describing the evolution of number of clusters is illustrated in Figure 3.10; the number of active clusters is denoted by *N*, whereas α and β_{N+1} and β_{N-1} represent the transition probabilities between different states, that is, the probabilities that the number of clusters stays the same or increases or decreases when moving from one snapshot to the next one. It is worth noticing, that α and β are related to, but do not directly tell, the lifetimes of individual clusters. However, they conveniently provide insight of how dynamically the radio channel characteristics change in different environments. In the following analysis, the probabilities that the number of clusters increases or decreases are both included in a single probability β, which describes the overall rate of change in the number of active clusters.

The CDFs of the transition probabilities α and β are shown separately for the LOS and NLOS scenarios in Figure 3.11. In the analyzed measurements, one snapshot corresponded to approximately 2.7 cm on average. We clearly see that the number of clusters changes more rapidly in the NLOS than in the LOS scenarios, which also indicates that the lifetime of clusters is typically longer in LOS scenarios. These observations can be explained in the following way. In the NLOS measurements analyzed here, at least either one of the TX or RX was located in a corridor, and therefore there were many scattering objects in the close vicinity of the antennas. Thus the scattering

[2]One should note that this approach for modeling the evolution of number of clusters is not relevant for the COST 2100 channel model, since there the visibility region concept takes care of modeling the number of clusters in an implicit manner.

environment changed more rapidly than in the LOS measurements, where the TX and RX were both in the hall. In GSCMs, this behavior can be controlled by adjusting the sizes of the cluster visibility regions: the smaller the region, the shorter the cluster lifetime.

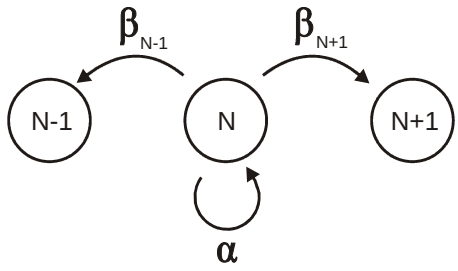

Figure 3.10. Illustration of the principle in which the evolution of number of clusters is presented as a Markov process. In the different states, N denotes the number of active clusters, and α and β represent the probabilities that the number of clusters stays the same or changes.

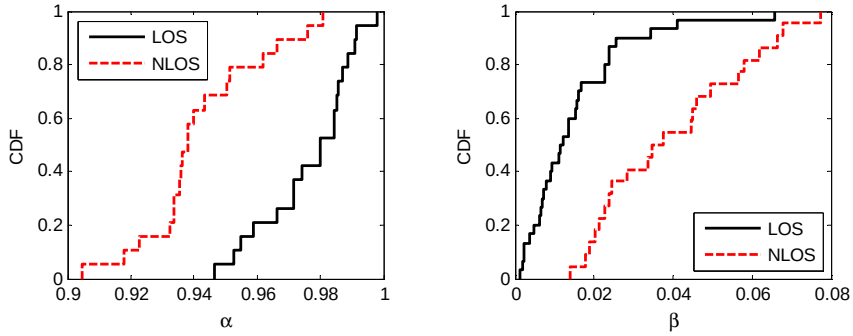

Figure 3.11. The CDFs of the probability that (a) the number of clusters stays the same and that (b) the number of clusters increases of r decreases when moving from a snapshot to the next one.

4 Parameterization and validation of COST 2100 channel model

One of the most attractive features of the geometry-based channel models is that the same model structure can, in principle, be used to model the radio wave propagation in all possible environments. This makes also the programming of the channel model implementation relatively convenient, since basically an unlimited number of different scenarios can be simulated with a single code; only the input parameters have to be set differently for the different scenarios.

Unfortunately, probably the most severe bottleneck in all the existing GSMCs has turned out to be exactly the parameterization of the different scenarios. Since channel sounding measurement campaigns are extremely laborious and expensive, no one can, in practice, measure all the possible scenarios. Furthermore, to derive the full set of parameters needed by a comprehensive GSCM based on the measurement data is a cumbersome task in itself. In many cases a practical way to parameterize a channel model scenario has been to combine available parameter values from various existing publications – and, to be honest, guess the remaining ones – to form a full parameterization. The problem in this approach is that results from different measurement campaigns are not always fully comparable with each other due to several reasons. First of all, different researchers may use different measurement systems and data post-processing tools, for instance different parameter estimation algorithms or clustering methods. In addition, the definitions of the cluster parameters in different publications may not always be exactly the same as that in the channel model implementation at hand. Hence, to compile parameter sets by collecting pieces from various sources is not a recommendable alternative for a high-quality GSCM.

On top of the parameterization, another severe issue in geometry-based channel models is the lack of thorough validation of the models against measurement data. This is partly due to the shortages in the parameterization, but also because an established way to do the validation does not exist. In fact, it is even hard to choose sufficient or reasonable validation metrics, since what can be considered as “sufficient” or “reasonable” validation, may change a lot depending on the usage of the channel model. Another challenge for a meaningful validation is the selection of an appropriate reference to which the channel model is compared. If the comparison is done between the model and measurement data – as it normally is – it is vital to ensure that the channel model is parameterized fully and exactly based on the measurement data that are used in the comparison.

In this section, the parameter extraction performed in this thesis for the indoor scenarios of the COST 2100 channel model is presented. All the parameters are carefully defined and the meaning of each of them and ways to extract them are also explained as rigorously as possible. Along with the explanations, examples of the parameters extracted from a reference measurement are presented. In addition, the COST 2100 channel model is validated by comparing the channel model output with the measurement based on which the channel model parameters were extracted. The content presented in this chapter is based on publications [4] and [5].

4.1 Scenarios

For the parameterization of the COST 2100 channel model, dual-link measurements were carried out in two different scenarios. As the analyzed measurements included two MS routes measured with a dual-link sounder, altogether four different cases were measured and the total number of measurement samples, i.e. snapshots, was 3600. However, results only for one reference measurement are shown and explained in detail, whereas parameter values for the rest of the scenarios are only listed in the summary tables presented in Appendix A.

4.1.1 Indoor hall with LOS conditions

The measurement in the first scenario was carried out in the Computer Science (CS) building, in Aalto University School of Science and Technology, Espoo, Finland. The measurement venue is a three-storey office building with a large hall that occupies the whole height of the building in the middle of it. The floor plan of the measurement venue is shown in Figure 4.1(a). In the measurement, BS1 (Aalto RX, see Section 3.1 for details) was located on a balcony on the second floor and BS2 (LU RX) on a bridge that connected the two sides of the building on the second floor. The MS (LU TX) was moving along a balcony on the hall side of the second floor having a LOS connection to both BSs throughout the measurement route. Below, parameters are explained based on measurement MS – BS1 of this scenario.

4.1.2 Office corridor with NLOS conditions

The venue for the second measurement scenario was the office corridor of the Department of Radio Science and Engineering (RS), located also in Aalto University School of Science and Technology. The floor plan of the measurement venue is shown in

Figure 4.1(b). In this case, the MS was moving along a corridor towards a T-junction, and the two BSs were located on opposite sides of the perpendicular corridor seen from the MS, as shown in Figure 4.1(b). In this measurement, links between the MS and both BSs had NLOS conditions for the whole route.

4.2 Parameterization of the reference scenario

The parameters that are needed to characterize clusters in the COST 2100 channel model are divided into three classes: 1) inter-cluster parameters, 2) intra-cluster parameters, and 3) cluster location parameters. The inter-cluster parameters describe the global cluster settings, e.g. the total number of cluster and their relationships with each other. The intra-cluster parameters, on the other hand, are necessary in order to describe how the MPCs are arranged within each cluster thus specifying the internal structure of the clusters. Cluster location parameters define how the clusters are located in the simulation coordinates.

All the parameters have been extracted by first applying the EKF parameter estimation algorithm [87] and then clustering the MPCs obtained by the EKF algorithm with the MBRT [1]. At this time, only the mean and standard deviation of the extracted parameters are given meaning that the theoretical distributions the parameters might obey have not been further analyzed. This approach was considered appropriate due to the fact that in the COST 2100 channel model, certain distributions have been already selected for each parameter, partly based on previous observations and partly due to implementation issues. In addition, the theoretical distribution a certain parameter might obey based on a single measurement, as long as being a sensible one, is not likely to significantly affect the quality of a GSCM.

Figure 4.2 shows the EKF parameter estimates of the DoD, DoA and delay as a function of the location of the MS (in snapshots) in the reference measurement. The LOS component is the dominant propagation mechanism throughout the MS route in this scenario. However, several clusters originating from reflections from different walls are also alive for most parts of the measurement route.

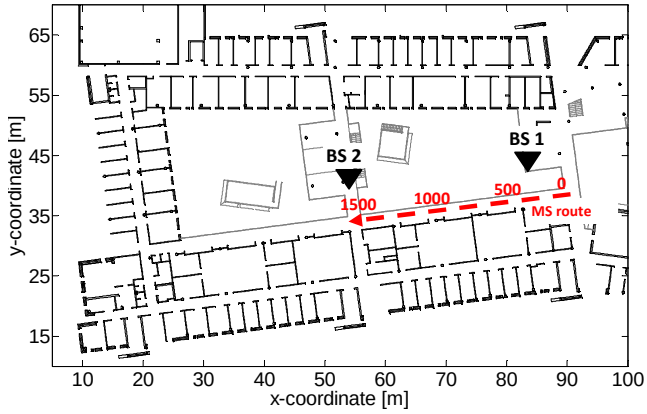

(a)

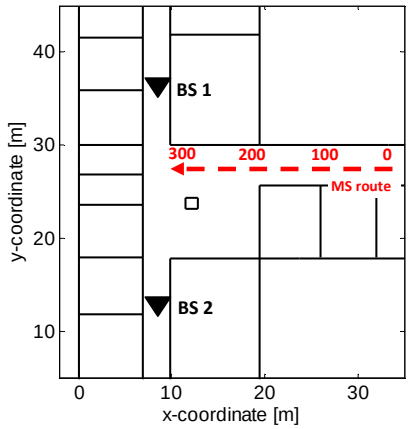

(b)

Figure 4.1. Floor plans of the measurement environments with MS routes and BS positions. (a) Measurement done in the Computer Science (CS) building. This measurement represents a scenario *Indoor hall with LOS conditions.* (b) Office corridor scenario in Department of Radio Science and Engineering (RS). This measurement represents a scenario *Office corridor with NLOS conditions.*

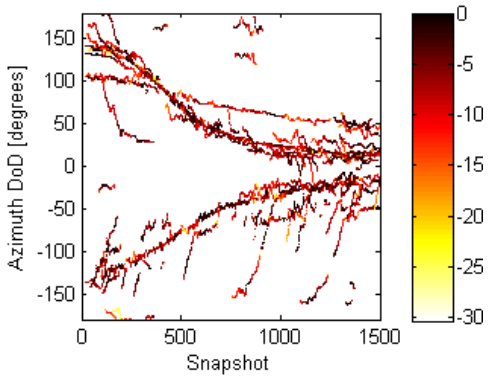

(a)

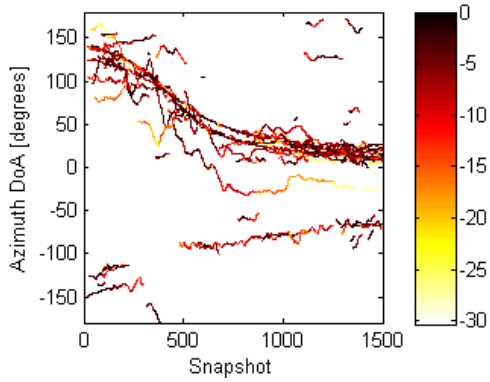

(b)

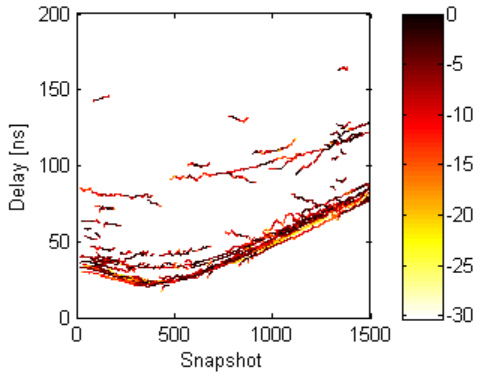

(c)

Figure 4.2. EKF parameter estimates for the (a) azimuth DoD and (b) DoA, and (c) delay for the measurement MS – BS1 in the indoor hall scenario.

4.2.1 Inter-cluster parameters

The following inter-cluster parameters were extracted from the measurement data:

- Number of clusters N_{C}
- Radii of the cluster visibility regions r_{VR}
- Cluster selection parameter K_{sel}
- LOS power factor K_{LOS}
- Cluster power decay factor k_{τ}
- Cluster shadow fading *SF*

Number of clusters and radii of VRs

In the COST 2100 channel model, the number of clusters is implicitly determined based on the concept of VRs: each cluster is assigned with a VR and the corresponding cluster is active only when the MS is inside the VR. The total number of active clusters is thus specified by the number of VRs inside which the MS is at each time instant. The concept of VRs is in that sense intelligent that, in addition to the instantaneous number of active clusters, the dynamic behavior, i.e. the appearance and disappearance of the clusters, is simulated in a realistic manner.

Owing to the visibility region concept applied in the COST 2100 channel model, values for two parameters need to be adjusted based on measurement data in order to simulate the number of clusters and its dynamic behavior in a realistic manner: 1) Mean number of active clusters, and 2) the lifetimes of each cluster, i.e. the radii of the VRs. Figure 4.3 (a) shows the number of active clusters as a function of snapshot in the reference scenario. The number of active clusters varies between 2 and 6, the mean and the standard deviation being 3.69 and 0.78, respectively. The results were similar also in other measurement scenarios. The radii of the VRs were calculated simply by translating the lifetimes of the clusters to meters and dividing the result by two. Since the lifetime of the cluster is equivalent to the diameter of the VR, it has to be divided by two to get the radius. The CDF of the VR radii is shown in Figure 4.3 (b). The mean and standard deviation of the VR radii are 2.72 m and 2.28 m.

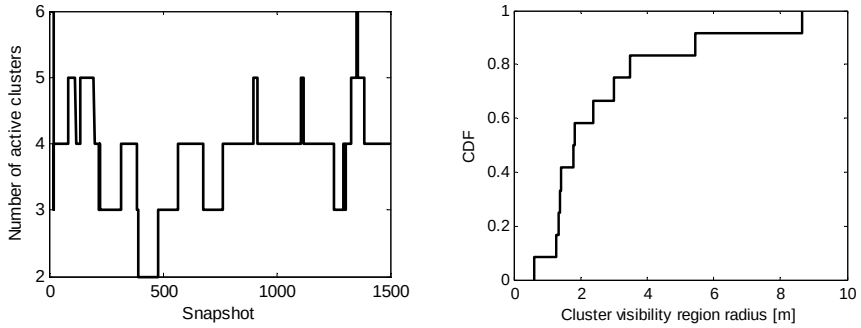

(a) (b)

Figure 4.3. Total number of active clusters as a function of the MS location. (b) CDF of the visibility region radius.

Cluster selection parameter

The COST 2100 channel model includes the option to distinguish between the single- (SBCs) and multiple bounce clusters (MBCs)[3]. This improves the accuracy of the model, since different cluster types can be assigned with different parameters. The ratio of SBCs and MBCs is denoted by the so called cluster selection factor K_{sel}:

$$K_{\mathrm{sel}} = \frac{N_{\mathrm{SBC}}}{N_{\mathrm{SBC}} + N_{\mathrm{MBC}}}, \tag{4.1}$$

where N_{SBC} and N_{MBC} are the number of SBCs and MBCs. Thus, $K_{\mathrm{sel}} = 1$ means that all clusters are SBCs and $K_{\mathrm{sel}} = 0$ that all clusters are MBCs.

Figure 4.4 (a) shows the cluster selection parameter K_{sel} as a function of snapshot in the reference measurement. Values for the K_{sel} are in the range between 0.3 and 1, and the mean and standard deviation are 0.70 and 0.19. That is, on average 70 % of the clusters are SBCs. Figure 4.4 (b) shows the power carried by the SBCs and MBCs in [%] of total power. It can be seen that the SBCs are significantly stronger than the MBCs in this scenario. It was found in the analysis done with the MBRT that in the RS building measurements all the clusters are MBCs, i.e. $K_{\mathrm{sel}} = 0$ in both links. Owing to the fact that is unlikely that in complex indoor environments with NLOS conditions the waves are

[3] MBC is often called *twin cluster* in the COST 2100 channel model, and includes the SBC as a special case where the twin pair overlaps.

able to reach the receiver by one interaction, it is recommended that the K_{sel} is always set to zero in indoor NLOS scenarios.

In the COST 2100 channel model, the ratio between the SBCs and MBCs is modeled only by the K_{sel} meaning that the power composition of different cluster types is not controlled. However, this may lead to overestimate the power carried by the MBCs in scenarios where SBCs are significantly stronger than MBCs, as was the case in this scenario.

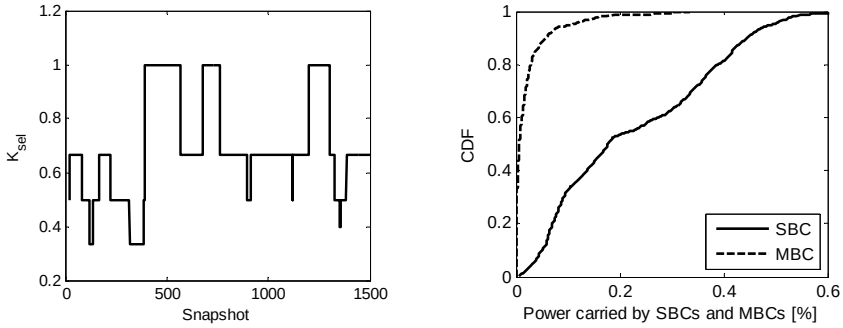

(a) (b)

Figure 4.4. (a) The cluster selection factor representing the ratio of single and multiple bounce clusters. (b) Power carried by SBCs and MBCs.

LOS power factor and cluster decaying

In the COST 2100 channel model one of the most fundamental properties that significantly affects the modeling results is to accurately adjust the power composition between the different propagation mechanisms. This is determined based on the LOS power factor K_{LOS}, which denotes the power of the first arriving MPC (i.e. the LOS component in many cases) compared to the power of all other components. The second parameter describing the cluster power model is the cluster decay factor k_{τ}, which settles the power of the clusters as a function of delay. The LOS power factor K_{LOS} is defined as the ratio of the power of the LOS component (or the first arriving MPC) and the power of all other MPCs, as

$$K_{\mathrm{LOS}} = \frac{P_{\mathrm{LOS}}}{P_{\mathrm{tot}} - P_{\mathrm{LOS}}}, \tag{4.2}$$

where P_{LOS} is the power of the LOS component and P_{tot} is the total power. The unit of K_{LOS} is [dB]; 0 dB means that the LOS component represents half of the total power. Figure 4.5 shows the LOS power factor in the reference measurement. It can be seen that K_{LOS} fluctuates generally between -5 dB and 5 dB. The mean and standard deviation of K_{LOS} are 0.37 dB and 2.77 dB, respectively.

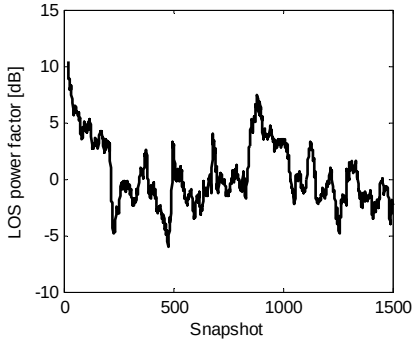

Figure 4.5. LOS power factor in the reference scenario.

The power carried by each cluster is a function of the delay; basically, the longer the delay, the weaker the cluster power is. In the COST 2100 channel model, the power of the *m*-th cluster P_m is modeled as a function of delay as

$$P_m = P_0 e^{-k_\tau(\tau_m - \tau_0)}, \tag{4.3}$$

where P_0 is the power of the LOS component, k_τ is the cluster decay factor, τ_m is the delay of the *m*-th cluster, and τ_0 is the delay of the LOS component. That is, the attenuation of the clusters is always determined with respect to the LOS path (or to the first arriving MPC). Cluster decay factor k_τ describes how rapidly the power of the clusters decays as a function of the propagation delay. The unit of k_τ is [dB/μs]. Figure 4.6 (a) shows an example of extracting k_τ. It is obtained by calculating the slope of the attenuation trend determined by the cluster power delay profile. Cluster decay factor is plotted for the reference measurement as a function of snapshot in Figure 4.6 (b). Typically, the values for k_τ are between 30 and 80 [dB/μs], the mean value being 54 [dB/μs]. It is interesting to see that in two locations around snapshots 300 and 500 the cluster decay factor is actually below zero dB meaning the power of clusters actually increases as the delay increases. This phenomenon is likely to occur in situations when the total number of active clusters is small, and if the cluster with the smallest delay is experienced deep shadow fading.

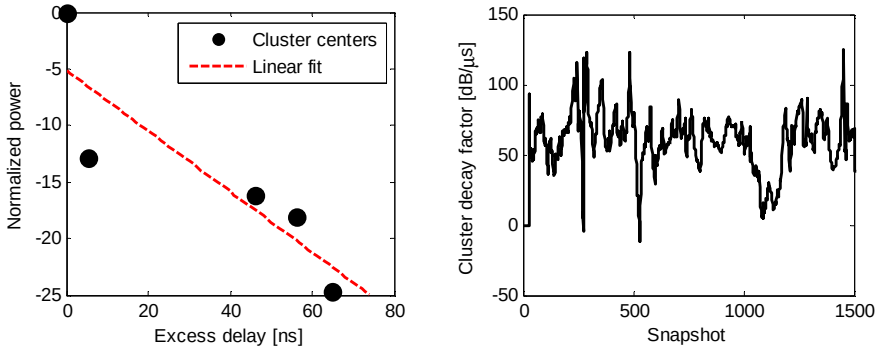

(a) (b)

Figure 4.6. a) Example of determining the cluster decay factor at a single snapshot. (b) Cluster decay factor as a function of snapshot.

Cluster shadow fading

Cluster shadow fading tells how much the power of a cluster fluctuates around its mean during the lifetime of the cluster. Figure 4.7 shows the CDF of the cluster fading in the reference measurement. The CDF in Figure 4.7 includes data from all identified clusters from the whole measurement route. In this case, the standard deviation of the cluster fading was 4.85 dB.

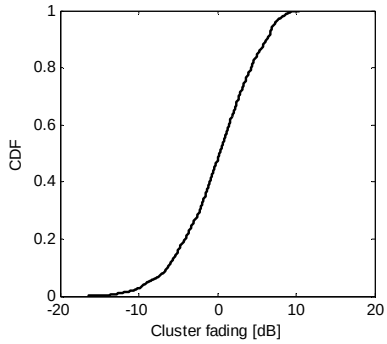

Figure 4.7. CDF of cluster shadow fading in the reference measurement. The CDF include data from all clusters of the whole measurement route. 0 dB corresponds to the mean power of the cluster during its lifetime.

4.2.2 Intra-cluster parameters

The following intra-cluster parameters have been extracted in this section:

- Number of MPCs within clusters N_{MPC}
- Cluster angular spread *AS*
- Cluster delay spread *DS*
- Cross-polarization ratio *XPR*
- Co-polarization ratio *CPR*

Number of MPCs within clusters

The number of MPCs within clusters is one of the most fundamental factors in determining the internal structure of clusters. It affects the angular and delay spreads of the cluster, and also has an impact on the small scale fading of the cluster power. In this case, the number of MPCs within clusters was calculated by the ratio of total number of MPCs and the number of active clusters at each snapshot. Hence, the number of MPCs within clusters gets also non-integer values in Figure 4.8, which shows the number of MPCs within clusters as a function of snapshot in the reference scenario. It can be seen that the number of MPCs within clusters is rarely more than 5, which is a lower value than what has been previously used e.g. in the COST 273 channel model. The lower number of MPCs per cluster is mainly caused by the EKF algorithm and the clustering method used in this thesis.

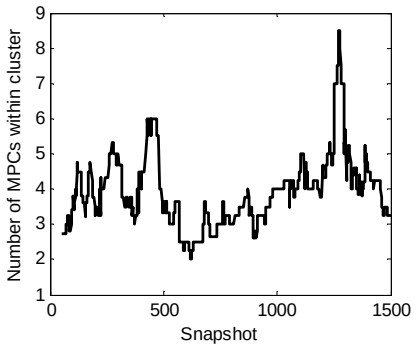

Figure 4.8. Number of MPCs within clusters.

Cluster angular and delay spread

The angular spread (*AS*) and delay spread (*DS*) describe the dispersion the radio channel in angular and delay domains. They can be used in two ways: 1) global spreads indicate how the power in the *total* radio channel is spread over the different domains, whereas 2) the cluster spreads represent the shape of individual clusters. In the COST 2100 channel model, the *AS* and *DS* are used for the latter, i.e. to shape the clusters; locations of the clusters, i.e. the global spreads, are controlled by the cluster location parameters (defined in the following sub-section).

The *AS* and *DS* have been calculated for each cluster based on the measurement data as [96]

$$AS = \sqrt{\frac{\sum_i^N P_i(\varphi_i - \bar{\varphi})^2}{\sum_i^N P_i}} \tag{4.4}$$

and

$$DS = \sqrt{\frac{\sum_i^N P_i(\tau_i - \bar{\tau})^2}{\sum_i^N P_i}}, \tag{4.5}$$

where φ_i is the DoD or DoA of the *i*-th MPC of the cluster, $\bar{\varphi}$ is the mean DoD or DoA of the cluster, and τ_i the delay of the *i*-th MPC and $\bar{\tau}$ is the mean delay of the cluster. *N* is the total number of MPCs within the cluster and P_i is the power of the *i*-th MPC.

Figure 4.9 (a) and (b) show the *AS* (mean over all clusters at each snapshot) in the reference scenario at BS and MS sides, respectively. It can be concluded that the *AS* is typically somewhat larger on the MS side than on the BS side in the reference scenario. A possible explanation to the larger *AS* on the MS side that in this scenario is that the MS was moving very close to the wall which constituted a significant cluster; since the wall is a very large object and the MS was always close to it, the *AS* seen by the MS is naturally large. However, even on the MS side the *AS* rarely gets values of more than 5 degrees. In some cases, the *AS* is zero which means that at those locations the cluster included only one MPC. No noticeable differences were observed between the ranges of the values the *AS*s get in azimuth and elevation planes. As was the case in the *AS*, also the *DS* had rather small values in this scenario. Based on Figure 4.9 (c) it was found that the *DS* is typically between 0 ns and 2 ns in this scenario.

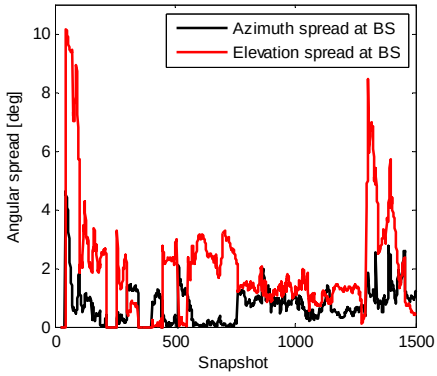

(a)

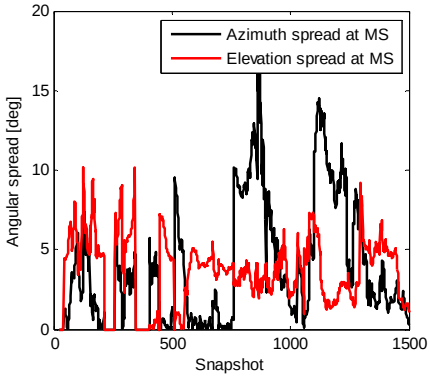

(b)

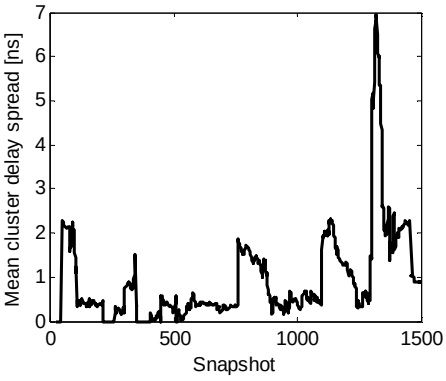

(c)

Figure 4.9. Cluster angular spread at (a) BS and (b) at MS. (c) Delay spread.

Cross-polarization ratio and co-polarization ratio

The cross-polarization ratio (*XPR*) is a parameter which indicates how large a proportion of the signal transmitted with a certain polarization shifts into the orthogonal polarization as it propagates through the radio channel. The *XPR* is calculated for each MPC for signals transmitted with V- and H-polarization as

$$XPR_{\mathrm{V}} = \frac{P_{\mathrm{VV}}}{P_{\mathrm{VH}}} \tag{4.6}$$

and

$$XPR_{\mathrm{H}} = \frac{P_{\mathrm{HH}}}{P_{\mathrm{HV}}}, \tag{4.7}$$

where P_{IJ} is the power of the wave which was transmitted at the *I*– and received at the *J*–polarization. The CDF of the *XPR* in the reference measurement is shown in Figure 4.10 (a). It is seen that in this scenario, there are no noticeable differences between XPR_H and XPR_V, the mean value and standard deviation being approximately 15 dB and 11 dB in both cases. The co-

polarization ratio (*CPR*) describes the differences in the power levels of the different co-polarization components:

$$CPR = \frac{P_{\mathrm{VV}}}{P_{\mathrm{HH}}}. \tag{4.8}$$

In the reference measurement (according to the CDF of the *CPR* shown in Figure 4.10 (b)), the mean and the standard deviation of the *CPR* were 0.88 dB and 6.57 dB, respectively.

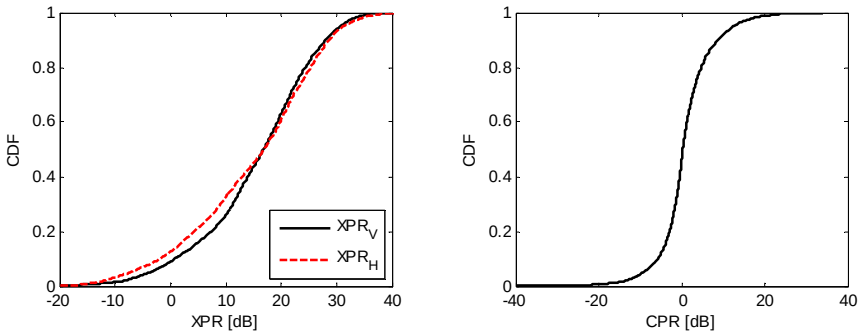

(a) (b)

Figure 4.10. CDFs of the (a) XPR and (b) CPR in the reference measurement.

4.2.3 Cluster location parameters

The cluster location parameters define how the clusters are distributed in the simulation coordinates. Three parameters are defined based on the location of the scatterers in the measurements:

- Link excess delay $\tau_{c,\mathrm{link}}$
- Scatterer delay $\tau_{c,\mathrm{MS/BS}}$
- Scatterer angle $\Psi_{c,\mathrm{MS/BS}}$

Link excess delay $\tau_{c,\mathrm{link}}$ denotes the delay time of intermediate propagation between the first and last scattering point of the MPC. Thus, for the SBCs $\tau_{c,\mathrm{link}}$ is in principle zero. The scatterer delay $\tau_{c,\mathrm{MS/BS}}$, on the other hand, is the delay time between MS or BS and the first or last scattering point. Hence, the total delay associated with the cluster can be expressed as

$$\tau_C = \tau_{C,\mathrm{BS}} + \tau_{C,\mathrm{link}} + \tau_{C,\mathrm{MS}}. \quad (4.9)$$

Scatterer angle $\Psi_{c,\mathrm{MS/BS}}$ is the angle between the line connecting the MS and BS and the line connecting the MS or BS and the first of last scattering point. Figure 4.11 clarifies what is meant by each cluster location parameter.

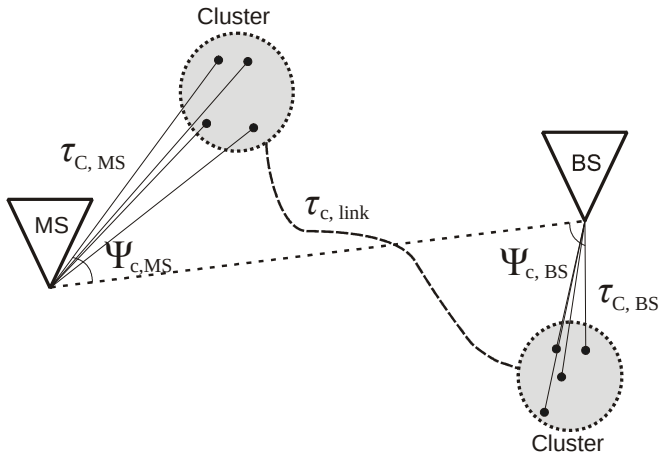

Figure 4.11. Parameters defining the locations of the clusters.

In order to extract the cluster location parameters from the measurement data, the first interaction point after the TX and the last interaction point before the RX have to be determined. This can be done by calculating the intersection point between the ray launched from the TX or RX and the physical object that the launched ray hits first, as illustrated in Figure 3.6. Here, the rays were launched in the MBRT from the TX or RX according to the direction of the DoD or DoA of each MPC.

Figure 4.12 (a) – (c) show the CDFs of the links excess delay, scatterer delay and scatterer angle, respectively. In Figure 4.12 (a) it can be seen that in about 70 % of the cases, $\tau_{c,link}$ is less than 10 ns. These small nonzero values correspond to $\tau_{c,link}$ of the SBCs; even for the SBCs $\tau_{c,link}$ is never exactly zero due to practical inaccuracies in the measurements and MBRT including the maps. However, it can be seen that for the MBCs $\tau_{c,link}$ is typically between 20 ns and 80 ns[4]. The scatterer delay $\tau_{C,MS/BS}$ gets values roughly between 10 ns and 80 ns, as seen in Figure 4.12 (b). No large differences can be seen between the $\tau_{C,MS/BS}$ seen from the MS and BS sides. The scatterer angle Ψ_c (Figure 4.12 (c)) spans the whole range between 0 and 180 degrees, meaning that in this scenario the scatterers are distributed over all possible angles.

[4] In the parameter values listed in Appendix 1, the link excess delay values include only the MBCs.

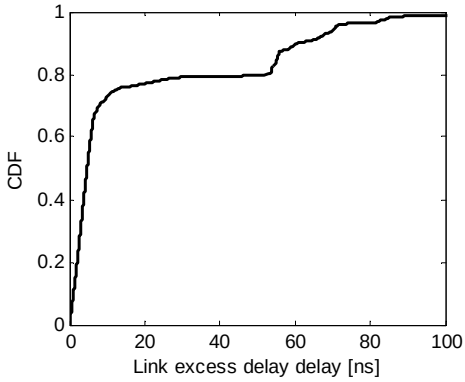

(a)

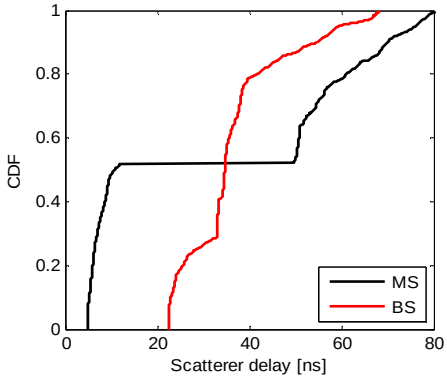

(b)

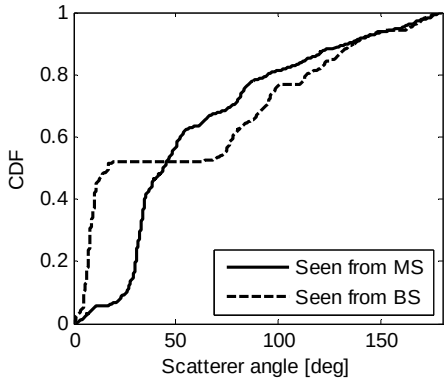

(c)

Figure 4.12. CDFs of the (a) link excess delay, (b) scatterer delay, and (c) scatterer angle.

4.3 Validation

4.3.1 Methodology

In this section, the COST 2100 channel model is validated by comparing the channels obtained from the COST 2100 channel model simulation with the measured channels. The flow chart of the comparison is shown in Figure 4.13. The measurement data were post-processed by the EKF parameter estimation algorithm in order to reconstruct the measured channel by discrete propagation paths for the comparison. On the other hand, the channel realizations generated by the COST 2100 channel model simulations were obtained by inputting exactly the parameters extracted from the corresponding measurement to the model. The channel model implementation code used in the validation was originally written based on the COST 273 model by Hofstetter in [59], complemented by Liu *et al.* in [97], and later refined according to the definitions of the COST 2100 channel model. Two measurement scenarios were selected for the comparison. The first scenario was the MS – BS1 link in the indoor hall LOS measurement shown in Figure 4.1(a). From that measurement, the first 1400 snapshots were considered in the comparison. The second scenario used in the validation was the MS – BS1 link in the office corridor NLOS measurement shown in Figure 4.1(b). In this scenario, first 300 snapshots were used in the comparison.

The channel simulations were made with the same geometrical settings of the BS and MS locations as the corresponding measurements. Otherwise, the randomness of the COST 2100 channel model regarding all of its parts, e.g. random cluster positions and other parameters, was fully maintained. Naturally, closer agreement between the measurement and simulation would have been expected if some random components of the model would have been forced to match between the measurements and simulations. However, with this approach it is possible to investigate the true performance and characteristics of the full COST 2100 channel model, which gives essential information to the possible end users of the model.

The following simplifications were made for the comparison. First, only vertical co-polarized path weights were considered, since a channel model "add-on" for multi-polarization simulation is still under development. It means co-polarized horizontal polarizations and cross-polarization components were not taken into account. Second, local clusters, which are placed around the BS and MS and have uniform angular power spectrum over azimuth angles, were inactivated in the channel simulation because they were not detected in the measurements. Finally, only specular propagation paths were taken into account for the comparison meaning that the dense multipath components were

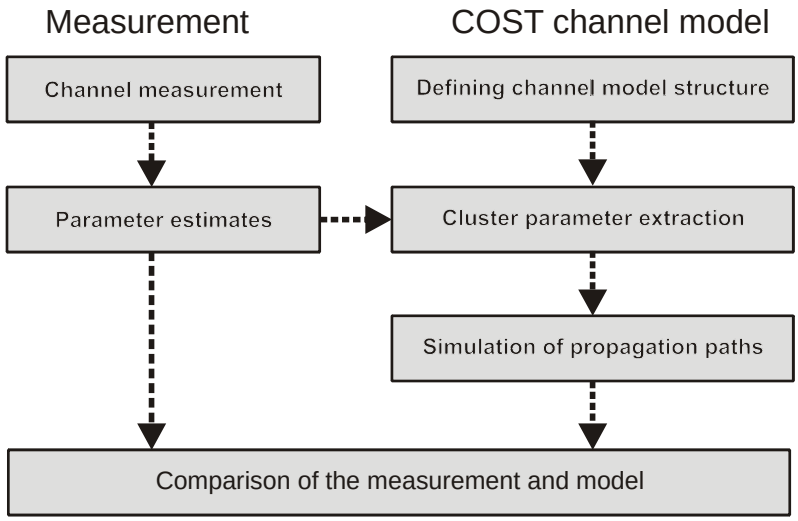

Figure 4.13. Flow chart of the comparison of the COST 2100 channel model against measurement data.

not considered at this time. In the measurement routes used in the comparison, the specular components contained approximately 70% and 10% of the total power on average for the LOS and NLOS scenarios, respectively.

4.3.2 Comparison of delay spread and angular spread

Among many metrics, angular spread and delay spread were chosen for the comparison since they can be derived without considering antennas, and furthermore, they are fundamental and affect other metrics such as eigenvalue and channel capacity distributions. One should note that the *global* delay and angular spreads are used here in the comparison, whereas above in Section 4.2.2 values were presented for the *cluster* spread parameters.

Delay spread

The CDFs of the delay spread from measurement and three independent simulation runs are shown in Figure 4.14. In the LOS scenario (Figure 4.14 (a)), the mean value of the delay spread was 9.0 ns in the measurement, and 5.9 ns, 7.9 ns and 8.1 ns in the simulation runs. In the NLOS scenario (Figure 4.14 (b)), the mean value of the delay spread was 40.4 ns in the measurement, and 71.8 ns, 39.5 ns, and 42.4 ns in the simulations. The first simulation run in the NLOS scenario clearly overestimated the

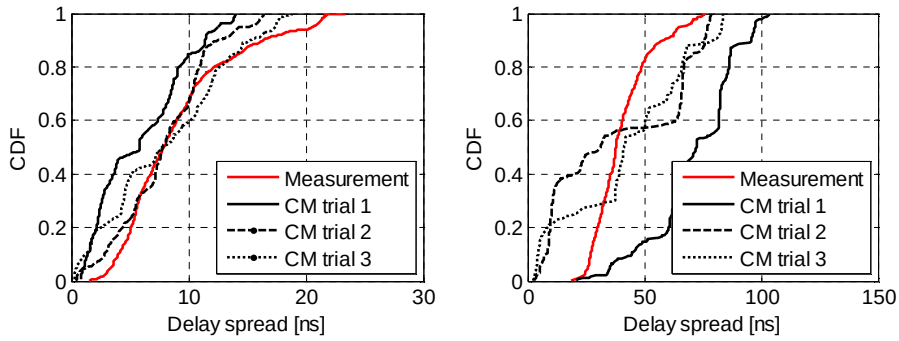

Figure 4.14. Comparison of delay spreads between measurements and the COST2100 model: (a) LOS hall and (b) NLOS corridor scenarios.

delay spread, but in the other trials the agreement between the simulated and measured delay spread was good. The channel simulation output revealed the accuracy of delay spread prediction within the relative error of −35 % to +80 %.

Looking at the CDF curves of Figure 4.14, the following observations can be made. First of all, the curves from the channel model simulations are not as smooth as the curves representing the measurements. This happens possibly because the large scale properties of the channel change drastically due to sudden death and/or birth of clusters along the MS route, since the total number of clusters was relatively small. Another observation that can be made is that the delay spread can vary significantly between different simulation runs. This is, however, inevitable since the number of independent cluster realizations was relatively small during each simulation run.

Angular spread

Comparison of azimuth and elevation angular spreads for channel simulations and measurements are shown in Figure 4.15 and Figure 4.16 for the LOS hall and NLOS corridor scenarios, respectively. The simulation underestimated the angular spread compared to measurements in the LOS hall scenario. The most visible underestimation appeared in the elevation spread on the MS side. The results from the NLOS corridor scenario revealed both over and underestimation of azimuth spread values. Elevation spread agreed well in this scenario. The range of difference between simulations and measurements was −88 % to −22 % in the LOS hall and −54 % to +111 % in the NLOS corridor scenarios.

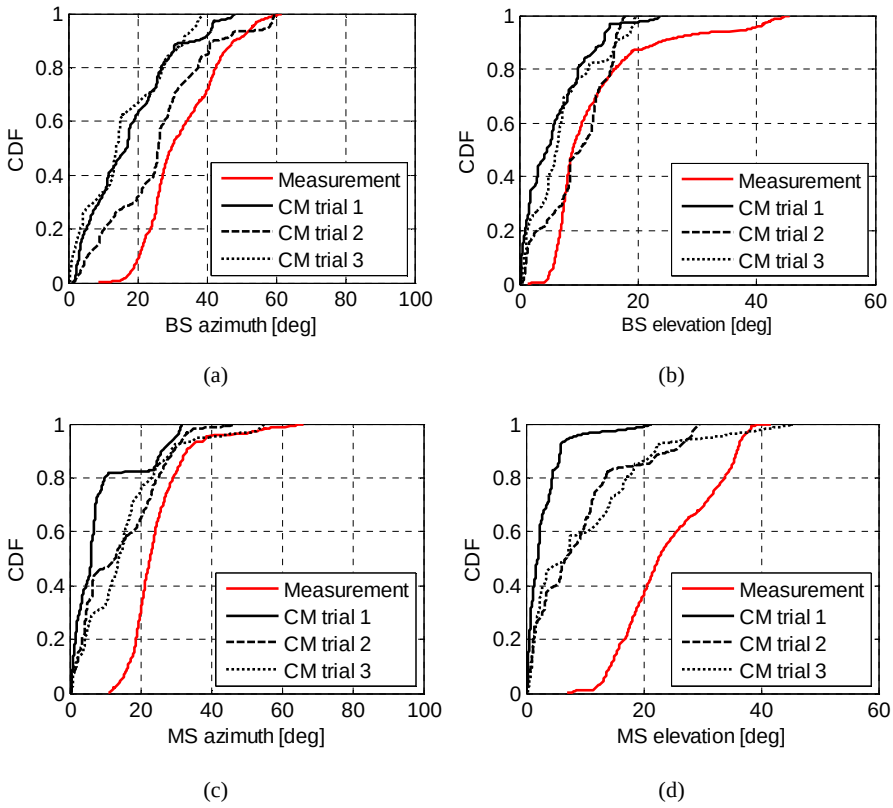

Figure 4.15. Comparison of azimuth and elevation angular spreads between measurements and the COST2100 model in the LOS hall scenario: (a) BS azimuth, (b) BS elevation, (c) MS azimuth, and (d) MS elevation.

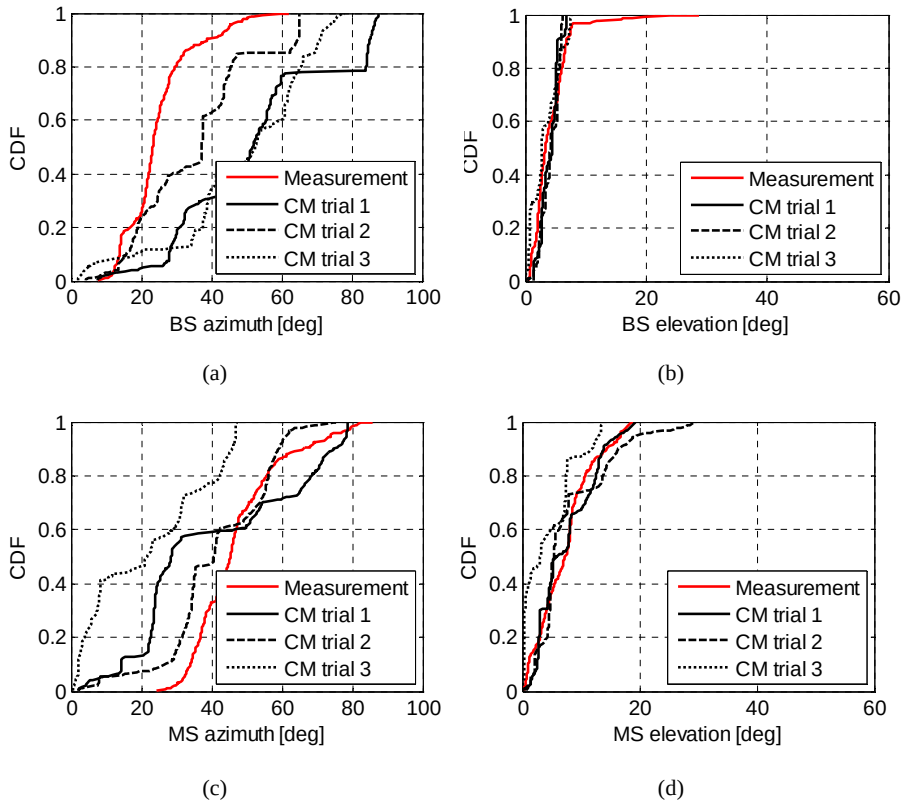

Figure 4.16. Comparison of azimuth and elevation angular spreads between measurements and the COST2100 model in the NLOS corridor: (a) BS azimuth, (b) BS elevation, (c) MS azimuth, and (d) MS elevation.

4.3.3 Discussion

When looking at the results of the validation done above, several questions arise. To begin with, take the meaning of the word "validation". It is commonly understood to stand for "to test whether the channel model is able to model scenarios correctly", but what is meant by "correctly", i.e. how close a match we should get between the channel model and the measurement, is already a much more difficult question. First of all, the answer is dependent on the metrics that are used in the comparison. For instance, if we take mutual information or channel capacity as the validation metrics, we might end up having a perfect match between the measurement and the model even if the physical characteristics of the radio channel would not be reflected at all in a realistic manner. If the user of the channel model is only interested in mutual information or capacity, is this a big problem?

On the other hand, when making a comparison between a GSCM and measurements, the different characteristics of a *stochastic* channel model and a *deterministic* measurement should be kept in mind. Measurement is always purely deterministic meaning that it gives a result only for one unique case, whereas a stochastic channel model should represent all possible cases belonging to the same type of scenarios. This fact makes the validation of a GSCM paradoxical: on one hand, we want to get as close match as possible between the model and the measurement, but on the other, according to the fundamental philosophy of GSCMs the model should include some variation in order to represent a large set of environments. The validation could be performed so that not only the BS and MS but also the clusters would be fixed to exactly the same positions as in the measurement environment. This way the comparison would give a closer match between the simulation and measurement but on the other hand it would be against the nature of GSCMs.

To conclude, validating a GSCM can never be a very rigorous discipline, and therefore, to say anything conclusive about the quality of the COST 2100 channel model is hard based on the validation done above. Perhaps, instead of analyzing how close match the model gives in comparison with a single measurement, a more sensible question when assessing the quality of a channel model would be to ask: Is it possible to find an environment that fits to our model?

Summary of Part II

The development of a GSCM requires four tasks: channel measurements, propagation path parameter estimation, propagation analysis, and model development. In Chapter 3, it was explained how these tasks have been handled in this thesis. As a case of analysis of the characteristics of the radio channels, the number of clusters and the evolution of number of clusters were also studied in Chapter 3. The analyses revealed that generally the number of clusters is larger in LOS than in NLOS scenarios and that, on the other hand, the number of clusters changes more rapidly in the NLOS than in LOS scenarios.

Chapter 4 presented the parameterization of the COST 2100 channel model in indoor scenarios. The parameters were divided into inter-cluster parameters, intra-cluster parameters, and cluster location parameters. Parameter values were extracted in altogether four indoor scenarios including two measurements in an indoor hall scenario with LOS conditions, and two measurements in an office corridor scenario with NLOS conditions. In addition, the COST 2100 channel model was validated in terms of the angular and delay spreads. The validation was performed by comparing two measurements with the channels obtained by COST 2100 simulation when the model was parameterized exactly based on the corresponding measurement.

Part III – Dense multipath components

5 Background

5.1 Specular components and dense multipath components

From the channel modeling perspective, the energy that is transferred by the radio channel from the TX to the RX can be understood to consist of two parts. The first part, i.e. the specular components (SC), is considered to consist of a superposition of individually strongly contributing plane waves that propagate from the TX to the RX via specular-like reflections from large physical objects. The second part, i.e. the dense multipath components (DMC), consists of a large number of weak MPCs originating from e.g. scattering from objects that are either small in size compared to the wavelength, have rough surfaces, or consist of multiple surfaces having different materials. With this interpretation, the full radio channel (**H)** can be simply written as the summation of the parts of the channel classified as the SC ($\mathbf{H}_{\mathrm{SC}}$) and the DMC ($\mathbf{H}_{\mathrm{DMC}}$):

$$\mathbf{H} = \mathbf{H}_{\mathrm{SC}} + \mathbf{H}_{\mathrm{DMC}}. \tag{5.1}$$

Figure 5.1 shows an example of the different propagation mechanisms of the SC and DMC in a case of a single scattering object. In this case, the SC propagates by a strong reflection from the surface of the scattering object. Around the SC there are many weaker components classified as DMC that originate from scattering from the edges of the rough surface and from reflections from the different layers of the object. As a result, a large amount of very closely - or densely - located MPCs representing the DMC arrive at the RX from slightly different angles and at slightly different delay times than the corresponding SC. This simple example shows a typical situation where the SC actually represent the scattering object only by a small number of discrete point sources, whereas the part of the energy classified as DMC scatters from the whole area of the object.

Traditionally, all measurement-based channel models have been parameterized based on parameter estimates obtained from channel measurements. However, a commonly recognized fact is that none of the parameter estimation algorithms, such as SAGE, RIMAX, or EKF, are able to fully characterize the radio channel by the parameter estimates. All these algorithms are based on approximating the radio channel by a superposition of distinct plane waves, i.e. the SC, and omit the residual part of the channel, i.e. the DMC. Even though different estimation algorithms use somewhat different approaches for characterizing the radio channel, the same fundamental problem applies for each of them; due to a limited measurement resolution, practical computational resources, and the fact that the plane wave assumption does not always perfectly hold, resolving all of the huge number of very weak signal components as SC is practically impossible.

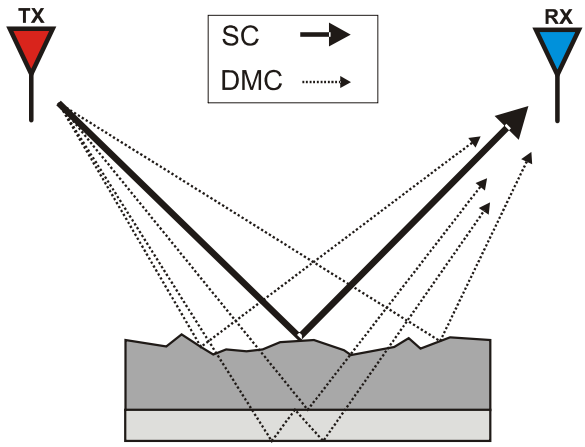

Figure 5.1. Differences in the propagation mechanisms of SC and DMC.

In fact, a rigorous distinction between the SC and DMC is hard to make in the measurement data due to the fact that in reality there is no strict boundary between these two components from the physical perspective. Hence, a common and practical way to make the distinction is to consider the output of a parameter estimation algorithm to represent the SC, and regard the residual power as the DMC. This approach is used also throughout the analyses presented later in this chapter, meaning that the distinction between the SC and DMC is not made explicitly based on their different propagation mechanisms, but simply everything which remains after removing the SC from the measured data is considered as DMC. This actually means that also the direct path (or the LOS component) can, and often does, contribute to the SC. To be more precise, the measured vectorized MIMO channel transfer function is given by

$$\mathbf{x} = \mathbf{x}_{\mathrm{SC}} + \mathbf{x}_{\mathrm{DMC}} + \mathbf{n} \in C^{M_f M_T M_R \times 1}, \tag{5.2}$$

where M_f, M_T, and M_R, denote the number of frequency samples, transmit antennas, and receive antennas, respectively. The $\mathbf{x}_{\mathrm{SC}}$ and $\mathbf{x}_{\mathrm{DMC}}$ represent the parts of the channel transfer functions classified as SC and DMC, and $\mathbf{n}$ is the noise vector. Provided that the signal-to-noise ratio is at a sufficiently high level in the measurement, an estimate for the DMC can be obtained simply by removing the effect of the estimated SC ($\tilde{\mathbf{x}}_{\mathrm{SC}}$) from the full channel ($\mathbf{x}$):

$$\tilde{\mathbf{x}}_{\mathrm{DMC}} = \mathbf{x} - \tilde{\mathbf{x}}_{\mathrm{SC}}. \tag{5.3}$$

Omitting the DMC has been commonly recognized as being one of the most fundamental problems in all measurement-based channel models. The problem in omitting the DMC from the models is that, in addition to underestimating the received power, the multipath richness becomes underestimated, and, accordingly, the impact on the system level is seen as an underestimated channel capacity (see e.g. [99]). Even if the effects of the DMC are known to contribute significantly to the radio channel, a serious effort has not previously been put in adding the DMC to the GSCMs, for which at least a part of the reason has been the lack of thorough understanding on the propagation characteristics of the DMC.

5.2 Earlier works

Previously, several publications have addressed the estimation and analysis of the DMC based on channel measurements, e.g. [86], [87], [99], [100], [101]. On the other hand, an intensive research topic in the field of ray tracing–based propagation prediction tools has been to characterize the roughness of the scattering surfaces to create the distributed scattering in a realistic manner, e.g. [102] – [105]. The first attempts in the characterization of the DMC suggested that the DMC could be modeled with an exponentially decaying structure in the delay domain, and with a white azimuthal angular spectrum [86], [98]. In [99] it was reported that the DMC have a significant effect on the channel capacity and that the contribution of the DMC to the total received power varies significantly depending on the environment; however, the characteristics of the DMC themselves were not discussed in detail in that paper. More recently, procedures for the estimation and analysis of the directional properties of the DMC have also been presented [86], [87], [100]. In [101] it was shown based on outdoor measurements that both uniform and concentrated angular distributions of the DMC can be observed; especially in street canyon-type NLOS scenarios the directional concentration of energy was clear, whereas in LOS cases the angular distribution of the DMC was close to uniform. Even though there have been quite a large number of publications related to the DMC, the focus in the previous works has mainly been on the estimation techniques of the parameters of the DMC rather than on analyzing the actual propagation mechanisms of the DMC based on real measurements; In addition to the results presented in this thesis, detailed propagation analysis of the DMC have been reported only very recently in [106].

6 Characteristics of the DMC

In this chapter, the properties of the DMC are analyzed based on an extensive set of indoor channel measurements. First, the proportion of the DMC in total power is studied in different LOS and NLOS environments, and as a function of the TX – RX distance. In addition, the effects of the shadowing object on the power carried by the SC and DMC are investigated. Furthermore, the angular and delay domain characteristics of the DMC are analyzed and compared with those of the SC. The results presented in this chapter are based on publications [6] and [7].

6.1 Measurement scenarios

The measurement campaign was carried out in the Computer Science Building in Aalto University School of Science and Technology by using the Lund Rusk channel sounder. The building is a three-storey office building with a large open hall in the middle. The hall occupies the whole height of the building and is surrounded by classrooms and offices. Two bridges are connecting the different sides of the building on the second and third floors. The floor plan of the measurement venue is shown in Figure 6.1 (a). In the measurements, the TX moved along continuous routes, acting as a mobile terminal, and the RX was always located at a fixed position, resembling an access point. The TX routes 1 – 5 are marked with dashed red lines and RX positions 1 – 2 with black triangles in Figure 6.1 (a). The walls surrounding the large open hall are marked with "A" –"D". Walls A and D are made of brick and there are many office windows on them. Wall C is made of concrete and also has some windows on it. Wall B is made of metal. Figure 6.1 (b) and (c) show photos of the measurement environment.

Five different TX/RX combinations were measured:

1. In scenario TX1/RX1 (TX route/RX position in Figure 6.1 (a)), the TX was moving close to the RX with LOS conditions except for the location where a concrete pillar shadowed the LOS component close to the middle of the measurement route.
2. In scenario TX2/RX1, the RX was located in the same place as in the first scenario, but in this case the TX moved along a balcony next to wall C.
3. In scenario TX4/RX1, the TX moved along a bridge that connects the two sides of the building on the second floor. In the middle of this route, stairs

between the bridges of the second and third floor shadowed the LOS component as can be seen in Figure 6.1 (c).

4. In scenario TX5/RX1, the TX moved along an office corridor. Since the RX was located in the hall also in this scenario, there were NLOS conditions throughout the measurement route.

5. In scenario TX3/RX2, the TX moved along a balcony on the third floor, and the RX was located on the opposite side of the hall in the corridor on the second floor. Along the route TX3, there were concrete pillars between the balcony and the hall, as seen in Figure 6.1 (c).

The measurement scenarios are summarized in Table 6.1:

Table 6.1. Summary of measurement scenarios

Scenario	**Floor level (TX/RX)**	**Snapshots**	**Conditions**	**Shadowing objects**
TX1/RX1	2/2	1800	LOS	Pillar around snapshot 700
TX2/RX1	2/2	3000	LOS	-
TX4/RX1	2/2	900	LOS or obstructed-LOS	Stairs around snapshot 550
TX5/RX1	2/2	2500	NLOS	-
TX3/RX2	3/2	2200	NLOS	Pillars at constant intervals

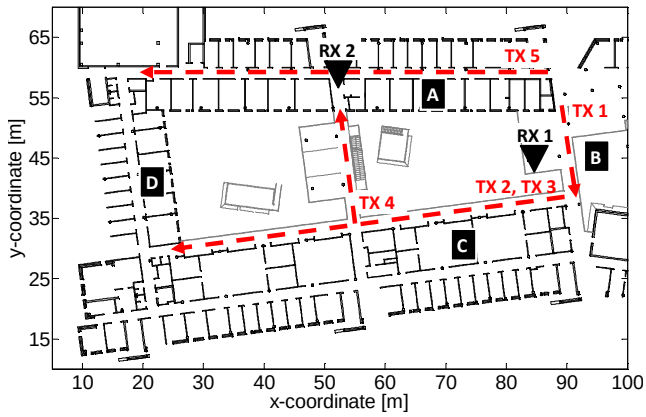

(a)

(b)

(c)

Figure 6.1. (a) Floor plan of the measurment venue with the TX routes (dashed red lines) and the RX positions (black triangles). (b) Measurement environment seen from the bridge connecting the two sides of the building and (c) from the balcony above RX 1.

6.2 Proportion of DMC in total power

Probably the most fundamental factor in the characterization and modeling of the DMC is to know how large proportion of the total power is carried by the DMC in different environments. This section discusses the proportion of DMC in total power in several indoor scenarios, including both LOS and NLOS cases, and additionally, investigates the dependency of the proportion of DMC on the distance between the TX and RX. Finally, the effects, that shadowing objects have on the SC and DMC, are studied.

6.2.1 Proportion of DMC in LOS and NLOS environments

The total received power, and the powers carried by the SC and by the DMC are presented for scenarios TX1/RX1, TX4/RX1 and TX3/RX2 in Figure 6.2 (a)-(c), respectively. In scenario TX1/RX1, the SC contribute significantly to the total received power, and the power carried by the DMC is typically in the order of 3 – 8 dB below the power of the SC. Only around snapshots 700 – 750, where the pillar shadows the LOS component, the SC and DMC have roughly equal powers. The effect of the pillar is not clearly visible in the power carried by the DMC. In scenario TX4/RX1, the SC and DMC contribute roughly equally except for the location where the stairs shadow the LOS component (around TX locations 450 – 600). At that location, the power of the SC is approximately 4 – 6 dB below the DMC. Neither in this case, is the shadowing of the stairs seen in the power carried by the DMC. In scenario TX3/RX2, the power carried by the SC is generally in the order of 5 – 10 dB below the power of DMC. Thus, this measurement shows an extreme example of a scenario where the SC actually represent only a small minority of the propagated energy. Different from the previous two scenarios, the degradations in the received power caused by concrete pillars are present in both the SC and DMC, showing that also the part of power classified as DMC can be affected by physical objects located in the vicinity of the antennas. Obviously, if the shadowed signal component represents a significant proportion of the total DMC power, the influence of the shadowing object can be seen also in the DMC, as is the case with the pillars in scenario TX3/RX2. On the other hand, in case the un-shadowed signal paths (such as reflections and scattering from other objects) are relatively stronger, it is possible that the degradation in the power level caused by a shadowing object is not visible in the total DMC power, which is the case with the stairs in scenarioTX4/RX1.

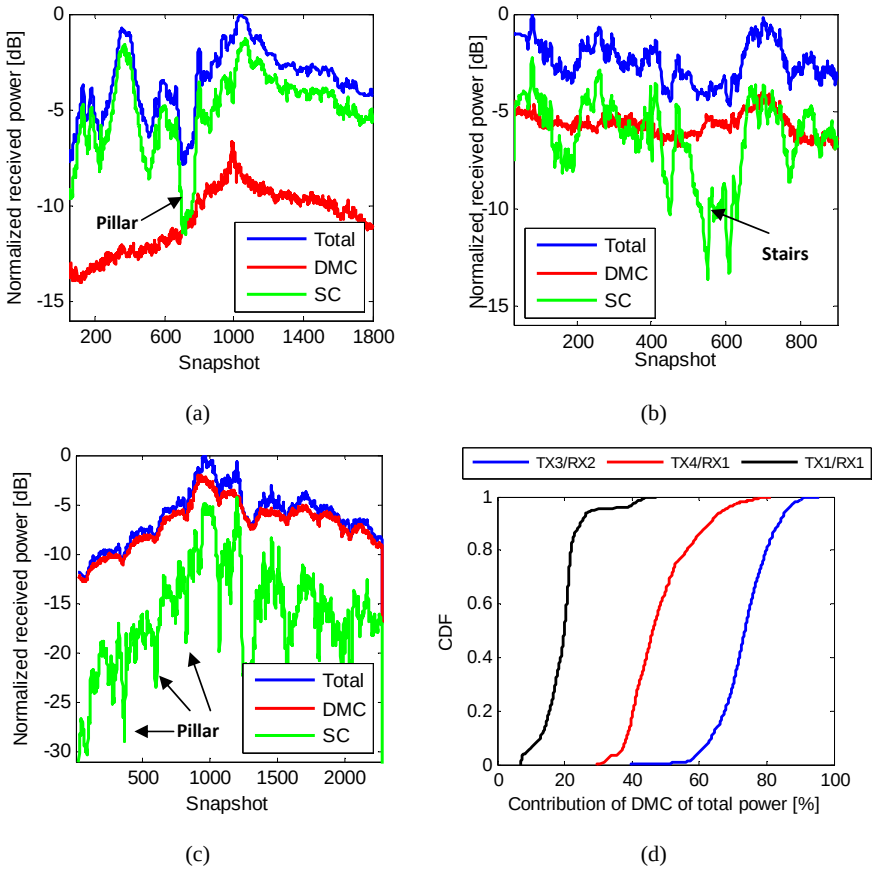

Figure 6.2. Total received power and power carried by the specular propagation paths and DMC normalized to the maximum total power in scenario (a) TX1/RX1, (b) TX4/RX1, and (c) TX3/RX2. (d) The CDFs of the contribution of DMC to total power in the different scenarios.

Figure 6.2 (d) shows the CDFs of the proportion of DMC in total received power (in [%]) for scenarios TX1/RX1, TX4/RX1 and TX3/RX2. In scenario TX1/RX1 the proportion of DMC in total power is between 10 % and 25 % for the majority of time. Larger shares of approximately 30 – 45 % can be observed rarely, only in the location where the concrete pillar shadows the LOS component and the power carried by the SC also drops rapidly. In scenario TX4/RX1 the DMC represent typically from 35 % to 65 % of the total power. A plausible reason for the higher proportion of DMC in scenario TX4/RX1 than in scenario TX1/RX1 is that the longer distance between the TX and RX attenuates the LOS component faster than the reflected MPCs; as the TX – RX distance increases, the path loss of the LOS component increases faster than the path loss of the MPCs reflected from walls, and as a result, the level of DMC relative to the total power increases. In scenario TX3/RX2, the DMC represent approximately 60 % – 90 % of total power.

6.2.2 Proportion of DMC as a function of TX – RX distance

As shown above, the proportion of DMC in total power can vary significantly from one environment to another; in general, the proportion of DMC in total power is higher in scenarios with NLOS than with LOS conditions. In addition, it was shown that in LOS scenarios the proportion of DMC in total power can increase as the distance between the TX and RX increases. In order to elaborate the dependency of the proportion of the DMC on the TX – RX distance, the proportion of DMC was studied in two scenarios (TX2/RX1 and TX5/RX1) where the TX – RX distance changed gradually.

The proportion of DMC in scenarios TX2/RX1 (LOS conditions) and TX5/RX1 (NLOS conditions) as a function of TX – RX distance is shown in Figure 6.3 (a) and (b), respectively. In scenario TX2/RX1, the proportion of DMC increases from about 20 % in the beginning of the TX route to about 40 % in the end of the route. In the middle of the route, in locations where the TX – RX distance is roughly 20 meters, the proportion of DMC increases rapidly by approximately 20 %-units. A similar rapid increase can be seen at TX – RX distances of approximately 30 meters. A possible reason for the increased proportion of DMC in these locations is that the bridge under which the TX moves around the middle of the route might cause some scattering thus increasing the relative amount of DMC. The trend in the increase in the amount of DMC is in this scenario 0.45 %-units/m.

In scenario TX5/RX1, the proportion of DMC is about 35 % in the very beginning of the route, thus being quite similar to the scenario TX2/RX1, which had LOS conditions. The slope of the linear fit is 0.20 %-units/m in this region. However, the proportion of DMC starts to increase rapidly soon after the TX – RX distance exceeds 20 meters. Between TX – RX distances of approximately 20 and 35 meters the proportion of DMC fluctuates a lot, and actually this region can be considered as a transition region from an obstructed LOS to a true NLOS. After the TX – RX distance exceeds 35 meters the increase in the proportion of DMC starts to be almost linear having the trend of 0.29 %-units/m. At the end of the route practically all the power is DMC. The rapid increase in the relative amount of DMC in total power after TX – RX distances of 20 meters is presumably caused by the fact that as the TX travels away from the RX, the number of walls that the waves need to penetrate gets larger. On the other hand, the large fluctuation in the amount of DMC is attributed to differences in the shadowing of the direct path at different snapshots: in locations where the power proportion of DMC is low, the direct path is obstructed less than in locations where the proportion of DMC is high. Since the direct path always contributes significantly to SC, attenuation of the direct path increases the relative strength of other propagation mechanisms, such as scattering from walls, furniture, etc., thus increasing the relative amount of DMC in total power. The results

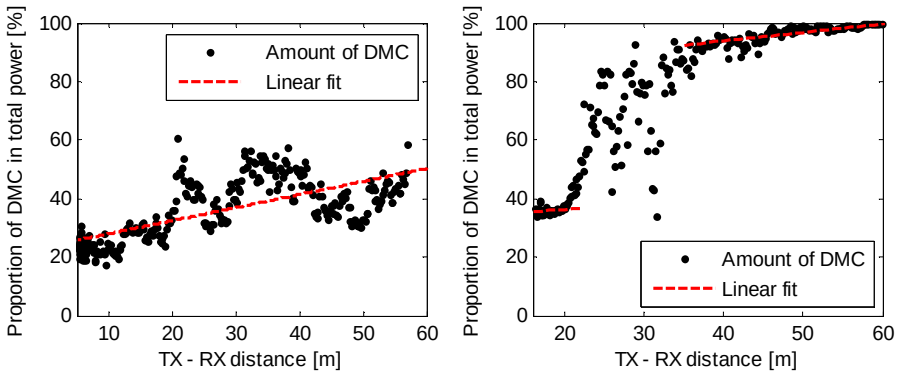

(a) (b)

Figure 6.3. The proportion of DMC as a function of TX – RX distance. (a) Scenario TX2/RX1 (LOS). In this environment, the increase in the amount of DMC is 0.45 %/m. (b) Scenario TX5/RX1 (NLOS). The increase in the amount of DMC is 0.20 %/m in the region where the TX – RX distance is less than 22 meters and 0.29 %/m in the region where the TX – RX distance is more than 35 meters.

shown in Figure 6.3 show that even though increasing the TX – RX distance seem to have an increasing effect on the relative amount of DMC, the effects caused by other factors in the environment (such as LOS/NLOS conditions, scattering objects, etc.) are more dominant.

To verify the assumption that the rapid fluctuation in the proportion of DMC is caused by differences in the obstruction of the direct path, the power angular profiles (PAPs) of the channel at the TX and RX are plotted in a polar coordinate system on top of the map of the environment at snapshots 1050 and 1100 (corresponding to approximately 27 m TX – RX distance) in Figure 6.4. The PAPs were obtained by Bartlett beamforming [87]. At snapshot 1050 the proportion of DMC in total power was 43 %, and at snapshot 1100 86 %. It is seen in Figure 6.4 that the direct path is significantly weaker at snapshot 1100 than at snapshot 1050, whereas the waves reflected from the south wall are almost at the same level at both snapshots.

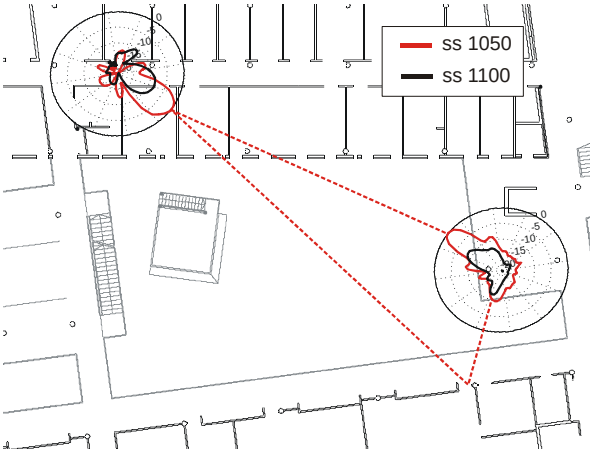

Figure 6.4. PAPs of the total power at snapshots 1100 and 1050. The direct path is attenuated significantly at snapshot 1100 whereas the power of the cluster reflected from the wall is almost at the same level at both snapshots. As a result, the ratio of DMC in total power increases significantly from snapshot 1050 to 1100.

6.2.3 Shadowing of the SC and DMC

As noticed above, SC and DMC seem to behave differently against fading caused by shadowing objects. In order to obtain deeper understanding, the effects of the shadowing objects on SC and DMC were studied by analyzing the degradation in the received power level at TX locations behind the shadowing object as depicted in Figure 6.5 (a). Two measures were used to characterize the shadowing effects for the SC and DMC: 1) the shadowing level (SL), i.e. the degradation of power caused by the object, and 2) the offset distance (OD), i.e. the distance from the location where the TX is exactly behind the object to the location where the maximum SL was observed. The SL and OD were extracted by studying the received power level degradation as the TX passes behind the shadowing object at different normalized DoD azimuth angles Ψ. The normalized DoD angle $\Psi = 0°$ corresponds to the angle where the shadowing object is on a line connecting the TX and RX, as shown in Figure 6.5 (a).

An example of extracting the SL and OD is shown in Figure 6.5 (b). In this case, the SL was –2.9 dB and the OD –0.5 m for the DMC with $\Psi = -20$ degrees, as represented by the dotted black curve. Figure 6.5(c) shows the SL and OD for the range of Ψ from –40 to 40 degrees for the pillar around snapshot 700 in scenario TX1/RX1. The color of the markers in Figure 6.5(c) shows the SL, whereas the OD is depicted by the value in the y-axis. The dashed lines are linear fits to characterize the trend of the OD. The SL is higher for the

SC than for the DMC, and the maximum SL is always observed at $\Psi = 0°$ and at OD = 0 m. The highest SL values for the SC are approximately 15 dB, whereas for the DMC the SL is between 2 and 4 dB. It is interesting to notice that even though the pillar did not cause visible degradation in the level of the total DMC power in this scenario (red curve in Figure 6.2(a)), the shadowing effect can anyway be as much as approximately 4 dB at the DoDs pointing towards the pillar. As can be expected, the SL gets lower as the normalized DoD gets further away from 0 degrees. The range of the OD is wider in the DMC than in the SC as the normalized DoD Ψ changes, as seen by the steeper slope in the linear fitting to the OD trend in Figure 6.5(c). Based on the results, it can be concluded that the shadowing behaviors of the SC and DMC are different: even though the SL is much higher in the SC than in the DMC, the shadowing effect lasts longer in the DMC than in the SC. A possible explanation to this phenomenon is that since DMC consist of a large amount of weak random components, it is likely that not all of them are shadowed at the same time.

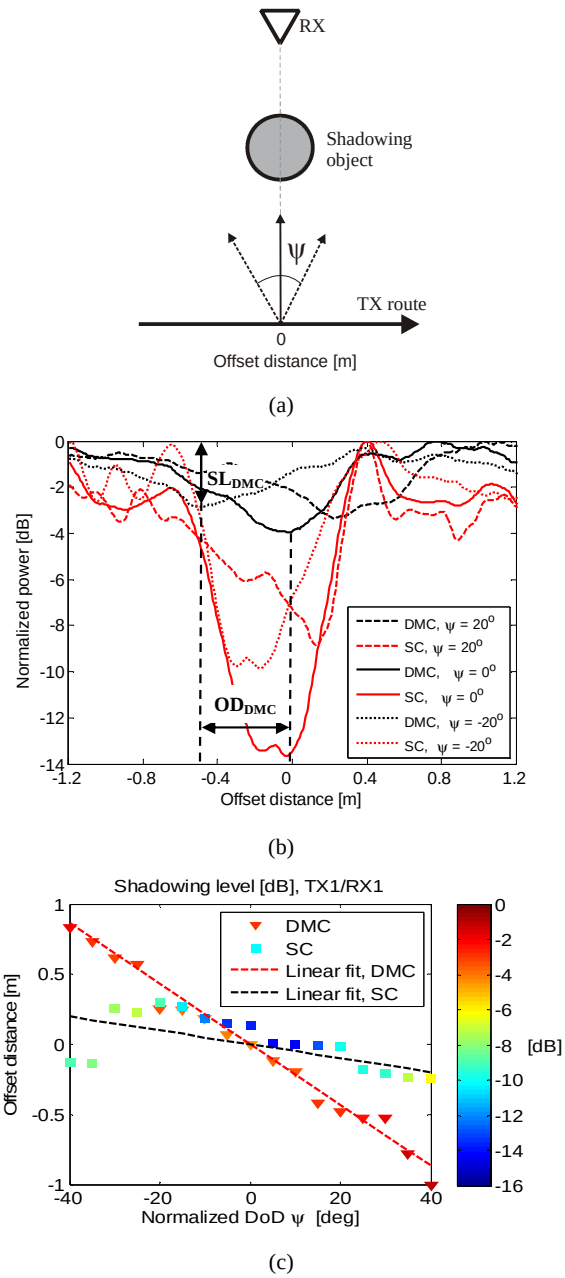

Figure 6.5. Determining the shadowing level (SL) and offset distance (OD). (a) Schematic. (b) Example in the case of the pillar in scenario TX1/RX1. (c) Shadowing level (SL) and offset distance (OD) at different normalized DoDs in the case of the pillar in scenario TX1/RX1.

6.3 Behavior of the DMC in angular and delay domains

As shown above in Section 6.2, the proportion of DMC can be basically anything between approximately 5 and 95 % depending on the environment. Hence, it is quite evident that channel models that do not take DMC into account fail, in general, to predict the full characteristics of radio channels. However, in order to be able to include the DMC to the channel models, information about the proportion of DMC in total power is not sufficient alone, but more in-depth understanding of the propagation characteristics of the DMC is needed.

6.3.1 Propagation mechanisms of SC and DMC

In order to get insight about the propagation mechanisms of the DMC, PAPs were calculated separately for the SC and DMC by applying Bartlett beamforming [87] in angular domain and averaging over the delay domain. In Figures 6.6 (a) and (b), examples of PAPs in scenarios TX4/RX1 and TX3/RX2 are plotted in a polar coordinate system on top of the map of the measurement environment. This way it is possible to combine the directional data with physical objects in the environment, and the different propagation mechanisms can be clearly seen in both the SC and DMC. Figures 6.7 (a) – (d) show the PAPs (TX azimuth) of the SC and DMC as a function of the measurement location in scenarios TX4/RX1 TX3/RX2. The PAPs were normalized by the maximum level at each snapshot. In this way, the variations of the total received power are suppressed, whereas the evolution of the directional properties of the channel can be seen more clearly. Since no noticeable differences were observed between the V- and H-polarizations, they were summed up in the presented PAPs. It is worth noticing, that this analysis focuses on the main propagation mechanisms of the DMC (e.g. from which walls waves reflected) with a relatively low-resolution method; taking these facts into account it would actually be quite surprising to see significant differences between the polarizations. In addition, as the DMC is noise-like in nature, it is likely that no noticeable differences exist between different polarizations.

As a general note, the PAPs presented in Figure 6.7 reveal that large similarities can be found between the angular distributions of the SC and DMC in the investigated scenarios. Based on these results it is fair to conclude that even if the contribution of the DMC in the total power changes a lot, no significant angularly white spectrum seems to exist. Even though the different propagation mechanisms are more concentrated in the SC due to the discrete nature of the SC, in many cases similar mechanisms can be found also in the DMC. Hence, the main propagation mechanisms of both SC and DMC seem to be usually related with the same physical scattering objects. It is worth noticing that this trend holds regardless of environment and regardless of the proportion of the DMC in total power.

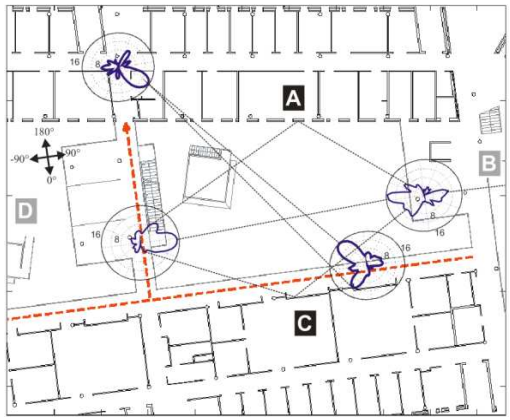

(a)

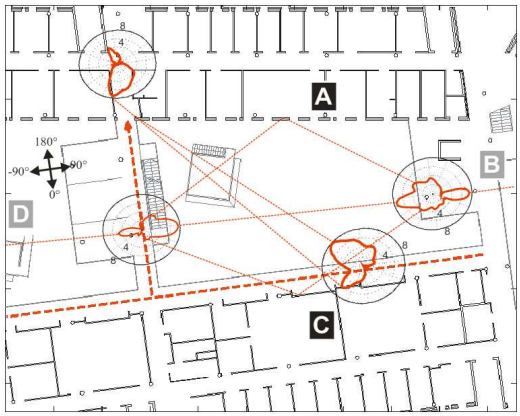

(b)

Figure 6.6. Example PAPs plotted in a polar coordinate system on top of the map of the environment in scenarios TX2/RX1 and TX3/RX2. (a) SC and (b) DMC. Plausible propagation mechanisms are also skecthed on top of the map.

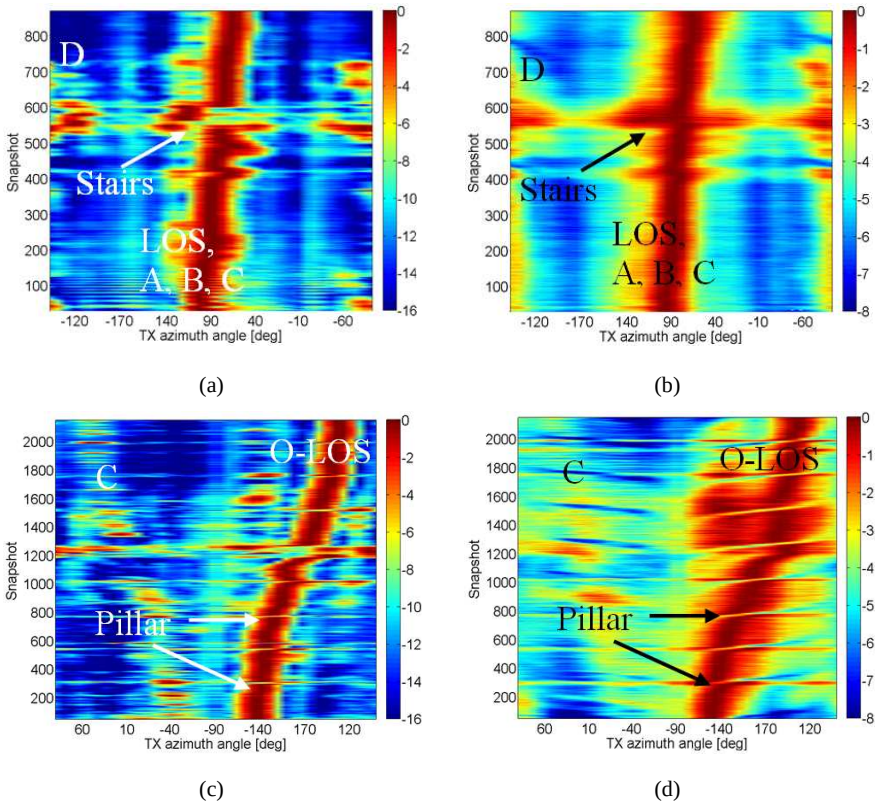

Figure 6.7. The power – angular profiles (TX azimuth) normalized to their maximum value separately for each snapshot (a) for the SC in scenario TX4/RX1, (b) for the DMC in scenario TX4/RX1, (c) for the SC in scenario TX3/RX2, and (d) for the DMC in scenario TX3/RX2.

6.3.2 DMC clusters in angular and delay domains

Figure 6.8 (a) shows a representative example of a power-angular-delay profile (PADP) of the total power (SC + DMC) in scenario TX5/RX1. At this location, the relative amount of DMC in total power was approximately 60 %. Three clusters can be clearly identified at RX azimuth angles of approximately -100, -160 and 90 degrees, the corresponding delay times being approximately 60, 100 and 150 ns. Figure 6.8 (b) shows the PAPs of the clusters separately for the SC and DMC at the delay time of the maximum of each cluster. It can be seen that in all cases, the clusters are located at the same angles in both SC and DMC. The power level between the peaks is higher in DMC

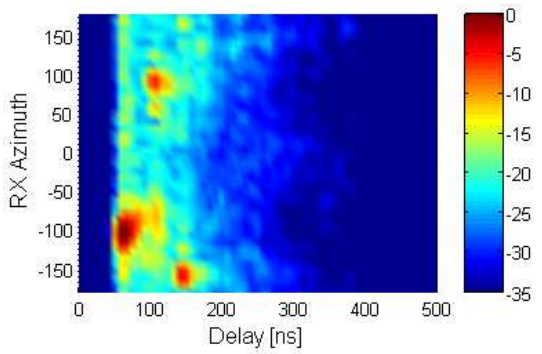

(a)

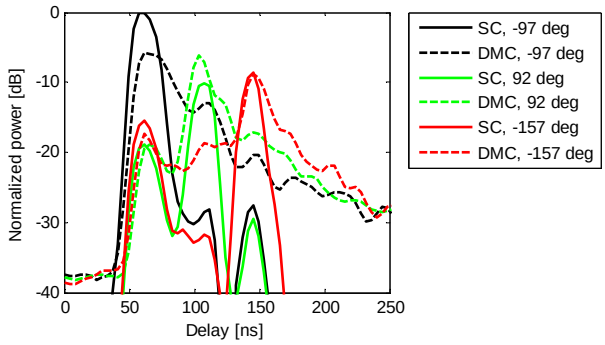

(b)

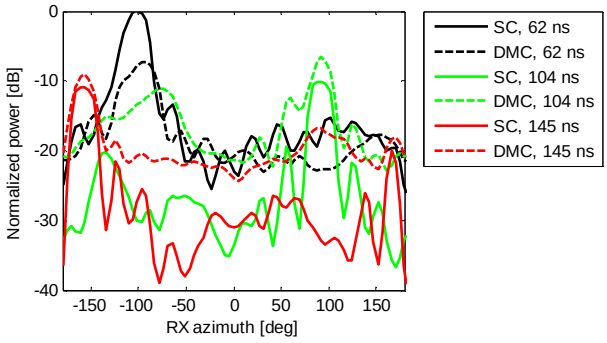

(c)

Figure 6.8. (a) Power-angular-delay profile of the total power. (b) Power-delay profiles of SC and DMC calculated at the RX azimuth angle corresponding to the maximum of each detected cluster. (c) Power-angular (RX azimuth) profiles of SC and DMC calculated at the delay time corresponding to the maximum of each detected cluster. All profiles have been calculated at snapshot 500 in scenario TX5/RX1 and normalized to the power of the strongest cluster.

than in SC at clusters 2 and 3. Figure 6.8 (c) shows the PDP of the clusters separately for SC and DMC at the angles of the maximum of each cluster. The energy of the DMC always has a peak at the same delays as the SC. However, each cluster seems to decay much slower in the DMC than in the SC, which is an implication of the more complicated scattering processes of the DMC in comparison with the SC.

6.4 Discussion

Even if the analyses done in this chapter considered only a single building, just changing the scenario from LOS to NLOS caused the relative amount of DMC to increase from about 10 % to more than 90 %. Therefore, we can conclude that, depending on the environment, the proportion of DMC in total power can be basically whatever between 0 % and 100 % and, quite evidently, this fact challenges the quality of any channel model that omits the DMC.

In this chapter, a further step to enable incorporating the DMC in current channel models was taken by analyzing the propagation characteristics of the DMC. The main conclusion that can be drawn from these analyses is that large similarities can be found between the behaviors of the SC and DMC in both angular and delay domains suggesting that the propagation mechanisms and the scattering sources are actually quite similar in both SC and DMC, which is in good accordance with the results of [106]. This finding is an extremely important one when it comes to the modeling of the DMC, since it suggests that the DMC could be added to the GSCMs just by manipulating the spread parameters of the existing clusters in angular and delay domains instead of attempting to create a fully detached part for the DMC. How this is done in practice, appears in the following chapter.

7 Adding DMC to geometry-based channel models

In this chapter, a method to include the DMC in GSCMs is presented. The basic idea is based on the observations made above in Chapter 6 that there are large similarities between the propagation mechanisms of the SC and DMC. Hence, based on these conclusions a natural approach is to relate the DMC part of the power to each cluster just by adding MPCs around the SC clusters to represent the DMC.

Based on the results shown in Chapter 6, the part of the channel model representing the DMC should have the following properties:

- The power of the DMC should be concentrated around the same angles as the SC. However, the energy in the DMC should be spread over a wider range than the SC.
- In the delay domain, the DMC clusters should have the same base delays as the corresponding SC. However, the DMC clusters should obey a slowly and exponentially decaying PDP.
- The peak power and the slope of the decaying of the DMC clusters should be adjusted so that the ratio between the powers carried by the SC and DMC would be similar to the measurement results.

Next, it is explained how the MPCs are generated for each cluster so that a desired behavior is obtained in angular and delay domains. The approach presented in this section is based on publication [9].

7.1 Angular domain

Usually in GSCMs, the radio channel is generated by dropping clusters, i.e. groups of MPCs, into the simulation environment. The coordinates of individual MPCs belonging to the same cluster are positioned within an ellipsoidal area according to a truncated random distribution around the cluster center, as shown with the black squares inside the solid circles in Figure 7.1. In the modeling approach presented here, the MPCs of the DMC are dropped randomly around the centroid of the SC cluster, but within an area greater than that of the SC. The MPCs for the DMC are distributed within the area that has the same center point than the SC cluster and the radius of r_{DMC}, as shown in Figure 7.1. The resulting response of the DMC in the angular domain is thus concentrated around the same angles as in the SC, however, with a wider angular spread. The parameter value for the r_{DMC} needs to be adjusted based on measurements.

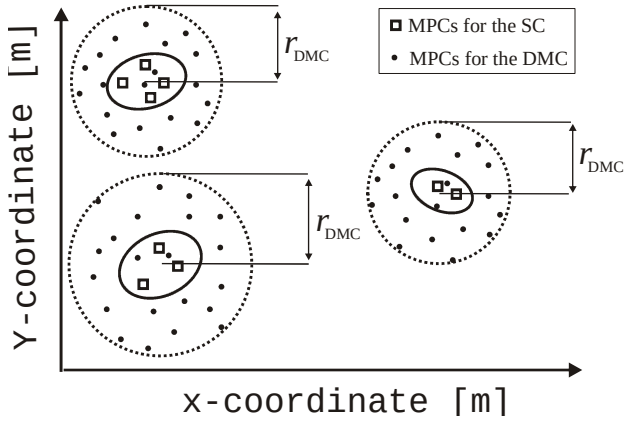

Figure 7.1. Illustration of the method to include DMC to the GSCMs. In spatial domain, the MPCs of the DMC are placed around the SC clusters with a wider distribution than that of the SC. The resulting angular distribution of the DMC is naturally wider than that of the SC.

7.2 Delay domain

In order to achieve a desired behavior for the DMC in the delay domain, each MPC of the DMC is associated with an additional delay on top of the delay determined by the geometry, i.e. the cluster position. This is necessary, since, according to the observations made above in Chapter 6, the DMC part of clusters decays much slower than that of the SC due to more complicated scattering processes. Hence, the delay time of the MPCs of the DMC can be expressed by

$$\tau_{\mathrm{DMC}} = \tau_{\mathrm{DMC,geometrical}} + \tau_{\mathrm{DMC,additional}}, \tag{7.1}$$

where $\tau_{\mathrm{DMC,geometrical}}$ is the delay coming from the geometry and $\tau_{\mathrm{DMC,additional}}$ is a random additional delay that is added to each MPC of the DMC. The additional delay for the DMC is determined so that the DMC part of the clusters obeys an exponentially decaying PDP, as shown in Figure 7.2. *The base delay* of the DMC clusters is determined by the centroid of the SC cluster, and *the slope of the decaying* is extracted from measurements. *The peak power* of the MPCs for the DMC can fluctuate and be higher or lower than the power of the corresponding SC. The MPCs for the DMC in delay domain are obtained by generating Poisson-distributed random delay taps in the range starting at the base delay and ending at the delay time where the power of the DMC has decayed to a sufficiently low level. The delay range for the DMC needs to be limited in order to avoid

complex and time-consuming simulations. One should note that according to the geometrical conditions (see Figure 7.1), the DMC can have a smaller delay than the centroid of the SC cluster; this can, however, be easily avoided in the implementation of the mode by adjusting $\tau_{\mathrm{DMC,additional}}$ if considered necessary. The MPCs for the DMC are generated densely in the spatial domain, and hence also in the delay domain; however, the PDP of the DMC will be sampled according to the delay resolution defined by the system bandwidth. Finally, DMC for the local cluster with a uniform angular distribution and a low power decay factor is added (the local cluster is not shown in Figure 7.1 for clarity's sake). In this way it is possible to model also the propagation paths that are not regarded as SC clusters, i.e. the MPCs that have uniform and random angular distribution and also clusters that are weak for instance due to long delays.

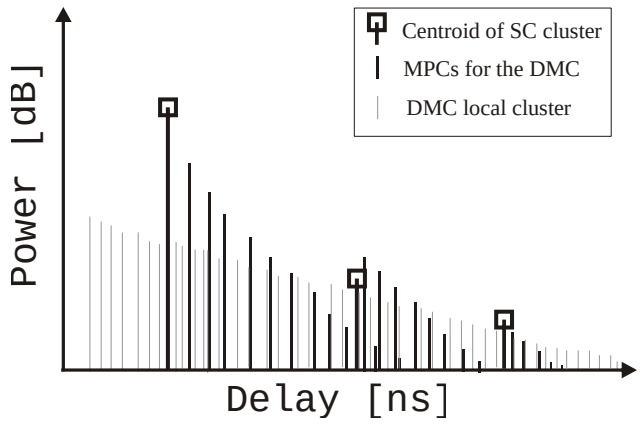

Figure 7.2. In delay domain, each MPC of the DMC is associated with an additional delay in order to achieve exponential decaying for the DMC part of each cluster.

7.3 Parameterization

In order to extract parameters for the DMC in the angular and delay domains, the DMC need to the extracted from the measured power-angular-delay profile (PADP) of the DMC. The PADP for the DMC can be obtained by removing the effect of the SC from the measured channel impulse response (CIR) and by applying beamforming for the residual part of the CIR. In this section possible procedures of how the extract the parameters for the DMC from measurement data are presented. At this time, the parameter values are not provided, but only the possible procedures to determine them based on measurement data are discussed. Hence, the extraction of the DMC cluster

parameters and the validation of the proposed modeling methodology are left to be covered in future research.

In order to generate DMC clusters with a desired response in the angular domain, information about the sizes of the areas within which the MPCs for the SC and DMC are distributed is needed. In the case of the SC clusters, the MPCs are distributed so that the resulting angular spreads of the clusters match with the ones observed in measurements. For the DMC, however, this cannot be straightforwardly done since it is not possible to get distinct MPCs for the DMC from the measurements. To overcome this issue, the following procedures are proposed.

1. *Angular spectrum–based approach.* The DMC part of the clusters can be identified from the measurement data based on the PAP calculated through beamforming of the residual (i.e. DMC) part of the channel. Then, the concentration parameters of, e.g., the Von Mises distribution can be determined for each cluster, as was done in [106]. The concentration parameters of the DMC are related with the angular spreads of the SC clusters, and this information can be used to distribute the MPCs representing the DMC.
2. *Physical scattering point–based approach*. Scattering points of physical objects can be identified for the MPCs of the SC by combining the measured signal directions with a map of the environment [1]. Accordingly, the area within the MPCs of the SC are distributed can be determined. By discretizing the PAP of the DMC obtained by beamforming, the same procedure can be applied for the DMC part of the channel and thus obtain r_{DMC}.
3. *Trial and error–based approach*. Since reliable parameter values for the r_{SC} and r_{DMC} are obviously difficult to obtain based on measurements, one possibility is to find values with which a good match between a measurement and a simulation is obtained based on some validation metrics, e.g. delay spread, angular spread, eigenvalue distribution or channel capacity. This kind of an approach was successfully used for finding appropriate parameters for DMC clusters in [8].

In the delay domain, the following three parameters are needed in order to include the DMC to the GSCMs: 1) *The base delay*. According to previously reported results [7], [106], the base delay of the DMC is the same as the delay time of the SC cluster. 2) *The peak power* of the DMC to be included is determined based on the difference between the estimated peak powers of the SC and DMC. 3) *DMC cluster decay factor* is determined based on the slope of the decay of the DMC extracted from measurements.

7.4 Benefits of the proposed modeling approach

To include the DMC directly to each cluster by additional MPCs has the following benefits. First of all, the biggest advantage of the proposed approach is that there is no need to create new, possibly complicated, concepts (such as the one proposed in [106]) or make any significant changes to the existing GSCMs since their structure fully supports the proposed inclusion of the DMC. Hence, the implementation of the proposed method is not a challenging task. In addition, the time evolution of the DMC is inherently modeled based on the geometry and the visibility regions, as is the case for the SC. A possible drawback of the approach to include the DMC to the clusters is that the number of MPCs becomes large, which may lead to time-consuming simulations. However, the total number of MPCs can be finally restricted by the sampling rate of the system, and, on the other hand, methods to facilitate fast computation of a large amount of MPCs have been also developed, see e.g. [107].

Summary of Part III

The DMC represent the part of the radio channel that cannot be characterized by a superposition of distinct plane waves. The DMC consist of a large amount of closely located MPCs, and even if they are individually weak, together they can contribute significantly to the real-world radio channels.

In this part, it was shown based on measurements that the proportion of DMC in total power can vary significantly from one environment to another, and that the proportion of DMC is generally higher in NLOS than in LOS environments. It was also shown that the relative amount of DMC increases as the TX – RX distance increases, in LOS and NLOS alike; however, impacts caused by other factors (LOS/NLOS conditions, scattering objects, etc.) were found to be more dominant on the relative amount of DMC than the TX – RX distance. In addition, large similarities were found between the propagation mechanisms of the SC and DMC. In particular, it was shown that in the angular domain the energy is concentrated around the same angles in SC and DMC. However, the DMC are spread over a wider angular range. In delay domain, the minimum delay times of the DMC part of each cluster are similar to those of the SC; however, each DMC cluster seems to obey an exponential power delay profile.

Finally, a method to include the DMC to the GSCMs was presented according to the revealed characteristics of the DMC. The basic idea of the modeling approach is to add MPCs representing the DMC around the SC clusters, but within a wider area than the SC. In delay domain, each MPCs of the DMC is assigned an additional delay time in order to achieve the desired exponential power delay profile for each DMC cluster.

Part IV – Multi-link MIMO channel modeling

8 Why do we need multi-link channel models?

So far in this thesis, all the radio channel characterization and modeling have handled the channel between a single BS and a single MS, or more generally, between a single transmitter and a single receiver. However, since many of the envisioned wireless communication systems either operate under heavy interference due to densely populated networks, and/or base their operation on utilizing agile communications between multiple nodes in the network, modeling only the single-link properties of the radio channels is clearly no longer sufficient. Examples of systems where it would be very beneficial to have realistic multi-link channel models are macro diversity, relay schemes, and indoor localization applications.

One might imagine that a multi-link channel model could be constructed simply by adding up multiple single-link channel realizations. In GSCMs, this assumption actually does hold to some extent, since the basic structure of the GSCMs allows simulations of multi-link scenarios simply by dropping multiple BSs and/or MSs into the simulation environment. However, since clusters and the corresponding visibility regions have been traditionally generated separately and independently for each BS – MS link, there has not been any guarantee that the multiple links reflect the important features of the multi-link scenarios realistically. In particular, the essential feature that should be modeled as accurately as possible is the correlation between different links, since in many cases underestimating the correlation between different links would end up overestimating the overall system performance.

Previously, correlation between different links has been investigated based on measurements in several publications. For instance, it was shown by Kaltenberger *et al.* in [108] that different links may encounter remarkable inter-link correlation when the units are in close proximity to each other. In [108], it was also shown that the spatial correlation between the different links deteriorates the performance of spatial multiplexing in multi-user MIMO systems in terms of throughput. In [11], [12], [17], [13], and [14] it has been shown that links may be highly correlated even if they are largely separated in distance. On the other hand Czink *et al.* showed in [109] that two links may also have very different inter-link correlation even if they are in the same environment, e.g. in the same room. It is obvious, that a true need exists for extending current channel models to be able to reflect these properties realistically.

Part IV of this thesis is dedicated to discussing how to extend current GSCMs to support multi-link simulations. To begin with, physical propagation phenomena that affect the correlation between different links, i.e. the inter-link correlation, are discussed in Chapter

9. In Chapter 10, the methodology of how to extend current GSCMs to support multi-link simulations is presented. The presented multi-link GSCM is based on the concept of common clusters, meaning that the inter-link correlation is controlled by forcing a predetermined proportion of power to propagate via the same clusters in the different links. Issues that are needed to take into account when implementing the multi-link extension of the COST 2100 channel model based on the concept of common clusters are also discussed in Chapter 10. Finally, the capability of the developed modeling approach to control the inter-link correlation is evaluated in Chapter 11. The content presented in Part IV is mainly based on publications [10] – [17].

9 Physical phenomena causing inter-link correlation

As we have learned, GSCMs construct the radio channel on the basis of imitating the real-world physical propagation phenomena by clusters. Therefore, for the development of multi-link GSCMs, it is essential to have understanding about the physical propagation phenomena that increase correlation between different links. In fact, this is of course true for all other aspects in channel modeling as well; if there is no information about the physical phenomena that are intended to be modeled, it is impossible to develop a model describing the phenomena in detail.

This chapter is dedicated for discussing the physical phenomena that are likely to increase the inter-link correlation in order to provide the fundamental basis for the construction of multi-link geometry-based channel models later in Chapter 10. The discussions of the physical phenomena that affect the inter-link correlation are based on observations made in extensive dual-link measurement campaigns. The measurement results, based on which this chapter has been written, have been previously reported in publications [10] – [14].

9.1 Geometry of the environment

In certain situations, the geometry of the environment can have a large impact on the correlation between different links. For instance, the most trivial situation is shown in Figure 9.1(a) where two MSs happen to be located very close to each other; here it is very probable that the scatterers seen by the different MSs are very similar thus making it hard for the BS to separate the MSs[5]. In a situation shown in Figure 9.1(b), on the other hand, one MS has difficulties separating the directions of the two BSs even though the BSs are separated by a considerable distance, since the two BSs happen to be located on the same line from the MS point of view.

[5]A situation where two BSs would be very close to each other may, of course, in principle exist. However, usually networks are designed so that BSs of neighboring cells are separated by a considerable distance to ensure efficient coverage in the network.

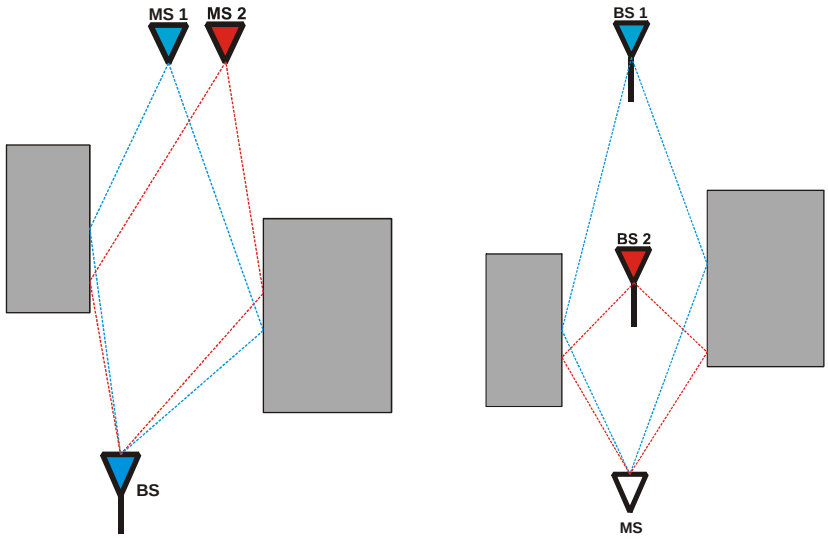

Figure 9.1. The geometry of the environment affects the correlation between different links.

In [10], the radio wave propagation mechanisms were investigated in an environment equivalent to the case in Figure 9.1(b). The measurement was carried out in Computer Science Building in Aalto University School of Science and Technology. In the measurement, the MS was moving along a corridor and two BSs were located in a hall, as seen in Figure 9.2. Two important findings were made based on the analyses: 1) The waves usually propagated through wall A, rather than propagating along the corridor and round Corner 1, and 2) the propagation paths seen by the MS were similar for both BSs including obstructed LOS component and reflections from walls B and C.

The inter-link correlation has been analyzed for similar environmental geometries also in [13] and [15]. In [15], high inter-link correlation values were observed in a scenario where the BSs were also located along the same line. In [13], it was further concluded that the interlink correlation can get high values even with large spatial separation of BSs in situations where the BSs are not located on the same line seen from the MS. The analysis revealed that the correlation resulted from the symmetry of the propagation environment and from the antenna array properties and orientations.

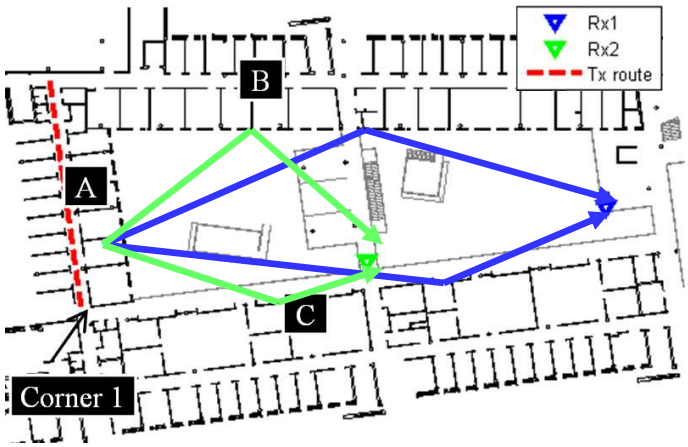

Figure 9.2. Propagation mechanisms in a scenario where the TX was moving along an office corridor acting as a MS and two RXs were located in a hall emulating BSs.

9.2 Correlated shadow fading

Correlated shadow fading stands for a situation where multiple links encounter degradation in power level due to a shadowing object simultaneously. Two typical cases that are subject to correlated shadow fading are sketched in Figure 9.3. In Figure 9.3(a), links MS – BS1 and MS – BS2 encounter correlated shadow fading since the two BSs are located relatively close to each other, and hence the shadowing object in front of the MS degrades the power in both links due to the shadowing of the LOS component. Naturally, if the shadowing object is relatively large, or it is located very close to the MS, even if the BSs would be separated by some distance the links might encounter correlated shadow fading. Figure 9.3(b), on the other hand, shows an example of a situation where the MS is behind a corner and the only possible signal direction towards both BSs goes round the corner. In this case, if a shadowing object happens to block this one and only possible signal path, both links encounter shadow fading simultaneously even though the two BSs would be separated by a considerable distance.

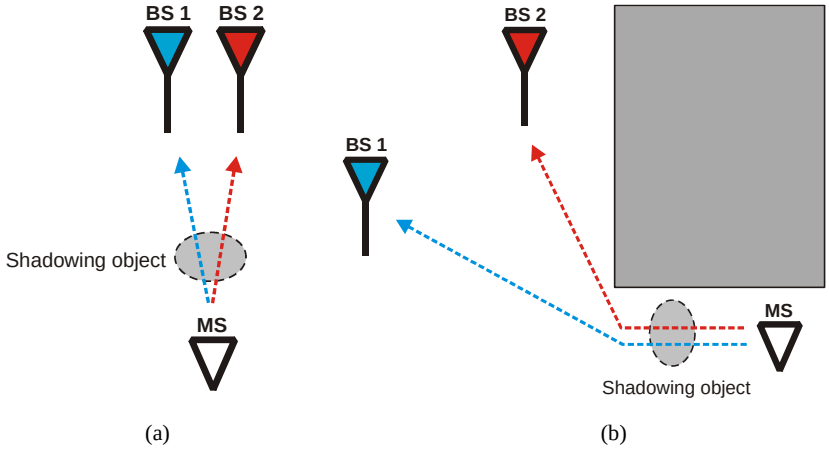

Figure 9.3. Examples of situations where correlated shadow fading is likely to occur. (a) If two BSs are located relatively close to or behind each other, a shadowing object in front of the MS can cause correlated shadow fading. (b) If only one dominant signal path connects the MS to both BSs, a shadowing object blocking this path causes fading in both links.

Correlated shadow fading is an important characteristic in multi-link scenarios, since it can deteriorate the performance of radio communication systems utilizing separated links. For instance, the sum rate capacity and reliability of a multi-user MIMO system can be degraded, or the expected coverage enhancement of a relay scheme may be reduced if alternative links are simultaneously shadowed. Thus, knowledge on the physical phenomena that cause correlated shadowing in multi-link scenarios is essential for the development of such systems.

The correlated shadow fading was studied in [12] based on a dynamic dual-link channel measurement in an indoor scenario shown in Figure 9.4. The measurement system comprised one TX moving along a continuous route and two RXs located at fixed positions. In this case, the different links showed remarkable similarities in terms of shadow fading, even though the two RXs were located on completely different sides of the measurement venue. As seen in Figure 9.4, concrete pillars were located at constant intervals on the balcony along which the TX was moving.

In order to investigate the reason for the correlated shadow fading in this scenario, the different propagation phenomena were identified with the MBRT, as described in Chapter 3. With the used method, it is possible to distinguish the different propagation mechanisms and, e.g., to investigate the power carried by each individual propagation mechanism as a function of the measurement location. It was found out that the concrete pillars next to the TX route caused the shadow fading in both links. In link TX – RX 1,

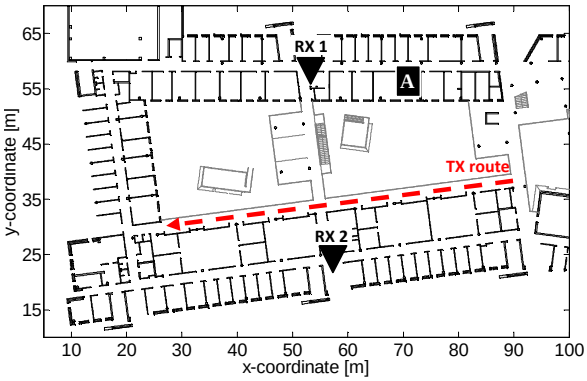

(a)

(b)

Figure 9.4. (a) Floorplan of the measurement venue with the TX route (dashed red line) and the RX positions (black triangles). (b) Measurement environment seen from the third floor. The TX route is shown with the dashed red line. The yellow arrows point to the pillars.

the direct path, i.e. the obstructed LOS component, carried a significant part of the energy, and was deeply shadowed whenever the TX was located behind a pillar, as shown in Figure 9.5(a). In link TX – RX 2, waves reflecting from wall A (see Figure 9.4(a)) encountered deep shadowing also by the pillars, as shown in Figure 9.5(b).

The normalized total received power after removing the effects of path loss and small scale fading is shown for the links TX – RX1 and TX – RX2 in Figure 9.5(c). First, the effect of path loss was removed by applying simple linear fitting to different parts of the received power along the measurement route and by subtracting the trend from the result.

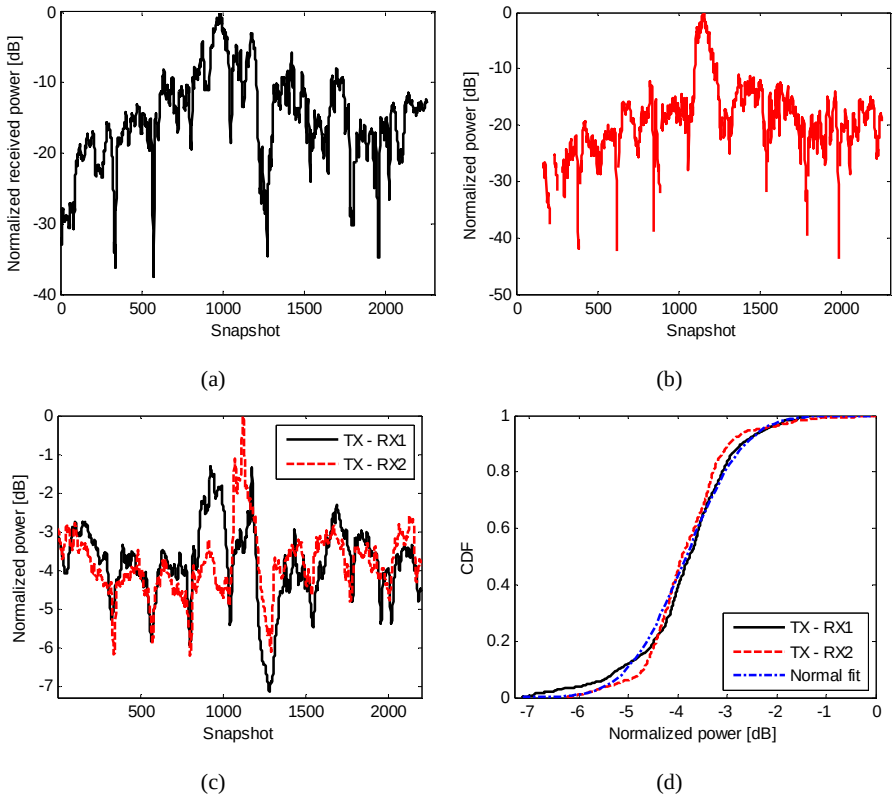

Figure 9.5. Normalized power of (a) the obstructed LOS component in the case of TX – RX1 link and (b) the signal components reflected from wall A in the case of TX – RX2 link. (c) Normalized total received power after removing the effects of path loss and small scale fading. (d) CDFs of the same data and a fit to a log-normal distribution.

After that, the effect of small scale fading was removed by using sliding window averaging with a window size of 30 snapshots[6]. Whenever the TX was behind a pillar, approximately 1.5 – 2.5 dB fading in the received power occurred simultaneously in both links, as seen by the dips in the normalized received power in Figure 9.5 (c). It is important to notice that Figure 9.5 (a) and Figure 9.5 (b) represent the powers of the individual propagation mechanisms that encountered deep shadow fading due to the pillars, whereas Figure 9.5 (c) shows the effects of the pillars on the total received power. The fading behavior of the total power fitted well to a log-normal distribution with the mean and standard deviation of 3.83 dB and 0.94 dB, respectively, as can be seen in

[6]The averaging window size needs to be large enough to remove the effect of fast fading, but on the other hand, small enough not to remove the effects of shadow fading. Hence, 30 snapshots was considered as a reasonable compromise.

Figure 9.5(d). The similarity between the fading of the two links is remarkable considering the very large terminal separation (approximately 40 meters) on the RX side.

The main conclusion of [12] is that links between the mobile terminal and different access points can be simultaneously shadowed even if the access points are separated by a large distance if 1) a significant proportion of energy propagates along the same path in the different links, and 2) if this common path is shadowed. The common path can be expected to occur e.g. in cases where a dominant scattering object is common for the different links, or when the mobile station is located in a corridor leading to a waveguiding propagation.

9.3 Common scatterers

One of the physical phenomena increasing the link correlation is scatterers that are common for two or more links. One should note that the geometry conditions described in Section 9.1 naturally affect the probability to observe common scatterers, and in that sense, the common scatterers also stem from the geometry of the environment to some extent. However, common scatterers can occur also regardless of the terminal geometries for instance in corridor scenarios. Common scatterers are especially harmful for multi-user radio systems that depend on the spatial characteristics of the channel, since underestimating the significance of common scatterers in simulations would result in overestimating the system performance. For instance, mitigation of the interference from other users by spatial filtering might become difficult, or the desired performance improvement of a relay scheme be deteriorated, if different links are correlated due to similar scatterers [17], [108].

In order to quantify how large amount of energy propagates via the same scatterers in different links, a measure called *the significance of common scatterers* is introduced as follows [11]. In a dual-link case, the significance of the *n*-th common scatterer is denoted as a function of a measurement snapshot *ss* by

$$S^{n}_{\mathrm{common}}(ss) = \sqrt{s^{(1),n}_{\mathrm{common}}(ss) \cdot s^{(2),n}_{\mathrm{common}}(ss)}, \tag{9.1}$$

where $s^{(i),n}_{\mathrm{common}}(ss)$ is the significance of the *n*-th common scatterer, which is defined by the power of common scatterers $P^{(i)}_{\mathrm{common}}(ss)$ with respect to the total power of the *i*-th link $P^{(i)}_{\mathrm{tot}}(ss)$ as

$$s_{\text{common}}^{(i),n}(ss) = \frac{P_{\text{common}}^{(i),n}(ss)}{P_{\text{tot}}^{(i)}(ss)}\ , \tag{9.2}$$

where $i = 1, 2$. If the total number of scatterers that are common for the different links is denoted by $N(ss)$, the total significance of the common scatterers can be expressed by the sum of the significances of the individual common scatterers $S_{\text{common}}^{n}(ss)$ by

$$S_{\text{common}}\ (ss) = \sum_{n=1}^{N(ss)} S_{\text{common}}^{n}(ss). \tag{9.3}$$

The total significance of the common scatterers $S_{\text{common}}(ss)$ gets values between 0 and 1, where 0 means that the different links have no common scatterers and 1 indicates that all scatterers are common for the two links.

When common scatterers are investigated in channel measurements, in situations where the scatterer has a relatively large physical size (e.g. a wall of a building), it is not always meaningful to consider the whole scatterer as common for different links. In such cases, even if the scattering source is the same physical object, the scattering points for different links might be separated by a large distance, and thereby the MS or BS equipped with antenna arrays could be able to resolve the scattering points in the angular domain. In order to exclude such scatterers from common scatterers, it is necessary to establish geometry-dependent conditions to define a common scatterer in a meaningful manner. The conditions for the common scatterer are derived based on 1) the distance between the scatterers of different links *d*, and 2) the angular separation of the scatterers seen from the MS φ, as shown in Figure 9.6. Furthermore, since several MPCs might originate from the same physical scatterer, the coordinates for the center point of the scatterer (or cluster center) are calculated as a power-weighted mean over the coordinates of the individual MPCs belonging to the same cluster. This is necessary, since a single scattering point is needed for each link and for each snapshot in order to be able to calculate unique *d* and φ for the scatterer in question.

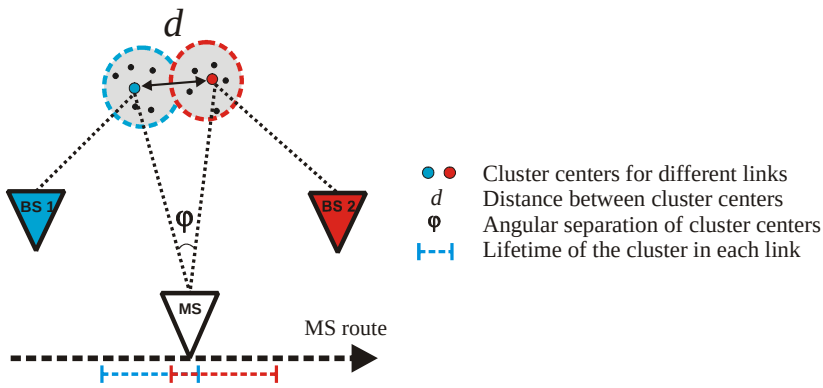

Figure 9.6. The definition for a common scatterer. A scatterer is considered common if the angular separation φ and the distance d between the cluster centers of the different links are smaller than the resolution of the envisioned communication system.

The significance of common scatterers was studied in the corridor of the Department of Radio Science and Engineering, in Aalto University School of Science and Technology. The floor plan of the environment is shown in Figure 9.7. In this case, the MS was moving along a corridor towards a T-junction, and the two BSs were located on opposite sides of the perpendicular corridor seen from the MS. Hence, the investigated scenario represents a realistic WLAN network deployment. Throughout the route, there were NLOS conditions in both links. The significance of common scatterers was studied also in other environments in [11]; however, here results only the most representative and interesting scenario are discussed in detail.

In order to investigate the significance of common scatterers in the scenario under consideration, the first scattering point seen from the MS on wall A was calculated and used to check the conditions for the common scatterer. In addition, the points on wall B where the signal either propagates through the wall (MS – BS1 link) or reflects from it (MS – BS2 link) were identified. In this scenario, other scatterers did not fulfill the criteria of the common scatterer. Considering resolution limitations in practical portable devices, d = 5 m and φ = 45 degrees were chosen as sensible threshold values for the criteria of what is considered as common scatterers.

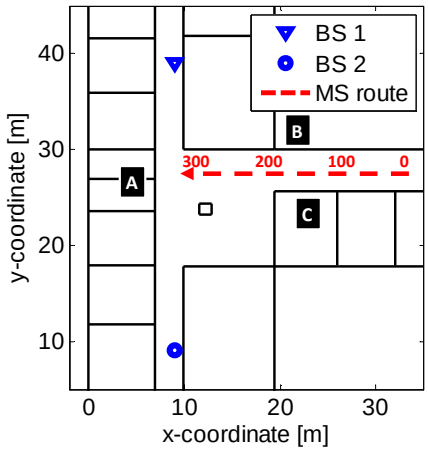

Figure 9.7. The floor plan of the measurement environment.

Figure 9.8 (a) and (b) show the d and φ separately for the scatterers A and B as a function of the MS location. In the case of wall A, the angular separation is around 10 degrees in the beginning of the route, but after snapshot 200 it starts to increase; in this location the MS passes the corner of wall C and the scattering points in the MS – BS2 link start to move further south. The threshold value is exceeded approximately at snapshot 220. In the case of wall B, the angular separation of the scattering points varies more rapidly than in the case of wall A. Furthermore, wall B is an active common scatterer only in parts of the route. The distance between the scattering points on both walls A and B follow the same trends as the angular separation. Also in this case, the threshold value is exceeded in the end of the MS route.

Figure 9.8 (c) shows S_{common} separately for scatterers A (blue curve) and B (red curve) and the total S_{common} (black curve). It is seen that the waveguiding along the corridor (A) is a significant propagation mechanism in both links, hence constituting a significant common cluster. Also wall B forms a common cluster in parts of the route. The total S_{common} varies between 40 % and 95 %, but goes rapidly to zero around snapshot 220 due to the fact that the threshold values for the conditions of common scatterer are exceeded in that location.

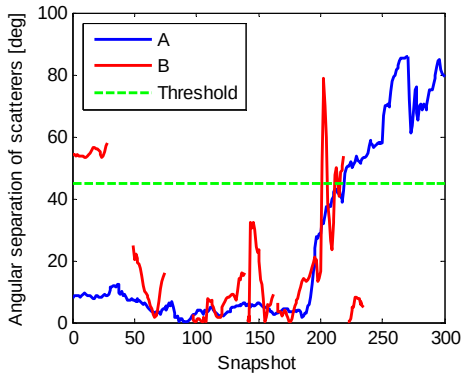

(a)

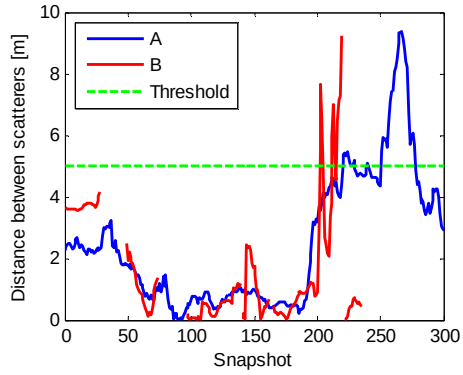

(b)

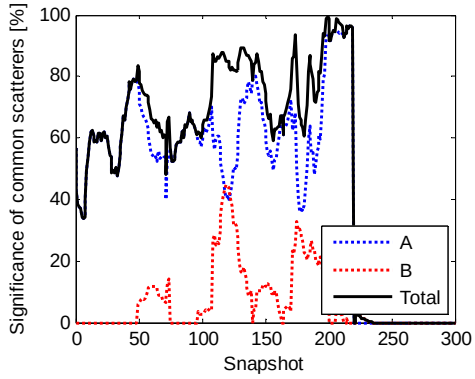

(c)

Figure 9.8. (a) The angular separation of the scattering points belonging to the different links seen from the MS. (b) The distance between the scattering points of different links. (c) The significance of common scatterers as a function of the MS location in snapshots.

10 Multi-link channel modeling principles

The experimental findings made above in Chapter 9 and in [108] – [109] indicate a true need for multi-link MIMO channel models being able to reflect inter-link correlation properties in a realistic manner. Furthermore, since the trend in novel radio communication systems is going more and more towards utilizing links between multiple nodes of the network in their operation, the need for realistic multi-link channels model increases accordingly. However, previous works on multi-link MIMO channel models are very limited. To the author's best knowledge, prior to the modeling approach presented below in this chapter, the only contribution to multi-link MIMO channel modeling with experimental support in the open literature is the analytical dual-link model presented in [15]; no contributions on multi-link GSCMs are available in the open literature.

An idea of a method to extend GSCMs to support multi-link simulations was first introduced in [11]. The idea is based on sharing part of the clusters between different links. The idea was further refined and a multi-link GSCM was implemented based on the concept of common clusters in [17]. In addition, the multi-link modeling concept based on the common clusters has been also applied to the COST 2100 channel model, as described in [16].

10.1 Concept of common clusters

A common cluster (CC) is a cluster that contributes to the channel between multiple MS – BS links at the same time, as shown in Figure 10.1. As discussed in Chapter 9, common scatterers[7] are one of the phenomena that are assumed to affect the inter-link correlation, and thus it is important to include them in the GSMCs. CCs are a convenient way of extending the GSCM to multi-link scenarios also because they can be used to some extent to describe the other important physical phenomena that cause inter-link correlation (i.e. geometry of the environment and correlated shadow fading, see Chapter 9), and because GSCMs inherently support the inclusion of common clusters.

Since the amount of power carried by the common clusters can be set to a desired value, it is possible to control the inter-link correlation between different links; the larger is the amount of power that is propagating via the common clusters, the stronger the correlation

[7] In this thesis, the term *scatterer* stands for a physical object that can be identified in the measurement, whereas *cluster* is used in the GSCMs to model a scatterer.

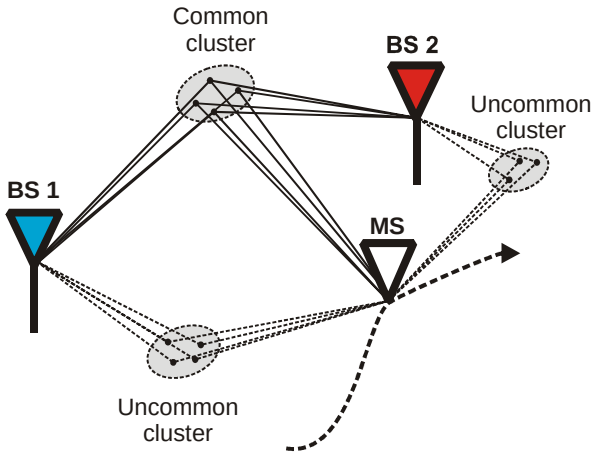

Figure 10.1. Example of a common cluster in a scenario with one MS and two BSs. The correlation between different links can be controlled by changing the amount of power that propagates through the common cluster.

between the different links. Since the properties of the individual links should not be changed even when the GSCMs are extended to multi-link scenarios, the intra-link correlation, i.e. the correlation between antenna elements in a MIMO link, should as before be controlled by the cluster distributions of the simulation environment.

In order to implement and validate a high-quality multi-link channel model based on CCs, clusters and the corresponding VRs need to be generated realistically, i.e., in the same way as observed in measurements. To this end, additional parameters describing how similarly different BSs and/or MSs see the clusters, are introduced, including:

- Probability of common clusters
- Significance of common clusters
- Lifetime of common clusters

The probability of common clusters p_{common} is determined by the number of clusters that are simultaneously seen by the different BSs relative to the total number of clusters: p_{common} is simply obtained as the ratio of number of common clusters N_{common} and the total number of clusters N_{tot}:

$$p_{\mathrm{common}} = \frac{N_{\mathrm{common}}}{N_{\mathrm{tot}}}. \tag{10.1}$$

The common cluster power ratio S_{common} is denoted as the ratio of the power in the common clusters P_{common} and the total power P_{tot} as

$$S_{\text{common}} = \frac{P_{\text{common}}}{P_{\text{tot}}}. \tag{10.2}$$

The lifetime of the common cluster is defined for the individual links in the same way as in the single-link case according to the VRs. However, as the common clusters are generally not alive during exactly the same period of time in the different links, the lifetime of the common clusters needs to be determined separately for each link. It should be noted that the common cluster VRs for the different links can have different radii, and furthermore the center points of the VRs may be in different locations. Hence, a natural approach is to consider the lifetime of the common cluster as the time when the cluster is simultaneously active for the different links.

10.2 Multi-link extension of the COST 2100 channel model

The rather complex structure of the COST 2100 channel model requires some modifications in order to facilitate the extension of the model to support multi-link simulations. In particular, the way to assign clusters and the corresponding VRs among the different links needs a special care. This section highlights the basic features of the implementation of the COST 2100 multi-link extension. Since the multi-link extension of the new COST 2100 channel model is fully based on the principles presented in this section, only the COST 2100 channel model is considered below when describing the implementation principles. One should note, however, that even though the COST 2100 channel model is emphasized in this section, the presented modeling concepts are fully applicable to other GSCMs (such as the WINNER model), as well.

The implementation of the COST 2100 multi-link channel model has been accomplished in close cooperation between research groups from Aalto University, Finland, Lund University, Sweden, and Universite Catholique de Louvain, Belgium within the frameworks of the WILATI+ project and the COST 2100 action. The content of this section is mainly based on [16].

10.2.1 Implementation principles

Intuitively, the structure of the COST 2100 channel model supports simulating multi-link scenarios simply by dropping multiple BSs or MSs into the simulation environment.

However, the structure of the whole COST 2100 channel model relies on the concept of the VRs, and how to assign the VRs for the different BSs and MSs in multi-link scenarios is yet to be thoroughly investigated. In the COST 273 channel model, the clusters and the corresponding VRs were generated independently for each BS, meaning that there was no way to control the correlation between different links. Furthermore, each cluster was assigned only one VR, which naturally prevented multiple MSs (that are separated by a large distance and thus are not located inside the same VR) seeing the same cluster simultaneously. Since common scatterers can carry significant proportions of energy in realistic environments, a key part in developing the multi-link extension to the COST 2100 channel model is to realistically generate the clusters that are common among multiple BSs and/or MSs.

Figure 10.2 (a) and (b) show schematics of how clusters and VRs are generated in the COST 2100 channel model in the cases of multi-MS and multi-BS simulations. In a multi-MS simulation, each cluster needs to be assigned multiple VRs so that different MSs are able to see the same cluster simultaneously even if the MSs would be separated by a large distance. Hence, MS-common clusters are implemented by VR groups, i.e. by allowing each cluster to be connected with multiple VRs. In the example presented in Figure 10.2 (a), Cluster 1 has two VRs and the two MSs are located inside them. In a multi-BS simulation, a part of the clusters are forced to be common among different BSs. Figure 10.2 (b) shows an example of a case where Cluster 1 is common among BS 1 and BS 2; hence, MS 1 is connected to both BSs through cluster 1. A scenario with both multiple BSs and multiple MSs can be naturally generated by combining these two concepts.

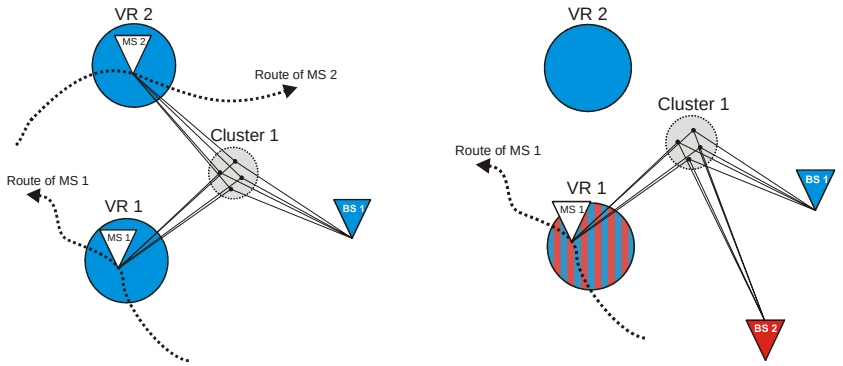

Figure 10.2. (a) In multi-MS simulations, several VRs are assigned for a single cluster to allow MSs that are separated by a large distance to see the same cluster. (b) In multi-BS simulation, clusters can be related to multiple BSs simultaneously.

10.2.2 Visibility region assignment table

When generating clusters and VRs in the COST 2100 multi-link channel model a *VR assignment table*, which specifies to which BSs and through which VRs each cluster is visible, needs to be generated. The VR assignment table is generated in the following way. First, the total number of VRs is determined, after which each VR is related to certain BSs. As a result, a part of the VRs will be common among multiple BSs. After this, the VRs are grouped so that the same cluster is assigned for them. It should be noted that a cluster may be related to multiple VRs, whereas each VR is strictly related to only one cluster. In the case of the scenario presented in Figure 10.2, Cluster 1 is visible to BS 1 through VR 1 and VR 2, and to BS 2 through VR 1, as shown in Table 10.1.

The VR assignment table needs to be large enough to specify the link connections for all the VRs in the environment. It has to also keep single-link consistency, such as the VR density and the cluster selection factor K_{sel}, for each BS. The only additional parameters that are required to characterize the multi-link extension are ratio of common clusters to the total number of clusters in the environment, and the average number of VRs in one VR group for a cluster.

Table 10.1. A Table for the assignment of clusters to BSs and VRs in the case of the scenario presented in Figure 10.3.

	VR 1	**VR 2**
BS 1	Cluster 1	Cluster 1
BS 2	Cluster 1	-

11 Effect of common clusters on system performance metrics

This chapter is dedicated to investigating the ability of a multi-link GSCM based on CCs to simulate multi-link scenarios. At first, a simple multi-link GSCM is implemented based on the concept of common clusters. The developed GSCM is then used to study the effect of the common clusters on channel characteristics and system performance from two perspectives: first, it is shown that common clusters are a suitable way of adjusting the correlation between different links, and, second, the effect of the common clusters on sum rate dual-link channel capacity is investigated. In the last part of the chapter, common clusters are analyzed based on measured dual-link MIMO data. It is also shown that the developed multi-link GSCM is able to accurately predict the channel behavior in comparison with the measurement data. Even though the GSCM implemented in this chapter is a rather simple one, the results of this chapter are fully applicable to more sophisticated GSCM implementations as well.

This chapter has been mainly written based on publication [17].

11.1 Simple multi-link GSCM

The model implemented in this section is based on clusters that emulate physical scattering objects of real environments, in the same way as in conventional GSCMs, and the MIMO channel matrices are constructed as usual based on the propagation path parameters. Regarding the single-link properties, the implemented GSCM includes some simplifications with respect to the more comprehensive GSMCs, such as the COST 2100 channel model; in particular, only single-bounce clusters are considered, and the concept of visibility regions is not included in the model meaning that the death/birth properties of clusters as a function of location is not regarded. Furthermore, the full model parameterization (including parameters such as angular and delay spreads, cluster shadow fading, etc.) based on measurement data has not been considered. These simplifications were made to the implementation in order to be able to fully focus on the performance of the multi-link extension of the GSCMs, in other words, on the effects caused by the common clusters, which would have been hard by using e.g. the full implementation of the COST 2100 multi-link channel model. Furthermore, since the omitted modeling concepts are targeted to model completely different aspects of the channels than common clusters, omitting them does not deteriorate the quality of the results of this chapter.

In the developed simple multi-link GSCM, clusters are generated so that each link is assigned a set of *uncommon clusters* (UCCs) and a certain number of *common clusters* (CCs). The UCCs are generated on the simulation map independently for each link and they contribute only to the impulse response of the designated link, whereas CCs are shared by the different links and contribute to both impulse responses, see Figure 10.1. In order to control the correlation between different links, the amount of power that propagates through the CCs is set to a desired value by the following procedure. First, the propagation path parameters, including the DoD and DoA, delay, and complex amplitude, are calculated for each MPC according to the geometrical locations of the antennas and clusters. Then, the power carried by the UCCs is scaled with a factor L so that the condition

$$S_{\text{common}} = \frac{P_{\text{CC}}}{L \cdot P_{\text{UCC}} + P_{\text{CC}}} \tag{11.1}$$

is satisfied. In (11.1) , S_{common} defines the ratio between powers carried by the CCs and UCCs; P_{CC} and P_{UCC} are the sum of powers carried by all the CCs and UCCs, respectively.

Once the propagation path parameters with the desired S_{common} have been obtained, the MIMO channel matrices are calculated for each link in the same way as for a conventional GSCM as

$$\mathbf{H} = \sum_{p=1}^{P} \alpha_p \, \boldsymbol{a}_p^{\text{RX}} (\boldsymbol{a}_p^{\text{TX}})^T e^{j(2\pi f \tau_p + \xi(p))} \in \mathbb{C}^{N_r \times N_t}, \tag{11.2}$$

where P is the number of MPCs, α_p is the amplitude of the p-th MPC, f is the used radio frequency, τ_p is the propagation delay of the p-th MPC, and $(\cdot)^T$ denotes the matrix transpose operation. Furthermore, $\boldsymbol{a}_p^{\text{TX}}$ and $\boldsymbol{a}_p^{\text{RX}}$ are the array response vectors calculated at the TX or RX as

$$\boldsymbol{a}_p^{\text{TX,RX}} = \left[\exp\left(\mathrm{j}k\langle \boldsymbol{r}_1^{\text{TX,RX}} \boldsymbol{u}_p \rangle\right) \cdots \exp\left(\mathrm{j}k\langle \boldsymbol{r}_N^{\text{TX,RX}} \boldsymbol{u}_p \rangle\right)\right] \tag{11.3}$$

where $k = \frac{2\pi}{\lambda}$ is the wave number, $\boldsymbol{u}_p$ is the unit directional vector consisting of the DoD or DoA of the p-th MPC, and $\boldsymbol{r}_n$ is the position vector of the n-th antenna element in the array. The term $\langle \boldsymbol{r}_N \boldsymbol{u}_p \rangle$ represents the inner product between vectors $\boldsymbol{r}_N$ and $\boldsymbol{u}_p$. Finally, a random phase $\xi(p)$ is added to each MPC in order to increase the number of independent realizations of the channel matrices [110].

11.2 Performance metrics

11.2.1 Inter-link correlation

The inter-link correlation on the MS side was evaluated by calculating the correlation matrix collinearity (*CMC*, or "collinearity") as [111].

$$CMC = \frac{\left|\mathrm{tr}\left\{\mathbf{R}_1\mathbf{R}_2^{\mathrm{H}}\right\}\right|}{\|\mathbf{R}_1\|_{\mathrm{F}}\|\mathbf{R}_2\|_{\mathrm{F}}}, \tag{11.4}$$

where $\mathbf{R}_i$ is the correlation matrix of the *i*-th link calculated as

$$\mathbf{R}_i = \sum_{s=1}^{N_s}\left(\mathbf{H}_i(s)\right)^{\mathrm{H}}\mathbf{H}_i(s). \tag{11.5}$$

In Equations (11.4) and (11.5), $(\cdot)^{\mathrm{H}}$ is the complex transpose of a matrix; N_s is the number of independent channel realizations; N_t is the number of transmit antennas; and $\|\cdot\|_{\mathrm{F}}$ denotes the Frobenius norm.

The *CMC* describes how similar the subspaces of the correlation matrices of the different links are, ranging between zero (matrices are orthogonal to each other) and one (matrices are similar).

11.2.2 Sum rate dual-link capacity

The capacity values were calculated in the following way. First, the received power for the *i*-th link P_i was calculated as

$$P_i = \frac{1}{N_s \cdot N_r \cdot N_t}\sum_{s=1}^{N_s}\|\mathbf{H}_i(s)\|_{\mathrm{F}}^2, \tag{11.6}$$

where N_s is the number of independent channel realizations; N_r is the number of receive antennas; N_t is the number of transmit antennas; $\mathbf{H}_i$ is the channel matrix of the *i*-th link; and $\|\cdot\|_{\mathrm{F}}$ denotes the Frobenius norm. In order to calculate the capacity, the channel matrices were normalized as

$$\widehat{\mathbf{H}}_i(s) = \frac{\mathbf{H}_i(s)}{\sqrt{P_i}}. \tag{11.7}$$

In the dual-link case, the received signal can be written as [112]

$$\mathbf{y} = \sqrt{\rho}\widehat{\mathbf{H}}_{\text{des}}\mathbf{x}_{\text{des}} + \sqrt{\eta}\widehat{\mathbf{H}}_{\text{int}}\mathbf{x}_{\text{int}} + \mathbf{n}, \tag{11.8}$$

where $\widehat{\mathbf{H}}_{\text{des}}$ and $\widehat{\mathbf{H}}_{\text{int}}$ are the normalized channel matrices of the desired and interfering link, and $\mathbf{x}_{\text{des}}$ and $\mathbf{x}_{\text{int}}$ are the transmitted signal vectors, respectively, and $\mathbf{n}\sim\mathcal{N}(0,\mathbf{I})$ is an uncorrelated complex Gaussian noise vector. Since the channel matrices and the noise variance are normalized, ρ and η represent the signal-to-noise ratio (SNR) and interference-to-noise ratio (INR). The ergodic channel capacity values were calculated using instantaneous channel realizations as [112]

$$C = E\left\{\log_2\left[\det\left(\mathbf{I}_{N_r} + \frac{\rho}{N_t}\widehat{\mathbf{H}}_{\text{des}}^{\text{T}}\left(\widehat{\mathbf{H}}_{\text{des}}^{\text{T}}\right)^{\text{H}}\mathbf{R}_{\text{int}}^{-1}\right)\right]\right\}, \tag{11.9}$$

where, again, sub-indices "des" and "int" stand for the "desired" and "interfering" links. In this case, it is assumed that there is no channel state information at the transmitter (i.e. the transmit signal covariance becomes an identity matrix) and a full knowledge of the channel at the receiver.

Next, the capacity is studied in two different cases, i.e. in the single-link case (i.e. without interference) and in the dual-link case (i.e. with interference). When calculating the capacity in the single-link case, i.e. $E\{C(\widehat{\mathbf{H}}_{\text{des}})\}$, the covariance matrix $\mathbf{R}_{\text{int}}$ in Equation (11.9) was set to

$$\mathbf{R}_{\text{int}} = \mathbf{I}_{N_r} \tag{11.10}$$

and when calculating the capacity in the dual-link case, i.e. $E\{C(\widehat{\mathbf{H}}_{\text{des}}, \widehat{\mathbf{H}}_{\text{int}})\}$, the covariance matrix was set to

$$\mathbf{R}_{\text{int}} = \eta\widehat{\mathbf{H}}_{\text{int}}^{\text{T}}\left(\widehat{\mathbf{H}}_{\text{int}}^{\text{T}}\right)^{\text{H}} + \mathbf{I}_{N_r}. \tag{11.11}$$

In the following, the analyses focus on the relative sum rate capacity (SRC, or "capacity"), which is denoted by the ratio between the sum rate dual-link capacity $E\{C(\widehat{\mathbf{H}}_1, \widehat{\mathbf{H}}_2)\} + E\{C(\widehat{\mathbf{H}}_2, \widehat{\mathbf{H}}_1)\}$ and the sum rate single-link capacity $E\{C(\widehat{\mathbf{H}}_1)\} + E\{C(\widehat{\mathbf{H}}_2)\}$:

$$SRC = \frac{E\{C(\hat{\mathbf{H}}_1, \hat{\mathbf{H}}_2)\} + E\{C(\hat{\mathbf{H}}_2, \hat{\mathbf{H}}_1)\}}{E\{C(\hat{\mathbf{H}}_1)\} + E\{C(\hat{\mathbf{H}}_2)\}}. \quad (11.12)$$

In (11.12), sub-indices "1" and "2" stand for links 1 and 2, meaning that first link 1 was considered as the desired link and link 2 as the interfering link, and then vice versa. The *SRC* is a measure to quantify the effect seen on the sum rate capacity of imperfect spatial filtering by zero-forcing compared to a case where the interference is perfectly cancelled.

11.3 Simulation studies

Figure 11.1 shows a flow chart of the procedure of how the effect of common clusters on *CMC* and *SRC* is evaluated. In Figure 11.1, the corresponding procedure for the measurement data is also shown; the correlation and capacity are studied based on measurement data in Section 0.

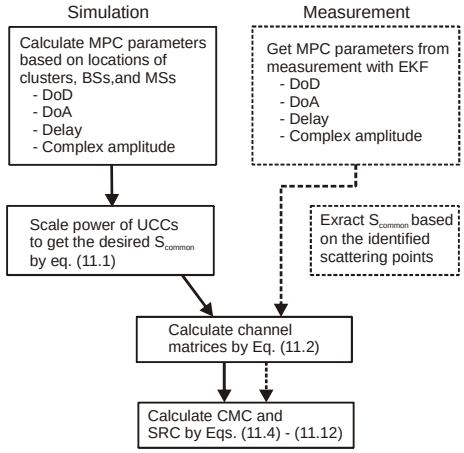

Figure 11.1. Flow chart of the method to investigate the effect of common clusters on system performance based on simulations and measurements.

The effect of the common clusters on inter-link correlation and sum rate dual-link capacity was investigated by computer simulations in three different scenarios. In the first scenario, the locations of the clusters were changed in a controlled manner in order to study the relationships between S_{common}, *CMC* and *SRC* and the influence of the environment through a simple example. In the simulations of these *controlled channels* the environment consisted of one uncommon cluster (per link) and one common cluster (shared by the different links). Then, the simulation studies were continued by placing the clusters in random locations. First, the *random channels* consisted of one UCC and one

CC, and, after that, of five UCCs and one CC, all being randomly positioned in the simulation area of 40 m × 40 m. In each of the three scenarios, one MS and two BSs were located at fixed positions. The clusters consisted of five MPCs placed randomly within a diameter of one meter around the center point of the cluster. Furthermore, a 4-element x-oriented uniform linear antenna array (ULA) was used at the MS and BSs in each case. The ρ and η were both fixed to 10 dB in all the simulations. In the following, the presented *CMC* and *SRC* values are the average values over 100 independent channel realizations. Table 11.1 summarizes the three different simulation scenarios.

Table 11.1. Summary of the simulation scenarios.

Simulation scenario	**Controlled**	**Random #1**	**Random #2**
# BSs/MSs	2/1	2/1	2/1
# uncommon clusters (per link)	1	1	5
# common clusters	1	1	1
# MPCs within cluster	5	5	5
SNR/INR [dB]	10/10	10/10	10/10
Antenna array of BS and MS	4-element x-oriented ULA	4-element x-oriented ULA	4-element x-oriented ULA

As a general conclusion of the simulation studies, it can be said that S_{common} has a significant effect on both the inter-link correlation and MIMO channel capacity; as S_{common} increases, the *CMC* increases and *SRC* decreases. This indicates the ability of the multi-link GSCM based on common clusters to manipulate the correlation between different links. It also shows that it is important not to neglect the effect of common clusters.

Next, the findings from the simulation studies are discussed in detail separately for the controlled and random scenarios.

11.3.1 Controlled channels

In the controlled scenario, clusters were located so that the CC and the UCC2 for the link MS – BS2 were at fixed positions whereas the UCC1 for the link MS – BS1 was moved on a circle with 45 degree steps around the MS, as shown in Figure 11.2. The simulations

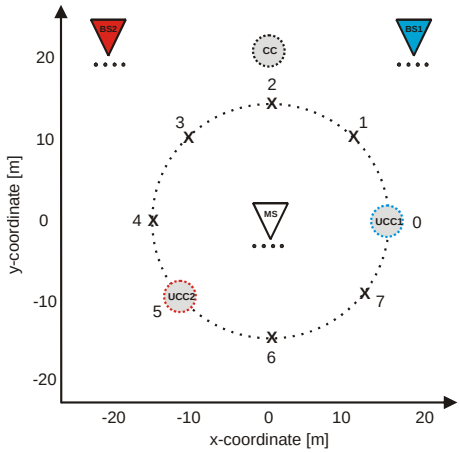

Figure 11.2. Environment in the simulations of the controlled environment. The CC and UCC2 were at fixed positions, whereas the UCC1 was moved from locations 0 to 7.

with the different locations of UCC1 are marked with numbers 0 – 7 in Figure 11.2. At each location of the UCC1, the *CMC* and *SRC* were simulated with S_{common} ranging between 0 % and 100 %.

Figure 11.3 shows the collinearity and capacity as a function of S_{common} for the different locations of the UCC1. It is seen that the capacity is very high at low values of S_{common} in most of the locations of the UCC1, and gradually decreases to approximately 10 % of its original value as S_{common} approaches 100 %. The collinearity behaves in the opposite way, i.e. whenever the capacity is high, the collinearity is low, and vice versa. However, at UCC1 locations 3 and 5 the capacity is low, and the collinearity almost one, with all values of S_{common}. At UCC1 location 5, both UCCs are located exactly at the same position, meaning that the situation is equivalent to the case where all the clusters are common among the different links. At UCC1 location 3, there is a high correlation between the different links since the MS cannot distinguish the waves coming from locations 3 and 5 due to its antenna array orientation.

11.3.2 Random channels

As shown above, the locations of the clusters may have a significant impact on the correlation and capacity values observed at different values of S_{common}. In particular, it can be observed that with some combinations of the cluster locations collinearity is high and capacity is low even without the CC. In order to investigate the relationships between S_{common}, collinearity, capacity, and cluster locations in a statistical manner, the simulation studies were continued by placing the clusters in random locations.

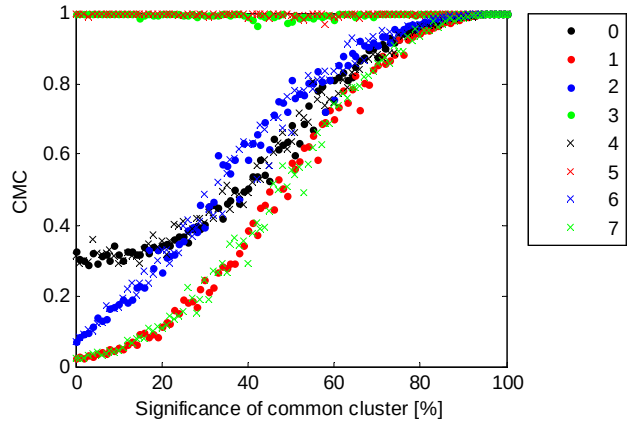

(a)

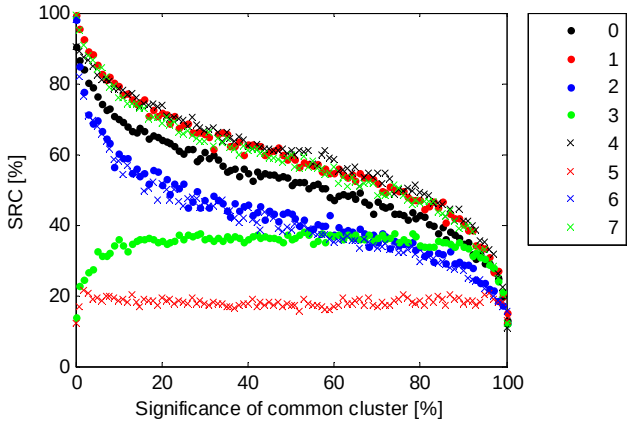

(b)

Figure 11.3. (a) The correlation matrix collinearity (*CMC*), and (b) the relative sum rate capacity (*SRC*) as a function of the significance of common cluster. The legends show the correspondence between the curves and the locations of UCC1.

The CDFs of the collinearity and capacity are shown for the first random scenario (one UCC, one CC) for the S_{common} values of 0, 1, 10, 50, 90, 99, and 100 % in Figures 11.4 (a) and (b). For each value of S_{common}, the CDF curve includes the values of the collinearity and capacity from 1000 random channels. With the S_{common} values of 0, 1, and 10 %, the matrix collinearity behaves quite similarly and is less than 0.2 in approximately 60 % of the cases. Even if for the most of the time the collinearity is low and capacity high with low values of S_{common}, also highly correlated channels are observed: the collinearity is at least 0.8 in about 15 % of the cases even without the CC.

With the S_{common} values of 0, 1, and 10 %, the capacity gets high values for the most of time, as could be expected. It was also found that capacity is more sensitive than the collinearity to the change of S_{common} in the range of 0 to 10 %: for instance, at the CDF level of 0.5, the capacity decreased by approximately 25 %-units when S_{common} increased from 0 to 10 %. This is an important observation in the sense that even if only a small amount of the power propagates through the common cluster, the impact on the system performance is significant compared to the case where the common cluster is not considered at all. In addition, it is an indication that the value for S_{common} needs to be set carefully, i.e. based on real measurement results, in the simulations.

When S_{common} is 50 %, both the collinearity and capacity are more or less evenly distributed between the minimum and maximum values. With the S_{common} values of 90, 99, and 100 %, we can see that the collinearity is very close to 1 the whole time. However, variations between the respective capacity curves are more clearly seen. The CDFs of the collinearity and capacity are shown for the second random scenario (5 UCCs, 1 CC) for the S_{common} values of 0, 1, 10, 50, 90, 99, and 100 % in Figures 11.5 (a) and (b). Again, the CDF curves include the values of the collinearity and capacity from 1000 random channels for each value of S_{common}.

In comparison with the first random scenario (1 UCC, 1 CC), the following observations can be made. First, with low values of S_{common} (0, 1, and 10 %), the collinearity is generally higher and therefore capacity lower; the same trends occur when S_{common} is 50 %. This can be explained so that as the number of clusters increases, it is harder for the antenna array at the MS to separate them, and hence, the correlation between links is likely to increase. Obviously, with larger antenna arrays, this effect would be less significant due to better capability of spatial filtering. With high values of S_{common} (90, 99, and 100 %), the curves are very similar to the first random scrnario, as could be expected, since anyway almost all the power propagates through the common cluster.

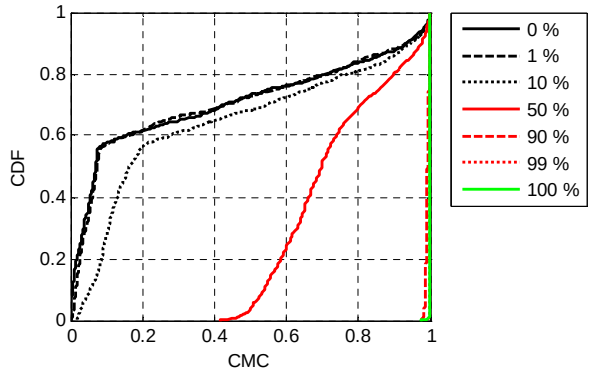

(a)

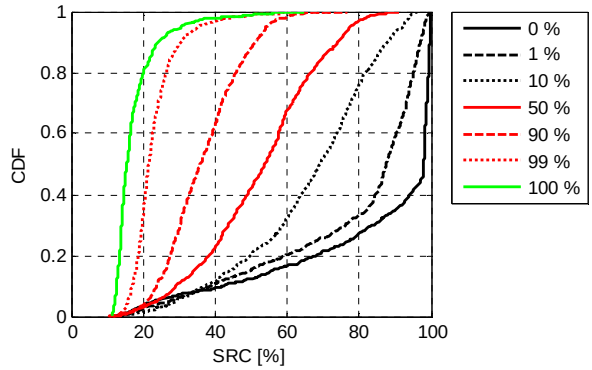

(b)

Figure 11.4. Effect of common cluster on collinearity and capacity simulated in the first random scenario (one uncommon cluster, one common cluster). CDFs of the (a) collinearity and (b) capacity. The CDFs are drawn from 1000 random combinations of cluster locations for each value of the S_{common}.

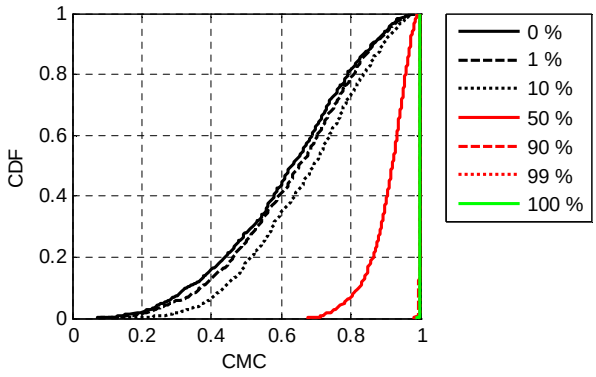

(a)

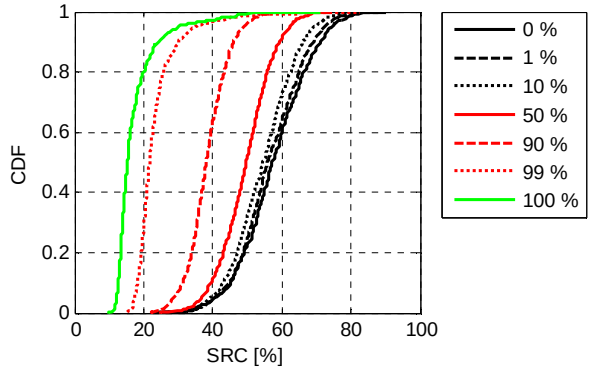

(b)

Figure 11.5. Effect of common cluster on collinearity and capacity simulated in the second random scenario (five uncommon clusters, one common cluster). CDFs of the (a) collinearity and (b) capacity. The CDFs are drawn from 1000 random combinations of cluster locations for each value of the S_{common}.

11.4 Effect of common clusters in measurements

The significance of common clusters was analyzed in an office corridor scenario in Section 9.2. The results of that section revealed that propagation along the corridor was a significant propagation mechanism in both links, hence constituting a significant CC. Also wall B formed a CC in parts of the route. The S_{common} along the measurement route is shown in Figure 9.8 (c). In order to study how the S_{common} affects the inter-link correlation and sum rate capacity in a real environment, the *SRC* and *CMC* were calculated for the same dual-link measurement as in Section 9.2 (see Figure 9.7 for the measurement scenario). The collinearity and capacity were calculated by applying the measured propagation path parameters obtained by the EKF to Equations (11.4) – (11.12) and by using the same 4-element x-oriented linear array as in the simulations of Section 11.3. Using the parameter estimates in the analysis is necessary in order to first remove the effects of the antennas used in the measurements, and hence to be able to use any desired antenna array in the analysis

Figure 11.6 shows the collinearity and capacity along the measurement route. As in the simulation studies of Section 11.3, the collinearity and capacity were calculated as the mean over 100 independent realizations of the measured channels at each snapshot. Figure 11.6 shows that the collinearity gets very high values in the beginning of the route where the MS was located in the corridor, but falls down to approximately 0.3 in the end of the route where the MS was not anymore in the corridor (see Figure 9.7 for the measurement environment). The capacity behaves the opposite way, as was the case also in the simulation studies in Section 11.3.

By comparing Figure 11.6 and Figure 9.8 (c), we can clearly see that also in the measured channels, the inter-link correlation and sum rate capacity are strongly related to the significance of common clusters; as the significance of common clusters increases, the inter-link correlation also increases, while the sum rate capacity decreases. Table 11.2 shows the cross-correlation values between the *CMC, SRC,* and S_{common} calculated based on the measurement data. It can be seen that the *CMC* and *SRC* are very strongly correlated, the correlation value being -0.91; the negative correlation value close to minus one indicates that whenever the *CMC* increases, the *SRC* decreases, and vice versa. The correlation values between the S_{common} and the *CMC,* and between S_{common} and *SRC* are in the order of 0.7 and -0.7 thus revealing strong relationship between these factors, as well.

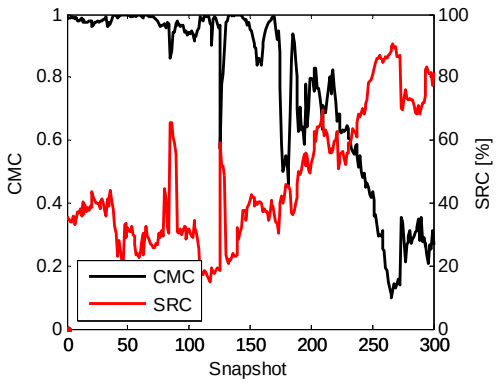

Figure 11.6. Collinearity (black curve) and capacity (red curve) as a function of the measurement location in snapshots. The results are obtained from the measurement scenario shown in Figure 9.7.

Table 11.2. Correlations between CMC, SRC, and S_{common} in the measurement.

	CMC	**SRC**	$\boldsymbol{S_{\text{common}}}$
CMC		-0.91	0.73
SRC	-0.91		-0.69
$\boldsymbol{S_{\text{common}}}$	0.73	-0.69	

11.5 Comparison between simulations and measurements

Finally, in order to investigate the validity of the multi-link GSCM implemented based on the CCs, the simulations were compared with the measurements in terms of dual-link sum rate capacity. Two measurement locations were selected for the comparison. The first location was at snapshot 120, where S_{common} was as high as 85 %, and the second at snapshot 270, where CCs did not exist anymore. In the simulation, two UCCs (per link) and two CCs were randomly located around the simulation environment, whereas the BSs and the MS were at fixed positions. The number of clusters and the BS and MS positions were selected to approximately match those in the corresponding measurement locations.

Figure 11.7 shows the CDFs of the capacity over 100 channel realizations for the measurement (solid lines) and for three independent simulation runs (dashed and dotted lines). As was case in the analyses of the *CMC* and *SRC* above, the comparison between measurements and simulation was carried out by the methodology described by the flow

chart shown in Figure 11.1. However, in this case, since the *CMC* and *SRC* are investigated at selected snapshots, the capacity CDFs are presented as outage capacities over the different channel realizations meaning that each capacity curve corresponds to a single correlation value. It is seen in Figure 11.7 that the simulation can always predict the dual-link channel behavior very accurately in terms of the capacity when S_{common} is 85 %. When S_{common} is 0 %, the model predicts the behavior well for the most of the time; however, occasionally, due to random cluster locations, the correlation between links happens to be high in the simulation which results in underestimation of the capacity.

The results of Figure 11.7 indicate also that if CCs are not included in the channel model, the simulations strongly overestimate the sum rate capacity. This important conclusion can be drawn based on the significant differences between the two measurement locations and the simulations done with S_{common} of 85 % (red curves) and 0 % (black curves). Even though the comparison for the *CMC* is not shown here, a good agreement between the measurement and simulation was found also in terms of the *CMC* as a result of high correlation between *SRC* and *CMC* shown in Table 11.2.

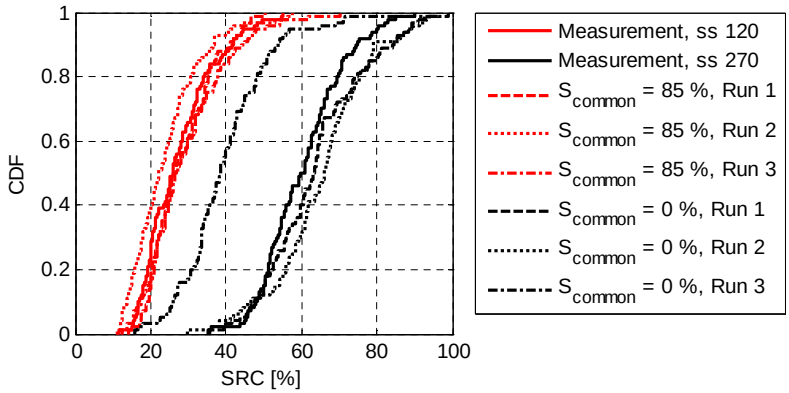

Figure 11.7. Comparison between measurements and simulations. The CDFs of the capacity at snapshots 120 and 270 and of three independent simulation runs with corresponding significance of common cluster are shown. In the simulations, 2 uncommon clusters (per link) and 2 common clusters were generated in random locations.

Summary of part IV

Part IV was dedicated for discussing how to extend GSCMs to support simulations of multi-link scenarios. First, the physical phenomena causing inter-link correlation were discussed, including geometrical properties of the environment, correlated shadow fading, and scatterers that are common among different links.

A multi-link GSCM can be developed based on the concept of common clusters, where the basic idea is to force part of the power in different links to propagate through the same clusters. It was shown based on simulations that a multi-link GSCM implemented based on the concept of common clusters is capable of controlling the correlation between different links. In addition, it was shown that the effect of common clusters on sum rate capacity is significant, meaning that it is vital not to neglect common clusters in multi-link simulations. Finally, the comparison between the simulations and measurements proved that the model can predict the relationships between the significance of common clusters, the inter-link correlation, and the sum rate dual-link capacity in a realistic manner.

Even if the simulation studies were performed with a rather simple implementation of a multi-link GSCM, the concept of common clusters can be applied in any other more sophisticated GSCM, as well. As an example, the concept has been applied in the COST 2100 channel model. However, special care is needed in the multi-link extension of the COST 2100 channel model in terms of the assignment of clusters and visibility regions among different links.

12 Conclusions

Even though research in the field of MIMO systems has been remarkably intensive during the past years, the potential of the MIMO systems is yet to be fully exploited in practical applications at least partly due to limited understanding of the radio channel characteristics. As the core idea of the MIMO technology is to take advantage of multipath propagation, it is vital to know the characteristics of the radio channel in which the system operates from the beginning of the development chain. Since it is practically impossible to test the system performance in all envisioned usage environments by measurements, to have accurate yet easy-to-use radio channel models is compulsory in the development of new radio communication systems that utilize the MIMO technology. As the new wireless applications become more and more sophisticated, requirements for the accuracy of the channel models increase accordingly. For instance, if for the coverage planning of GSM networks it was enough to use simple path loss prediction tools, in the development of novel MIMO systems the models need to predict the radio wave propagation in all angular, delay, and Doppler domains.

The goal of this thesis was to contribute to the development of geometry-based stochastic channel models (GSCMs). The GSCMs have attracted a lot of attention in MIMO channel modeling due to their capability to model the spatial and temporal characteristics of the radio channels in a straightforward manner. Even though the basic modeling framework of the GSCMs was well established already prior to this thesis, they still included several severe shortages. In particular, the previous implementations of the GSCMs were not capable of simulating multi-link scenarios, which is foreseen to become a more and more severe issue in the future as many of the envisioned novel wireless applications will try to utilize links between multiple network nodes in their operation. In addition, the so-called dense multipath components (DMC) had not been considered in previous GSCMs even if they have long been well known to significantly affect the radio channel characteristics. On top of these conceptual shortages, another imperfection in the previous GSCMs was the lack of complete parameterization.

The main achievements of this thesis are the following. First of all, as compulsory background work, a measurement-based ray tracer (MBRT) was developed in order to facilitate detailed analysis of radio channel measurements. The rest of the thesis focused on filling the above-mentioned gaps in the previous geometry-based channel models based on extensive set of measurement data and with the help of the MBRT. Many of the achievements of this thesis have been also directly applied in the development of the new COST 2100 MIMO channel model. Parameterization of several indoor environments was conducted for the COST 2100 channel model. Furthermore, the validity of the COST

2100 channel model was confirmed by comparing the simulation results with the measurement based on which the channel model was parameterized. In addition, a method for including the DMC to the GSCMs was developed based on thorough analysis of the propagation characteristics of the DMC; this novel invention gives insight of how to handle the issue that has long been one of the most fundamental problems in radio channel modeling, i.e. how to include the effects of the DMC in the models.

Finally, a method for extending GSCMs to fully support multi-link simulations was developed based on the concept of common clusters (CCs). This modeling concept is based on the idea that the correlation between different links can be controlled by forcing part of the power to propagate via the same clusters in different links. On the other hand, observations made in measurements indicated that CCs indeed exist also in realistic environments, and in fact, can in certain types of environments carry significant parts of energy. It was shown based on simulations that CCs are a suitable means to control the inter-link correlation, and that the GSCM based on CCs can predict the relationships between the significance of common clusters, inter-link correlation, and sum rate capacity realistically in comparison with the measurement results.

In the future, the novel modeling concepts developed in this thesis should be thoroughly validated against measurement data. This, however, is not an easy task since appropriate references are not currently available; To assess the quality of the modeling approach for the DMC, it is difficult to obtain a valid reference due to the fact that current parameter estimation algorithms, based on which the measurement data are processed, do not include the DMC. What comes to the validation of the multi-link concept, the scarcity of multi-link measurements limits thorough validation work.

Appendix A: COST 2100 channel model parameters

The following tables include values for the cluster parameters of the COST 2100 channel model. Measurements "CS, BS1" and "CS, BS2" represent an indoor hall scenario with LOS conditions, and measurements "RS, BS1" and "RS, BS2" represent an office corridor scenario with NLOS conditions.

A.1 Inter-cluster parameters

Measurement	CS, BS1	CS, BS2	RS, BS1	RS, BS2
Number of clusters N_{C}				
$\mu_{N_{\mathrm{C}}}$	3.69	3.90	4.27	3.72
$\sigma_{N_{\mathrm{C}}}$	0.78	1.41	0.67	0.80
Radius of the visibility region VR [m]				
μ_{VR}	2.77	2.76	3.77	1.79
σ_{VR}	2.44	2.23	2.22	2.47
Cluster selection factor K_{sel}				
$\mu_{K_{\mathrm{sel}}}$	0.70	0.62	0	0
$\sigma_{K_{\mathrm{sel}}}$	0.19	0.15	0	0
LOS power factor K_{LOS} [dB]				
μ_{K}	0.37	-0.75	-9.72	-
σ_{K}	2.77	2.77	7.39	-
Cluster decay factor k_{τ} [dB/µs]				
$\mu_{k_{\tau}}$	54.23	31.84	5.87	15.96
$\sigma_{k_{\tau}}$	25.74	23.00	8.75	63.94
Cluster shadow fading *SF*				
$\sigma_{k_{\mathrm{SF}}}$	4.85	4.41	5.40	6.27

A.2 Intra-cluster parameters

Measurement	CS, BS1	CS, BS2	RS, BS1	RS, BS2
N.o. MPCs in cluster N_{MPC}				
$\mu_{N_{\mathrm{MPC}}}$	3.91	4.47	3.66	2.76
$\sigma_{N_{\mathrm{MPC}}}$	1.01	1.35	0.56	0.67
Angular spread *AS* [deg]				
$\mu_{\varphi_{\mathrm{BS}}}$	0.71	1.68	3.93	1.13
$\sigma_{\varphi_{\mathrm{BS}}}$	0.59	1.51	3.93	0.77
$\mu_{\theta_{\mathrm{BS}}}$	1.95	1.41	3.74	0.54
$\sigma_{\theta_{\mathrm{BS}}}$	1.80	1.11	3.99	0.44
$\mu_{\varphi_{\mathrm{MS}}}$	3.94	3.84	6.6	1.42
$\sigma_{\varphi_{\mathrm{MS}}}$	3.91	2.07	3.00	1.03
$\mu_{\theta_{\mathrm{MS}}}$	3.73	3.97	1.48	0.91
$\sigma_{\theta_{\mathrm{MS}}}$	2.11	2.32	0.93	0.87
Delay spread *DS* [ns]				
μ_{τ}	1.07	1.65	4.48	1.98
σ_{τ}	0.93	1.67	1.52	1.61
Cluster K-factor K_c [dB]				
min	0.40	0.28	0.36	0.39
max	∞	∞	∞	∞
$\mathrm{XPR_V}$ / $\mathrm{XPR_H}$ [dB]				
μ_{XPR}	15.59 / 14.89	12.73 / 13.57	9.55 / 11.35	13.06 / 11.49
σ_{XPR}	10.39 / 11.80	10.86 / 9.88	9.48 / 8.73	7.96 / 9.11
CPR [dB]				
μ_{CPR}	0.88	1.24	-5.27	-3.85
σ_{CPR}	6.57	4.71	11.93	8.98

A.3 Cluster location parameters

Measurement	CS, BS1	CS, BS2	RS, BS1	RS, BS2
Link excess delay $\tau_{c,link}$ [ns]				
$\mu_{\tau_{c,link}}$	34.01	83.17	45.35	55.41
$\sigma_{\tau_{c,link}}$	64.43	71.70	29.31	27.67
Cluster delay $\tau_{C,MS/BS}$ [ns]				
$\mu_{r_c,BS}$	36.24	89.77	49.90	18.01
$\sigma_{r_c,BS}$	11.00	55.31	29.96	12.42
$\mu_{r_c,MS}$	32.79	71.32	17.94	22.01
$\sigma_{r_c,MS}$	27.67	63.03	18.51	18.48
Cluster angle Ψ_c [deg]				
$\mu_{\Psi_c,BS}$	54.61	47.82	49.88	43.16
$\sigma_{\Psi_c,BS}$	55.67	62.70	38.52	39.14
$\mu_{\Psi_c,MS}$	58.41	29.94	5.67	5.54
$\sigma_{\Psi_c,MS}$	44.43	36.30	3.72	6.75

References

[1] J. Poutanen, K. Haneda, J. Salmi, V.-M. Kolmonen, A. Richter, P. Almers, and P. Vainikainen, "Development of measurement-based ray tracer for multi-link double directional propagation parameters," in *Proc. 3rd European Conference on Antennas and Propagation 2009 (EuCAP 2009)*, pp. 2622–2626, Berlin, Germany, March, 2009.

[2] J. Poutanen, K. Haneda, J. Salmi, V.-M. Kolmonen, F. Tufvesson,and P. Vainikainen, "Analysis of radio wave scattering processes for indoor MIMO channel models," in *Proc. The 20th Personal, Indoor, and Mobile Radio Communications Symposium (PIMRC 2009)*, p1569199466, Tokyo, Japan, Sep. 2009.

[3] J. Poutanen, K. Haneda, J. Salmi, V.-M. Kolmonen, and P. Vainikainen, "Modeling the evolution of number of clusters in indoor environments," in *Proc. 4th European Conference on Antennas and Propagation 2010 (EuCAP 2010)*, p1839137, Barcelona, Spain, April, 2010.

[4] J. Poutanen, K. Haneda, V.-M. Kolmonen, J. Salmi, and P. Vainikainen, "Parameterization of the COST2100 MIMO indoor channel model," submitted to *5th European Conference on Antennas and Propagation 2011 (EuCAP 2011)*, Rome, Italy, April, 2011.

[5] K. Haneda, J. Poutanen, C. Oestges, F. Tufvesson, and P. Vainikainen, "Comparison of Delay and Angular Spreads between Channel Measurements and the COST2100 Channel Model", in *Proc. Loughborough Antennas and Propagation Conference 2010 (LAPC 2010)*, p 1569336783, Loughborough, UK, November, 2010.

[6] J. Poutanen, J. Salmi, K. Haneda, V.-M. Kolmonen, and P. Vainikainen, "Angular and shadowing characteristics of dense multipath components in indoor radio channels," *IEEE Transactions on Antennas and Propagation*, vol. 59, no. 1, pp. 245 – 253, 2011.

[7] J. Poutanen, J. Salmi, K. Haneda, V.-M. Kolmonen, F. Tufvesson, and P. Vainikainen, "Propagation characteristics of dense multipath components," *IEEE Antennas and Wireless Propagation Letters*, vol. 8, pp. 791 – 794, 2010.

[8] J. Salmi, J. Poutanen, K. Haneda, A. Richter, V.-M. Kolmonen, P. Vainikainen, and A. F. Molisch," Incorporating diffuse scattering in geometry-based stochastic MIMO channel models," in *Proc. 4th European Conference on Antennas and Propagation 2010 (EuCAP 2010)*, p1841221, Barcelona, Spain, April, 2010.

[9] J. Poutanen, F. Tufvesson, K. Haneda, L. Liu, C. Oestges, and P. Vainikainen, "Adding dense multipath components to geometry-based MIMO channel models," in *Proc. International Symposium on Antennas and Propagation (ISAP 2010)*, p54, Macao, China, November, 2010.

[10] J. Poutanen, K. Haneda, J. Salmi, V-M Kolmonen, and P. Vainikainen, “Analysis of radio wave propagation from an indoor hall to a corridor,” in *Proc. IEEE International Symposium on Antennas and Propagation 2009 (AP-S 2009)*, s408p9, Charleston, SC, June, 2009.

[11] J. Poutanen, K. Haneda, J. Salmi, V.-M. Kolmonen, T. Hult, F. Tufvesson, and P. Vainikainen, “Significance of common scatterers in multi-link radio wave propagation,” in *Proc. 4th European Conference on Antennas and Propagation 2010 (EuCAP 2010),* p 1849081, Barcelona, Spain, April, 2010.

[12] J. Poutanen, K. Haneda, J. Salmi, V.-M. Kolmonen, and P. Vainikainen, “Analysis of correlated shadow fading in dual-link indoor radio wave propagation,” *IEEE Antennas and Wireless Propagation Letters*, vol. 8, pp. 1190 – 1193, 2009.

[13] V.-M. Kolmonen, K. Haneda, T. Hult, J. Poutanen, F. Tufvesson, and P. Vainikainen, ”Measurement-based evaluation of interlink correlation for indoor multi-user MIMO channels,” *IEEE Antennas and Wireless Propagation letters*, vol. 9, pp. 311 – 314, 2010.

[14] V.-M. Kolmonen, K. Haneda, F. Tufvesson, J. Poutanen, and P. Vainikainen, "A dual-link capacity analysis of measured time-variant indoor channel," *Electronics Letters*, vol. 48, no. 8, pp. 592 – 593, 2010.

[15] T. Hult, F. Tufvesson, V.-M. Kolmonen, J. Poutanen, and K. Haneda, ”Analytical dual-link MIMO channel model using correlated correlation matrices,” in *Proc. 4th European Conference on Antennas and Propagation 2010 (EuCAP 2010)*, p1849792, Barcelona, Spain, April, 2010.

[16] K. Haneda, J. Poutanen, L. Liu, and C. Oestges, ”The COST 2100 MIMO multi-link channel model,” Section 3.6 in R. Verdone (ed.), *COST Action 2100 – Pervasive Mobile & Ambient Wireless Communications*, to appear in 2011.

[17] J. Poutanen, F. Tufvesson, K. Haneda, V.-M. Kolmonen, and P. Vainikainen, ”Multi-link MIMO channel modeling using geometry-based approach,” accepted for publication in *IEEE Transactions on Antennas and Propagation, Special Issue on MIMO Technology*, to appear in 2011.

[18] M. Parkin, M. Powell, and K. Matthews, *Economics*, Essex, England, Addison Wesley, Seventh edition, 2008, 830 p.

[19] Internet usage statistics. Available online: http://www.internetworldstats.com.

[20] GSM World. Available online: http://www.gsmworld.com.

[21] 3GPP. 3GPP Long Term Evolution (LTE). Available online: http://www.3gpp.org/Highlights/LTE/LTE.htm.

[22] IEEE. IEEE 802.11 Wireless Local Area Networks (WLAN). Available online: http://www.ieee802.org/11/.

[23] IEEE. IEEE 802.16 Wireless Metropolitan Area Networks (WMAN). Available online: http://www.ieee802.org/16/.

[24] J. Zhu and S. Roy, "MAC for dedicated short range communications in intelligent transport systems," *IEEE Communications Magazine*, vol. 41, no. 12, pp. 60–67, Dec. 2003.

[25] IEEE Draft Standard IEEE P802.11p/D0.26 Jan. 2006, "Draft amendment to standard for information technology telecommunications and information exchange between systems local and metropolitan networks; specific requirements part 11: Wireless LAN medium access control (MAC) and physical layer (PHY) specifications amendment 3: Wireless access in vehicular environments (WAVE)," Tech. Rep., 2006.

[26] C. Huasong, V. Leung, C. Chow, and H. Chan, "Enabling technologies for wireless body area networks: A survey and outlook," *IEEE Communications Magazine*, vol. 47, no. 12, pp. 84 – 93, 2009.

[27] E. Jovanov, C. C. Y. Poon, G. Yang, Y. Zhang, "Guest editorial body sensor networks: From theory to emerging applications", *IEEE Transactions on Information Technology in Biomedicine*, vol. 13, no. 6, November 2009.

[28] P. Enge, and P. Misra, "Special Issue on GPS: The Global positioning System," *Proceedings of the IEEE*, pp. 3-172, January 1999.

[29] A. M. Ladd, K. E. Bekris, A. P. Rudys, D. S. Wallach, and L. E. Kavraki, "On the feasibility of using wireless Ethernet for indoor localization," *IEEE Transactions on Robotics and Automation*, vol. 20, no. 3, June 2004, pp. 555 – 559.

[30] S. Fang and T. Lin, "A dynamic system approach for radio location fingerprinting in wireless local area networks," *IEEE Transactions on Communications*, vol. 58, no. 4, Apr. 2010, pp. 1020 – 1025.

[31] C. Drane, M. Macnaughtan, and C. Scott, "Positioning GSM telephones," *IEEE Communications Magazine*, vol. 36, no. 4, pp. 46 – 54, 1998.

[32] M. Rabinowitz and J. J. Spilker, "A new positioning system using television synchronization signals," *IEEE Transactions on Broadcasting*, vol. 51, no. 1, pp. 51 – 61, 2005.

[33] L. Yang and G. Giannakis, "Ultra-wideband communications: An idea whosetime has come," *IEEE Signal Processing Magazine*, vol. 21, no. 6, pp. 26–54, Nov. 2004.

[34] C. Park and T. S. Rappaport, "Short range wireless communications for next-generation networks: UWB, 60 GHz millimeter-wave WPAN, and ZigBee," *IEEE Wireless Communications*, vol. 14, no. 4, pp. 70 – 78, 2007.

[35] G. J. Foschini and M. J. Gans, "On limits of wireless communications in a fading environment when using multiple antennas," *Wireless Personal Communications*, vol. 6, no. 3, pp. 311–335, 1998.

[36] A. Nosratinia, T. Hunter, and A. Hedayat, "Cooperative communications in wireless networks," *IEEE Communications Magazine*, pp. 74 – 80, October 2004.

[37] A. Paulraj, R. Nabar, and D. Gore, *Introduction to space-time wireless communications*, New York, NY, Cambridge University Press, 2003, 277 p.

[38] S. R. Saunders, Antennas and propagation for wireless communication systems, Chichester, England, John Wiley & Sons Ltd, 2000, 409 p.

[39] E. Telatar, "Capacity of multi-antenna Gaussian channels," *European Transactions on Telecommunications*, vol. 10, no. 6, pp. 585–595, 1999.

[40] D. Gerlach and A. Paulraj, "Base station transmitting antenna arrays for multipath environments," *Signal Processing*, vol. 54, no. 1, pp 59 – 73, 1996.

[41] M. Lotter and P. van Rooyen, "Space division multiple access for cellular CDMA," in *Proc. IEEE 5th International Symposium on Spread Spectrum Techniques and Applications*, vol. 3, Sun City, South Africa, Sep. 1998, pp. 959 – 964.

[42] A.H. Sayed, A. Tarighat, and N. Khajehnouri, "Network-Based Wireless Location: Challenges faced in developing techniques for accurate wireless location information", *IEEE Signal Processing Magazine*, July 2005, pp. 24 – 40.

[43] I. Bekkerman and J. Tabrikian, "Target detection and localization using MIMO radars and sonars," *IEEE Transactions of Signal Processing*, vol. 54, no. 10, pp. 3873 – 3883, 2006.

[44] W. A. Syafei, Y. Nagao, M. Kurosaki, B. Sai, and H. Ochi, "A gigabit MIMO WLAN system with international standardization strategy," in *Proc. International Symposium on Intelligent Signal Processing and Communication Systems 2009 (ISPACS 2009)*, Kanazawa, Japan, Jan. 2009, pp. 228 – 231.

[45] M. Steinbauer, A. F. Molisch, A. Burr, and R. Thomä, "MIMO channel capacity based on measurement results," in *Proc. European Conference on Wireless Technology*, Paris, France, October 2000.

[46] J. Wallace and M. Jensen, "Mutual coupling in MIMO wireless systems: a rigorous network theory analysis," *IEEE Transactions on Wireless Communications*, vol. 3, no. 4, pp. 1317 – 1325, July 2004.

[47] R. Stridh, B. Ottersten, and P. Karlsson, "MIMO channel capacity of a measured indoor radio channel at 5.8 GHz," in *Conference Record of the Thirty-Fourth Asilomar Conference on Signals, Systems, and Computers, 2000.*, vol. 1, pp. 733-737, 2000.

[48] P. Kyritsi and D. Cox, "Correlation properties of MIMO channels for indoor scenarios", in *Conference Record of the Thirty-Fifth Asilomar Conference on Signals, Systems, and Computers, 200.*, vol. 2, pp. 994-998, 2001.

[49] M. Steinbauer, A. F. Molisch, and E. Bonek, “The double-directional radio channel,” *IEEE Antennas and Propagation Magazine*, vol. 43, no. 4, pp. 51–63, 2001.

[50] A. F. Molisch, *Wireless Communications*, Wiley-IEEE Press, New York, NY, USA, 2005.

[51] P. Almers, E. Bonek, A. Burr, N. Czink, M. Debbah, V. Degli-Esposti, H. Hofstetter, P. Kyösti, D. Laurenson, G. Matz, A. F. Molisch, C. Oestges, and H. Özcelik, “Survey of channel and radio propagation models for wireless MIMO systems,” *EURASIP Journal on Wireless Communications and Networking*, vol. 2007, 2007, article ID 19070.

[52] G. Corazza, V. Degli-Esposti, M. Frullone, and G. Riva, “A characterization of indoor space and frequency diversity by ray-tracing modeling,” *IEEE Journal on Selected Areas in Communications*, vol. 14, no. 3, pp. 411 – 419, Apr. 1996.

[53] F. Fuschini, H. El-Sallabi, V. Degli-Esposti, L. Vuokko, D. Guiducci, and P. Vainikainen, “Analysis of multipath propagation in urban environment through multidimensional measurements and advanced ray tracing simulation,” *IEEE Transactions on Antennas and Propagation*, vol. 56, no. 3, pp. 848 – 857, Mar. 2008.

[54] T. Kurner, D. Cichon, and W. Wiesbeck, “Concepts and results for 3D digital terrain-based wave propagation models: an overview,” *IEEE Journal on Selected Areas in Communications*, vol. 11, no. 7, pp. 1002 – 1012, Sept. 1993.

[55] K. Yee, “Numerical solution of inital boundary value problems involving Maxwell's equations in isotropic media,” *IEEE Transactions on Antennas and Propagation*, vol. 14, no. 3, pp. 302 – 307, May 1966.

[56] R. F. Harrington, Field Computation by Moment Methods. New York, NY: the Macmillan Co., 1968, 229 p.

[57] A. F. Molisch, H. Asplund, R. Heddergott, M. Steinbauer, and T. Zwick, “The COST 259 directional channel model – Part I: overview and methodology,” *IEEE Transactions on Wireless Communications*, vol. 5, no. 12, pp. 3421–3433, 2006.

[58] H. Asplund, A. A. Glazunov, A. F. Molisch, K.I. Pedersen, and M. Steinbauer, “The COST 259 directional channel model – Part II: macrocells,” *IEEE Transactions on Wireless Communications*, vol. 5, no. 12, pp. 3434–3450, 2006.

[59] H. Hofstetter, “Characterization of the wireless MIMO channel,” Ph. D. dissertation, Technische Universität Wien, Austria, September 2006, ISBN 3-902477-12-1.

[60] L. M. Correia (ed.), Mobile Broadband Multimedia Networks – Techniques, Models and Tools for 4G, Elsevier, Oxford, UK, 2006, 569p.

[61] WINNER II deliverable D1.1.2 V1.1, *WINNER Channel Models.* Online: http://www.ist-winner.org/deliverables.html.

[62] A. Saleh and R. Valenzuela, “A statistical model for indoor multipath propagation,” *IEEE Journal on Selected Areas of Communications*, vol. 5, no. 2, pp. 128 – 137, Feb. 1987.

[63] T. Zwick, C. Fischer, D. Didascalou, and W. Wiesbeck, “A stochastic spatial channel model based on wave-propagation modeling,” *IEEE Journal on Selected Areas of Communications*, vol. 18, no. 1, pp. 6 – 15, Jan. 2000.

[64] http://www.cost2100.org/

[65] A. Burr, “Capacity bounds and estimates for the finite scatterers MIMO wireless channel,” *IEEE Journal on Selected Areas in Communications*, vol. 21, no. 5, pp. 812–818, 2003.

[66] M. Debbah and R. R. Muller, “MIMO channel modeling and the principle of maximum entropy,” *IEEE Transactions on Information Theory*, vol. 51, no. 5, pp. 1667–1690, 2005.

[67] A. M. Sayeed, “Deconstructing multiantenna fading channels,” *IEEE Transactions on Signal Processing*, vol. 50, no. 10, pp. 2563–2579, 2002.

[68] C.-N. Chuah, J. M. Kahn, and D. Tse, “Capacity of multiantenna array systems in indoor wireless environment,” in *Proceedings of IEEE Global Telecommunications Conference (GLOBECOM ’98)*, vol. 4, pp. 1894–1899, Sidney, Australia, November 1998.

[69] D. Chizhik, F. Rashid-Farrokhi, J. Ling, and A. Lozano, “Effect of antenna separation on the capacity of BLAST in correlated channels,” *IEEE Communications Letters*, vol. 4, no. 11, pp. 337–339, 2000.

[70] D.-S. Shiu, G. J. Foschini, M. J. Gans, and J. M. Kahn, “Fading correlation and its effect on the capacity of multielement antenna systems,” *IEEE Transactions on Communications*, vol. 48, no. 3, pp. 502–513, 2000.

[71] J. P. Kermoal, L. Schumacher, K. I. Pedersen, P. E. Mogensen, and F. Frederiksen, “A stochastic MIMO radio channel model with experimental validation,” *IEEE Journal on Selected Areas in Communications*, vol. 20, no. 6, pp. 1211–1226, 2002.

[72] W. Weichselberger, M. Herdin, H. Özcelik, and E. Bonek, “A stochastic MIMO channel model with joint correlation of both link ends,” *IEEE Transactions on Wireless Communications*, vol. 5, no. 1, pp. 90–99, 2006.

[73] http://www.cost.eu/

[74] Commission of the European Communities, *Digital Land Mobile Radio Communications - COST 207*, Brussels 1989.

[75] Final report of the COST Action 231, “Digital mobile radio towards future generation systems, final report.” Available online: http://www.lx.it.pt/cost231/final_report.htm (accessed on August 26, 2010).

[76] J. Poutanen, K. Haneda, J. Salmi, V.-M. Kolmonen, and P. Vainikainen, "Angular characteristics of dense multipath components in indoor radio channels," *COST2100 9th Management Committee Meeting*, Vienna, Austria, TD(10)911, Sep. 28 – 30, 2009.

[77] P. Kyösti, D. Laselva, L. Hentilä, and T. Jämsä, "Validating IST WINNER indoor MIMO radio channel model," in *Proc. IST Mobile and Wireless Summit*, Mykonos, Greece, June 2006.

[78] Y. Zhang, J. Zhang, G. Liu, X. Gao, and P. Zhang, "A generic validation framework for wideband MIMO channel models," in *Proc. 7th IEEE Vehicular Technology Conference, (VTC Spring 2008)*, Marina Bay, Singapore, pp. 330–334, May 2008.

[79] V.-M. Kolmonen, "Propagation channel measurements system development and channel characterization at 5.3 GHz," Ph. D. dissertation, Helsinki University of Technology, Department of Radio Science and Engineering, Report 12, Apr. 2010. [Online]. Available: http://lib.tkk.fi/Diss/2010/isbn9789526030531/.

[80] J. Salmi, "Contributions to measurement-based dynamic MIMO channel modeling and propagation parameter estimation," Ph. D. dissertation, Helsinki University of Technology, Department of Signal Processing and Acoustics, Report 10, Aug. 2009. [Online]. Available: http://lib.tkk.fi/Diss/2009/isbn9789522480194/.

[81] V.-M. Kolmonen, P. Almers, J. Salmi, J. Koivunen, K. Haneda, A. Richter, F. Tufvesson, A. F. Molisch, and P. Vainikainen, "A dynamic dual-link wideband MIMO measurement system for 5.3 GHz," *IEEE Transactions on Instrumentation and Measurement*, vol. 59, no. 4, pp. 873 – 883, March 2010.

[82] V.-M. Kolmonen, J. Kivinen, L. Vuokko, and P. Vainikainen, "5.3-GHz MIMO radio channel sounder," *IEEE Transactions on Instrumentation and Measurement*, vol. 55, no. 4, pp. 1263 – 1269, Aug. 2006.

[83] http://www.channelsounder.de/ruskchannelsouder.html.

[84] R. Roy and T. Kailath, "ESPRIT - estimation of signal parameters via rotational invariance techniques," *IEEE Transactions on Acoustics, Speech and Signal Processing*, vol. 37, no. 7, pp. 984 – 995, July 1989.

[85] J. A. Fessler and A. O. Hero, "Space alternating generalized expectation maximization algorithm," *IEEE Transactions on Signal Processing*, vol. 42, pp. 2664 – 2677, Oct. 1994.

[86] A. Richter, "Estimation of radio channel parameters: Models and algorithms," Ph. D. dissertation, Technische Universität Ilmenau, Germany, May 2005, ISBN 3-938843-02-0. [Online]. Available: www.db-thueringen.de

[87] J. Salmi, A. Richter, and V. Koivunen, "Detection and tracking of MIMO propagation path parameters using state-space approach," *IEEE Transactions on Signal Processing*, vol. 57, no. 4, pp. 1538 – 1550, April, 2009.

[88] L. Vuokko, P. Vainikainen, and J. Takada, ”Clusters extracted from measured propagation channels in macrocellular environments,” *IEEE Transactions on Antennas and Propagation*, vol. 53, no. 12, pp. 4089 – 4098, Dec. 2005.

[89] http://www.autocad.com.

[90] N. Czink, X. Yin, H. Özcelik. M. Herdin, E. Bonek, and B. Fleury, “Cluster characteristics in a MIMO indoor propagation environment,” *IEEE Transactions on Wireless Communications*, vol. 6. no. 4, Apr. 2007, pp. 1465 – 1476.

[91] N. Czink, P. Cera, J. Salo, E. Bonek, J.-P. Nuutinen, and J. Ylitalo, “Improving clustering performance by using the multi-path component distance,” *IET Electronic Letters*, vol. 42, no. 1, pp. 44 – 45, 2006.

[92] N. Czink, M. Herdin, H. Özcelik, and E. Bonek, “Number of multipath clusters in indoor MIMO propagation environments”, *Electronic letters*, vol. 40, no. 23, November 11, 2004, pp. 1498 – 1499.

[93] N. Czink, X. Yin, H. Özcelik, M. Herdin, E. Bonek, and B. H. Fleury, “Cluster characteristics in a MIMO indoor propagation environment,” *IEEE Transactions on Wireless Communications*, vol. 6, no. 4, April 2007, pp. 1465 – 1475.

[94] L. Hentilä, M. Alatossava, N. Czink, and P. Kyösti, ”Cluster-level parameters at 5.25 GHz indoor-to-outdoor and outdoor-to-indoor MIMO radio channels”, *in Proc. 16th IST Mobile and Wireless Communications Summit*, July 2007, pp. 1 – 5.

[95] R. Durrent, *Essentials of Stochastic Processes*, New York, USA: Springer-Verlag, 2001, 283 p.

[96] R. Vaughan and J. B. Andersen, *Channels, Propagation and Antennas for Mobile Communications*, IEE Press, London, UK, 2003.

[97] L. Liu, N. Czink, and C. Oestges, “Implementing the COST 273 MIMO channel model,” in *Proc. NEWCOM-ACoRN Joint Workshop 2009*, Barcelona, Spain, Mar.-Apr. 2009.

[98] N. Czink, A. Richter, E. Bonek, J.-P. Nuutinen, and J. Ylitalo, “Including Diffuse Multipath Parameters in MIMO Channel Models,” in *Proc. 66th IEEE Vehicular Technology Conference 2007 (VTC Fall 2007)*, pp. 874 – 878, Baltimore, MD, Sept. 30 – Oct. 3, 2007.

[99] A. Richter, J. Salmi, and V. Koivunen, “Distributed scattering in radio channels and its contribution to MIMO channel capacity,” in *Proc. The 1st European Conference on Antennas and Propagation (EuCAP 2006)*, pp. 1 – 7, Nice, France, Nov., 2006.

[100] M. Käske, M. Landmann, and R. Thomä, “Modelling and synthesis of dense multipath propagation components in the angular domain,” in *Proc. 3rd European Conference on Antennas and Propagation 2009 (EuCAP 2009)*, pp. 2641 – 2645, Berlin, Germany, Mar. 2009.

[101] A. Richter, J. Salmi, and V. Koivunen, “Signal processing perspectives to radio channel modelling,” in *Proc 2nd European Conference on Antennas and Propagation 2007 (EuCAP 2007)*, pp. 1 – 6, Edinburgh, UK, Nov. 2007.

[102] M. O. Al-Nuaimi and M. S. Ding, “Prediction models and measurements of microwave signals scattered from buildings,” *IEEE Transactions on Antennas and Propagation*, vol. 42, no. 8, pp. 1126 – 1137, Aug. 1994.

[103] F. Fuschini, H. El-Sallabi, V. Degli-Esposti, L. Vuokko, and P. Vainikainen, ”Analysis of multipath propagation in urban environment through multidimensional measurements and advanced ray tracing simulation,” *IEEE Transactions on Antennas and Propagation*, vol. 56, no. 3, pp. 848 – 857, Mar. 2008.

[104] D. Didascolou, M. Döttling, N. Geng, and W. Wiesbeck, “An approach to include stochastic rough surface scattering into deterministic ray-optical wave propagation modeling,” *IEEE Transactions on Antennas and Propagation*, vol. 51, no. 7, pp. 1508 – 1515, July 2003.

[105] M. R. J. A. E. Kwakkernaat, “Analysis of scattering in mobile radio channels based on clustered multipath estimates,” Ph. D. Dissertation, Eindhoven University of Technology, Eindhoven, The Netherlands, 2008.

[106] F. Quitin, C. Oestges, F. Horlin, and P. De Doncker, “Diffuse multipath component characterization for indoor MIMO channels,” in *Proc. 4th European Conference on Antennas and Propagation 2010 (EuCAP 2010)*, p1847194, Barcelona, Spain, Apr., 2010.

[107] N. Czink, F. Kaltenberger, Y. Zhou, L. Bernado, T. Zemen, and X. Yin, “Low-complexity geometry-based modeling of diffuse scattering,” in *Proc. 4th European Conference on Antennas and Propagation 2010 (EuCAP 2010)*, pp. 1 – 4, Barcelona, Spain, Apr., 2010.

[108] F. Kaltenberger, D. Gesbert, R. Knopp, and M. Kontouris, ”Correlation and capacity of measured multi-user MIMO channels,” in *Proc. IEEE 19th International Symposium on Personal, Indoor and Mobile Radio Communications (PIMRC 2008)*, pp. 1 – 5, Cannes, France, September 2008.

[109] N. Czink, B. Bandemer, G. Vazquez-Vilar, L. Jalloul, C. Oestges, and A. Paulraj, ”Spatial separation of multi-user MIMO channels,” in *Proc. IEEE 20th International Symposium on Personal, Indoor and Mobile Radio Communications (PIMRC 2009)*, pp. 1059 – 1063, Tokyo, Japan, September 2009.

[110] A. Molisch, M. Steinbauer, M. Toeltsch, E. Bonek, and R. Thomä, “Capacity of MIMO systems based on measured wireless channels,” *IEEE Journal on Selected Areas in Communications*, vol. 20, no. 3, pp. 561–569, Apr. 2002.

[111] G. Golub and C. van Loan, *Matrix computations*, 3rd ed. London: The Johns Hopkins University Press, 1996.

[112] R. Blum, “MIMO capacity with interference,” *IEEE Journal on Selected Areas in Communications*, vol. 21, no. 5, pp. 793 – 801, 2003.

The development of new wireless communication systems requires broad knowledge starting from the physical radio wave propagation, going through hardware construction and signal processing algorithm development to the design of high-layer protocols. This thesis deals with the lowest level of the development chain, i.e., with the characterization and modeling of radio channels, mainly for the purposes of multiantenna (MIMO) system development. In addition to the analysis of numerous fascinating radio wave propagation phenomena, novel concepts have been developed for modeling multi-link MIMO scenarios and the so-called dense multipath components, which significantly improves the quality of the available MIMO channel models.

ISBN: 978-952-60-4106-3 (pdf)
ISBN: 978-952-60-4105-6
ISSN-L: 1799-4934
ISSN: 1799-4942 (pdf)
ISSN: 1799-4934

Aalto University
School of Electrical Engineering
Department of Radio Science and Engineering
www.aalto.fi

BUSINESS + ECONOMY

ART + DESIGN + ARCHITECTURE

SCIENCE + TECHNOLOGY

CROSSOVER

DOCTORAL DISSERTATIONS

Aalto-DD 36/2011